INSTITUTE

FOR

AEROSPACE STUDIES

UNIVERSITY OF TORONTO

AN EXPERIMENTAL STUDY OF NONSTATIONARY

INSTABILITIES OF PLANAR SHOCK WAVES IN IONIZING ARGON

Technical note

by

LEVEL

W. L. Buchanan

DTIC

DEC 3 0 1980

C

AFOSR 77-2283

UTIAS-TN-222

August 1980

80 12 29 056

Qualified requestors may obtain additional copies from the Defense
Documentation Center, all others should apply to the National Technical
Information Service.

Conditions of Reproduction:

Reproduction, translation, publication, use and disposal in whole or in
part by or for the United States Government is permitted.

Approved for public release; distribution unlimited.

AN EXPERIMENTAL STUDY OF NONSTATIONARY

INSTABILITIES OF PLANAR SHOCK WAVES IN IONIZING ARGON

by

W. L. Buchanan

Submitted November, 1979

ACKNOWLEDGEMENTS

SUMMARY

A multipulse laser-schlieren technique was used to study the time behaviour of instabilities in the translational front of planar shock waves in ionizing argon in the 10 x 18 cm hypervelocity shock tube at UTIAS. Using a ruby laser in a combined normal-lasing/giant-pulse mode, at least two monochromatic light pulses were obtained about 7 µs apart. As well, a schlieren system compatible with the 23 cm dia Mach-Zehnder interferometer was created with maximum sensitivity for some low-density conditions. The almost-sinusoidal perturbations were found to change with time; some like a standing wave, and others like a travelling wave. It was not, however, possible to associate the observed perturbations with either form of wave motion in nearly half of the cases. A simple graph provides a way to predict the shape of the perturbations from the shock-wave parameters.

TABLE OF CONTENTS

NOTATION

a   speed of sound

A   stability parameter (Eq. 4.1)

d   unsupported diameter of diaphragm

$E(X)$ absolute error in measuring the quantity X

f_1 input focal point of interferometer

f_2 output focal point of interferometer

g   one-half of amplitude of non-planar shock front

h   residual diaphragm thickness in the groove

H   height of oil column in manometer (cm)

I_n schlieren image of translational shock front due to P_n

j   mass flux through shock wave

k π/L

l_n mean shock position (median of l_n^* and l_n')

l_n^* left-most extent of I_n

l_n' right-most extent of I_n

L   channel height

m   atomic mass

M   Mach number of shocked gas in shock-fixed frame

M_s Mach number of shock wave in lab frame

n_h number of half-waves in the shock-front geometry

p   pressure

P_n nth light pulse from the laser

P_1 initial pressure ahead of the diaphragm

P_4 P_{burst}

P_{mix}	pre-ignition driver-mixture pressure
P_{burst}	predicted diaphragm-breaking pressure
R	gas constant
S	distance
t	time; diaphragm thickness
T	temperature; period of oscillation
u	velocity in lab frame
U_s	shock velocity
v	specific volume
w	velocity in the shock-fixed frame; reference wire
W_n	system of transverse disturbances behind I_n
V_t	travelling-wave phase velocity
x	spatial coordinate, laboratory frame
y	spatial coordinate, laboratory frame
z	spatial coordinate, laboratory frame
x'	spatial coordinate, shock-fixed frame
y'	spatial coordinate, shock-fixed frame
z'	spatial coordinate, shock-fixed frame
x_E	relaxation length of ionizing shock wave
n_j	number density of species j
t_p	laser flash-lamp-pumping time
t	time between the emissions of pulses P_1 and P_2
β	angle of incidence of freestream with oblique shock wave
γ	ratio of specific heats
λ	wavelength
λ_1	fundemental wavelength of ruby laser light ($=6943$ Å)
λ_2	second harmonic of the ruby laser light ($=3471.5$ Å)

x   degree of ionization

Subscripts

e   electron

Ar   argon

a   atom

1   preshock test gas (quiescent room-temperature argon);
        giant pulse emitted by laser

2   post-shock test gas; second pulse emitted by the laser

4   driver gas before diaphragm bursts; fourth laser light pulse

fr   frozen ionization state of gas behind translational front

eq   ionization equilibrium conditions

S   standing-wave model of non-planarity

T   travelling-wave model of non-planarity

V   vertical

H   horizontal

1. INTRODUCTION

1.1 Significance of Planar Flow in a Shock Tube

A simplifying assumption in shock-tube flows is that the flow is one-dimensional. Except for thin boundary layers in tubes of large cross-section, this supposition is quite reasonable and has been verified experimentally by many researchers. The shock front under such circumstances is found to be planar at a few diameters from the diaphragm station. Notable exceptions to this expected planarity are the ionizing shock waves in argon and krypton produced in the UTIAS hypervelocity shock tube (Ref. 1,2,3). Interferograms of such shocks display a translational front with decidedly sinusoidal oscillations along with coupled disturbances in the subsequent relaxation regions. The existence of this phenomenon seems to contradict the expected shock-wave stability in a shock tube. It also hinders the reduction of shock-structure data from the interferograms. It has been found that the addition of a small amount of hydrogen to the test gas renders the shock front and the flow planar (Ref. 1,2,3). To date no satisfactory explanation has been put forward for this anomaly but several suggestions have been made by previous researchers pertaining to the source of the non-planarities, mechanisms of propagation, and recommended investigations. The remaining part of this introduction to the present study will 1) provide a precise description of the problem and relate the significance of the investigated phenomenon; 2) summarize the findings and suggestions of previous researchers and 3) state the purpose of the present study as influenced by these proposals.

Shock tubes have been used for many years in conjunction with various optical devices in investigations of high-speed shock waves and high-temperature gas flows (Ref. 4). The monatomic gas argon has been used extensively by researchers studying plasma behaviour and ionization effects because it is readily available in high purity, safe to work with, free of dissociation effects, relatively easy to ionize, and has thermodynamic properties that are well known over a wide range of temperatures and pressures. Because of its high atomic weight (40 amu) its sound speed is not high 320 m/s at room temperature), so that higher flow Mach numbers can be obtained for the same driver and channel pressures (Ref. 4). Lastly, in an argon plasma, the vast difference between m_e and m_{Ar} ($m_{Ar} \sim 70,000\ m_e$) constitutes a significant kinetic barrier between the electrons and the argon ions and atoms, making possible two distinct temperatures T_e and T_{Ar}, even though the species are mixed (Ref. 1-3, 5-7). Researchers utilizing the UTIAS 10 x 18 cm combustion-driven shock tube and the 23-cm diameter Mach-Zehnder interferometer have made use of some of these features of argon to study supersonic corner expansion of plasma (Ref. 8), refractive index of ions (Ref. 1), shock structure (Ref. 1-3, 9-11), shock-induced boundary layers (Ref. 11-15) and oblique shock-wave reflections (Ref. 16-18).

Except for the thin sidewall boundary layer, it is usually assumed in a theoretical analysis that the flow in the unobstructed channel is one-dimensional, that is, all state variables of the test gas at every point (x,y,z) in the channel are functions of the space variable x, only (Fig. 1). This assumption greatly simplifies the mathematical modeling of the gas-dynamics of the shock, which otherwise would be too unwieldy or would involve prohibitive computational costs.

The laboratory coordinate system generally used is shown in Fig. 1, where the (x,y,z)-axes are at the diaphragm station and oriented in the following way. The x-axis is parallel to the longitudinal axis of the shock tube; the y-axis is in the vertical direction; the z-axis is the third axis of the right-handed coordinate system. The shock-fixed coordinates, (x',y',z') are related to the lab coordinates by

$$x' = x - Ut, \qquad y' = y, \qquad \text{and} \qquad z' = z,$$

where U is the shock speed and the shock front is stationary at $x' = x - Ut = 0$, and the gas travels through the shock in the negative x'-direction.

The interferometer receives from the light source light travelling in the z-direction, and its field of view represents the sum of all (x,y)-planes over the shock-tube width of 10.16 cm. If the flow is one-dimensional, each state variable is constant on each (y,z)-plane; hence, the equivalent term "planar" flow. Each (y,z)-plane appears at the image of the test section as a straight vertical line, so the presence of planar flow in the test section implies that every observable variable is constant along such vertical lines in the resultant picture. Great care is taken in the alignment of the interferometer to ensure that photographic light from the light source passing through the test section is in fact parallel to the z-direction, that is, perpendicular to the window surfaces. This alignment is routinely checked by observing that light from the interferometer's point-light source returns to the original point after partial reflection off the various test section window surfaces. A discussion of errors, tolerances and adjustments of the optics of the interferometer is found in Refs. 19 and 20.

It follows from the above discussion that the surface of a shock wave in on-dimensional flow will necessarily be planar, causing the shock to appear as a very thin straight vertical line, if the light pulse used to obtain the picture is short enough to "freeze" the motion. This line is readily seen in schlieren shadowgraph and interferogram (Fig. 2) pictures, but must also be visualized on an interferogram by connecting a series of discontinuous fringe shofts (Figs. 3-6). The abruptness of the fringe shifts attests to the very thin shock surface and shows that schlieren and shadowgraph images of the translational shock do not reflect the actual thickness which is on the order of 10^{-5} cm, or a few mean free paths.

There are two ways in which the shock surface can be distinguished as non-planar. The first occurs when the shock surface position depends upon x and y but not on z; the image consists of a curved thin line and represents a reflected translational shock front (Ref. 18)(C in Fig. 2). The second non-planarity occurs when the shock surface is three-dimensional, when the position depends on z as well as x and y. This effect manifests itself in stray shocks branching out from the main image or in a distinctive "twisted ribbon" appearance where it seems that the observer is looking edge-on at a flexible twisted sheet (Fig. 3). Recognition of three-dimensional phenomena from interferograms (schlieren or shadow photographs) is relatively easy, as small deviations from a thin shock front can be observed.

Since the flow behind the shock front has gone through the wave, it can be expected that the flow is coupled with it. The flow behind a planar shock front is usually planar. This is easily depicted by interferograms, in which

fringe shifts are constant along vertical lines everywhere in the field of view. Planar flow is most vividly illustrated when the no-flow fringes are rotated to be horizontal, that is, parallel to the x' direction. In this case, every fringe is congruent, even in chemically-reacting flows at high temperature (Fig. 4). In plotting a profile of some state variable through a shock-wave transition (e.g., density ρ vs x') from a picture such as Fig. 4, one can be confident that at every position x' the variable had that value over the whole (y', z')-plane. That is, the profile applies to the whole volume of the test section. Similarly, when a variable such as relaxation length x_E is quoted, there is no ambiguity because every fringe provides the same answer. In addition, one may justifiably apply to the observed physical phenomena one of the previously mentioned theoretical analyses which, even though one-dimensional, in many cases is very complex and computationally expensive. Hence interferometric verification of planar flow in the shock tube is essential to the reliable interpretation of measured data.

1.2 Review

While studying ionizing argon gas flows in this facility, Bristow (Ref. 1) obtained interferograms (Fig. 5) which implied that the flow was not planar. He described the flow disturbances as a system of transverse waves in the post-shock relaxation region related to the sinusoidally curved shock translational front, and postulated weak forward-moving oblique shocks. He observed that wave geometry was not consistent in identical runs although these non-planarities appeared in each experiment. It was found that no references to such disturbances were made by other researchers investigating similar ionized argon shocks through space and time-resolved interferograms. However, Bristow directs attention to Fig. 1 in Ref. 23 and a system of weak waves in this interferogram which he fails to identify as time-resolved. This moving-mirror time-resolving technique gives the same results as space-resolving techniques only when the flow is quasi-stationary, that is, steady in the shock-fixed coordinates, so that time-independent non-planarities would be faithfully represented. The fact that all perfect gas and dissociating-gas flows generated by this facility (Figs. 2 and 6) were always planar told him that this was an ionization phenomenon, that is, the electron number density n_e was significant. Bristow suggested that the much larger cross-section of this facility (18 x 10 cm as opposed to 8.25 x 8.25 cm in Ref. 24 and 5 x 5 cm in Ref. 23) made possible an ionization resonance effect capable of generating such transverse waves.

Morse and Ingard (Ref. 7) had dealt with the amplification of acoustic disturbances in an electrically-heated two-temperature ($T_e \gg T_a$) plasma. Since the thermally-heated ionizing argon plasma under consideration here has $T_a > T_e$ in the relaxation region (Fig. 7a), Bristow conjectured with some experimental but no theoretical justification that this temperature difference could also cause acoustic amplification. Measures and Belozerov (Ref. 25) showed that for strong shocks in hydrogen the electron and heavy-particle temperatures are essentially equal in relaxation regions (Fig. 7b). Bristow reasoned that adding some hydrogen to the argon test gas would cause the difference between the electron and heavy-particle temperatures to be significantly reduced, thereby spoiling the acoustic amplification so that the flow disturbances would not appear. The addition of 0.4% of H_2 by pressure to the argon test gas in fact rendered the entire flow planar (Fig. 4).

It was found that ignoring the effect of the hydrogen impurity on the equilibrium fringe shift introduced errors smaller than those from other sources,

3

and the investigation continued on its original course. Bristow discussed
several sources of acoustic disturbances inside the shock tube, which,
however, should give rise to similar non-planarities in perfect-gas and
dissociating-gas shocks if they were in fact the cause. The only plausible
explanation that fits the experimental observations seemed to be that the
postulated acoustic-resonant cavity behind the shock front picked up the
disturbances from sources far upstream of the test section such as gas inlet
ports and amplified them, transmitting them down the shock tube into the test
section as non-planarities in the complex reacting-gas shock wave. In the
absence of a resonant cavity disturbances from such sources die out rapidly,
that is, as $x^{-3/2}$ where x is the distance over which they have propagated
(Ref. 26). An attempt was made to reduce possible effects from the gas ports
to the rectangular channel, but it met with little success.

The addition of the hydrogen impurity was used as the method of stabil-
izing the shock-wave flow because it was effective, expedient and had no
detrimental effects on the flow properties.

Igra (Ref. 8) investigated ionizing argon flow over an expansion corner
by causing an ionizing shock wave to pass down the shock tube over a very
long (5.8m) false upper wall 3.18 cm thick which ended at the test section
with a wedge tappering to the true upper wall. Although interested in the
equilibrium flow behind the shock, he took several pictures of the shock
just passing over the corner. They all showed that the ionizing argon shock
travelling down the smaller cross section was always planar. Note that in
this instance the channel height was no longer 17.78 cm.

Brimelow (Ref. 9) studied shock-induced boundary layers very near the
shock-tube bottom wall and found that non-planarities in the ionizing argon
shock did not hinder his interferometric measurements. He also showed that
in pure argon premature ionization behind the shock front occurred close to the
wall. It was very difficult to tell if this phenomenon was present when the
stabilizing hydrogen impurity was added. No link was made between this
premature ionization near (1 to 2 mm) the wall and the shock-wave non-planarities.

Liu (Ref. 11) conducted an analytical study on the effect of a hydrogen
impurity on the shock structure of ionizing argon, comparing his model-
profiles with data from Ref. 9.

Tang (Ref. 10) investigated experimentally the effects of different types
of impurities on the structure and the non-planarities of ionizing argon shocks.
He found that oxygen, helium, and sodium-chloride had no observable effect on
the instabilities. Only the addition as impurity of 0.4% H_2 or a certain
undetermined amount of water vapour had the stabilizing effect. Tang noted that
his experiments did not have real-gas state variables in the range such that
$(\partial^2 p/\partial v^2)s < 0$, precluding the possibility of shock-wave instability associated
with the violation of the second law of thermodynamics.

In his recommendation for future study, Bristow suggested that an analysis
of the acoustic-wave process for thermally-heated plasma. In conjunction with
this, it was considered important to find the time behaviour of the non-planarities.
The fact that the non-planarities were always present under suitable conditions
although the wave geometries (e.g., the shape of the translational shock front)

were not reproducible in similar runs suggests that they could be time dependent. Normal single-exposure interferograms gave no clue as to the motion of the sinusoidal-shaped shock front. Also it was not clear whether these instabilities occurred across the width of the shock tube as well as the height, that is, if the non-planarities were three-dimensional or only two-dimensional.

In order to investigate the time behaviour of the non-planarities, G. Doubilet* used a framing camera to obtain five interferograms of the same shock wave in ionizing argon, using the ruby laser in the normal-lasing mode as a continuous light source. Each frame took 0.5 microseconds to scan and the time between frames was adjustable; one photographic plate held all five 12 mm diameter images. In contrast, a normal single-exposure interferometric image of the test section is about 10 cm in diameter. The laser was deficient as a continuous light source because in normal lasing the emitted light consisted of pulses about 0.3 microseconds in duration and random in time and energy. Figure 8a(i) shows a trace of the framing-camera shutter voltage with time, while 8a(ii) shows the relative intensity of light emitted from the ruby operated in the normal-lasing mode. The exposures of the five corresponding interferometer frames are shown in 8(b) and depend on the strength or absence of the random light pulses when the electronic shutter is open. The two most promising experiments are shown in Figures 9a and 9b where each frame has been printed separately by the author from Doubilet's two negatives to allow for variations of exposure of the same type as seen in Figure 8b. In each frame, the translational shock front can be seen advancing from right to left, but the grain caused by the framing camera obscures the geometry of the shock fronts. Unfortunately, these pictures provide no information about the time behaviour of the non-planarities.

Lapworth (Ref. 26) studied the evolution of shock-wave perturbations by placing ahead of the test section wedges at the top and bottom of a shock tube and taking a schlieren picture of the resulting shock wave as it passed the windows. The distance between the wedges and the windows was increased between successive pictures to observe how the shock evolved with distance from the wedges. If the resulting pictures were placed side by side according to the distance from the wedges, the product gave the illusion of being one picture consisting of many exposures of the same shock travelling down a shock tube with transparent sidewalls. This method of visualizing time behaviour is feasible only if both the shocks and the observed phenomenon are reproducible, that is, the same in a set of runs. In this case the investigators were confident that the shock strengths and the subsequent wave geometries were consistent over a set of runs.

The above-mentioned elegant method cannot be used to observe the time behaviour of the present phenomenon for two reasons. First, the source of the perturbations is unknown, that is, the researcher has little or no control over the beginning or timing of the disturbances in any one experiment. Second, the many previous interferograms show that wave geometry (for example, the shape of the translational shock front) of the non-planarities is by no means consistent between similar runs. Thus, the method employed in the present study had to ensure that multiple exposures were obtained of the same shock wave, since there was no known reference point ahead of the test section for this phenomenon.

---

*Research Assistant, UTIAS

Bristow also noticed that the curved shock front with the subsequent transverse waves appeared similar to the multi-headed wavefronts of gaseous detonations of H_2,O_2-mixtures, as reported by White (Ref. 28). The structure and evolution with time of these wavefronts are well understood and are illustrated clearly in Fig. 5 of Ref. 32. Each wavefront is a shock wave accross which runs a series of intersecting triple points, each wavehead consisting of a length of the shock between two triple points. The trajectories of these triple points visualized by allowing the passage of the pressure pulses and slipstreams associated with them to leave imprints on soot deposited on the shock-tube wall. It was suggested that this method be used to gain some understanding in a similar way of the time behaviour of the non-planarities considered in this study. If triple points or some other disturbances existed, leaving transverse traces on a soot-covered wall, then a cross-hatch pattern, such as that which appears in Fig. 6 of Ref. 32, would be expected.

A simple relation is put forward in Ref. 23, connecting the average size of a wavehead with the detonation velocity and the reaction induction time. With this in mind, the possibility of obtaining an empirical formula predicting the number of wavelengths in the sinusoidally shaped shock front was investigated.

Therefore, the purpose of the present study was to

1)   determine the time behaviour of the non-planar shock front,

2)   determine if the instabilities are also three-dimensional, and

3)   see what can be learned about these instabilities by the soot-imprint

technique.

2.   EXPERIMENTAL FACILITIES

One object of the experimental work was to investigate the time-dependent behaviour of the sinusoical instabilities of the translational front of strong shock waves produced in argon in the UTIAS 10 x 18 cm combustion-driven hypervelocity shock tube. This was accomplished by obtaining in one picture several space-resolved images of the same travelling shock-wave translational front at different times. Such pictures were produced by a multiple-exposure schlieren system based upon a pulsed ruby-laser light source and the 23 cm dia field-of-view Mach-Zehnder interferometer. This instrument is installed at the shock tube test section. Many modifications (Ref. 1,19) toward the improvement of performance and operation have been made since the construction (Ref. 22,26) of the facility.

2.1   Shock Tube

The UTIAS hypervelocity shock tube is a large (15 m long), robust facility built to simulate high-enthalpy, real-gas flows, generating shock speeds in argon of up to 8 km/s. A detailed description is given by Boyer (Ref. 22) and an excellent update is found in Ref. 19. Only a brief description will be given here, including modifications done by the author.

6

2.1.1 Driver Section and Diaphragms

The driver section consists of a steel cylinder 1.42 m long with an internal diameter of 15.24 cm and a wall 10.16-cm thick. Driver pressures from 800 psi to 6500 pse were obtained by filling the driver with a combustible mixture of 7.5% O_2, 20% H_2 and 72.5% He by pressure to a pressure p_{mix}, and igniting this mixture by impulsively heating a 0.38 mm dia tungsten wire (strung down the axis of the driver) with a high-voltage capacitor discharge. The combustion products are chiefly hot He and H_2^0 at a pressure of about 6.7 times p_{mix}, constituting a near ideal driver gas for deflagrating shock-tube operation (Ref. 4). Ten percent more pressure was added to ensure that the desired driver pressure p_4 was attained and the diaphragm did burst. Thus p_{mix} was related to the anticipated driver pressure p_4 by

$$p_{mix} = (p_4/6.7) \times 1.1 \tag{2.1}$$

Each diaphragm which was made of annealed, type SS 304 stainless steel 35.4 cm in dia. Two 90° grooves were machine-scribed on the driven side of the diaphragm at right angles across its unsupported diameter to ensure petalling when the diaphragm burst. The breaking pressure p_{burst} of the scribed diaphragm was found experimentally by Bristow (Ref. 1) to be given by

$$p_{burst} = K\left(\frac{4\sigma t}{d}\right)\left(\frac{h}{t}\right)^n \text{ psi} \tag{2.2}$$

where   t – total diaphragm thickness

   h – residual thickness in scribed grove

   d – unsupported diameter of the diaphragm (=18.1 cm)

   σ – ultimate tensile strength of SS 304 (=85,000 psi)

   n – fitted constant (=2.2 ± 0.1)

$$\text{and } K - \begin{cases} 1.01 \quad \text{when} \quad t \sim 0.172" \quad (0.438 \text{ cm}) \\ 1.10 \quad \text{when} \quad t \sim 0.108" \quad (0.295 \text{ cm}) \\ 1.06 \quad \text{when} \quad t \sim 0.062" \quad (0.158 \text{ cm}) \end{cases}$$

To ensure proper petalling of the steel diaphragm, the condition $0.55 < h/t < 0.75$ was satisfied. Repeatability and reliability of breaking pressure was experienced since the thicknesses t and h were held within rigid machining tolerances. To achieve a given shock Mach number M_s into a test gas at pressure p_1 a certain driver pressure p_4 is needed. Bristow's empirical relation (Ref. 1) between p_1, p_4, and M_s for argon driven by the combustion process outlined above was used:

$$\ln(p_4/p_1) = 0.422M_s + 4.02 \quad \text{for} \quad 10 < M_s < 24 \tag{2.3}$$

For example, to obtain M_s = 16.15 in 2.50 torr of argon a driver pressure of p_4 = 2452 psi was required, as stipulated by Eq. 2.3. A diaphragm of thickness 5 = 0.1805" (0.458 cm) was scribed to give in the groove a residual

thickness of h = 0.1015" (0.257 cm), so that it would burst at p_{burst} = 2452 psi (168 atm) = p_4, per Eq. 2.2. To produce this shock wave, p_1 = 2.50 torr of argon was admitted into the evacuated channel, and into the driver chamber was admitted 30.2 (2.05 atm) psi of O_2; He gas up to 185 psi (12.5 atm), H_2 gas up to 266 psi (18.2 atm), and then He was admitted up to the pressure p_{mix} = 403 psi(27.3 atm). If the diaphragm had not burst, the driver pressure would have reached a maximum of about 6.7 x p_{mix} = 2700 psi (184 atm) after combustion (Eq. 2.1). As it was, the diaphragm burst at about 2500 ± 50 psi (170 ± 3.4 atm), and M_s was measured at the test section as 16.17. The trace of the driver pressure with time is shown in Figure 10a, produced by a pressure transducer embedded in the end wall of the driver, opposite the diaphragm. The trace starts when the capacitor discharges and initiates combustion, and shows the combustion pressure rise which is terminated by the arrival of the rarefaction wave. Figure 10b shows the pressure record in the test section, the gauge response time (10 μs) and the approach to the equilibrium flow pressure in the test section followed by a fairly uniform pressure stall.

2.1.2 Driven Section

The 15.24 m long driven section contains a 0.457-m circular to rectangular cross-section transition section, a 1.22-m test section located 13.56 m from the diaphragm and a large 1 m^3 shock-absorber dump tank. The channel is smooth on all four sides for a distance of 11.6 m ahead of the 20.32 cm dia test-section windows, 9.53 cm thick. Upon evacuation of the driven section an ultimate pressure of 3 x 10^{-4} torr was reached, representing an impurity of 200 ppm when p_1 = 1.5 torr and 30 ppm when p_1 = 10 torr. Most of the remaining gas was water vapour. The argon test gas had a quoted impurity level of less than 2 ppm. The pressure p_1 in the channel was measured by a sensitive oil manometer giving readings from 0 to 40 torr by the formula

$$p_1 = \frac{1.069 + (25 - T) \times 9.5 \times 10^{-4}}{13.595} \times H$$

where T is the lab temperature in ^{c}C, H is the oil height in mm and p_1 is in torr. The test gas temperature T_1 was taken as the reading given by a thermometer embedded in the upper wall of the channel.

The arrival of the shock-front pressure rise was detected by flushmounted piezoelectric transducers at six stations called D, F, G, H, I, and J along the channel (Fig. 11a). The shock's arrival at D started five counters (No. 1 to No. 5) connected to a common 1 MHz time base, and the arrival of the shock front at each of the remaining five stations stopped a counter in turn. The measured travel times and the corresponding distances between stations were plotted on an (x,t) graph with x=0 at D, and the least-squares second order fit through these points was computed giving the expected travel times and the shock velocity at each station (Fig. 11b). The shock Mach number quoted for shock waves photographed in the test section, and used in subsequent calculations for that experiment, is $M_s = U/a_1$, where U is the expected velocity given by the second order fit at x = 5.791 m (station M), midway between I and J, and a_1 is the test gas sound speed given by $a_1 = \sqrt{\gamma R T_1}$, γ = 1.667 and R = 208.13 m^2/s^2-$°K$ for argon.

The average deviations between times observed and those computed by the second order fit ($t = ax^2 + bx + c$) were consistently less than the counter resolution of ±1 µs over the whole length of 6.096 m from D to J for Mach numbers from 9 to 17. In fact, a deviation of more than 2 µs at a station was an indication that it needed servicing; cleaning and recoating the piezoelectric transducer with a thin layer of silicone rubber usually sufficed.

As a check an additional counter (No. 7), a Hewlett-Packard universal counter (Type 5325A) with a resolution of ± 0.1 µs, measured the time taken for the shock to travel from I to J. The average velocity from I to J computed from this time was compared with the computed velocity U at station M midway between I and J and was found to differ by only a few percent in most cases.

Three changes were made in this study affecting the accuracy and reliability of the value quoted as the velocity of the shock wave observed in the test section.

1) The three Hewlett-Packard (Type 3734A) digital counters were assigned to stations H, I and J which were closest [2 ft (0.61 m), 1 ft (0.305 m) and 1 ft, respectively] to the test section station M, while the two older Racal (Type SA.45) counters with observed resolutions, of 2 µs and 4 µs were assigned to stations G and F, farthest from M [7 ft (2.14 m) and 11 ft (3.36 m), respectively]. Grouping the more accurate counters around the point of interest was expected to increase the reliability of interpolations at M. Previous to this study, the least accurate counters were assigned to I and J. It was observed that this change effected a significant decrease in the difference between the velocity at M computed from the fitted curve and the average velocity given by the time measured between stations I and J on counter No. 7.

2) Previously, the order of the fitted curve was the lowest for which the RMS deviation between observed and expected times was less than 2 µs. Thus an incorrect time caused by a malfunctioning pressure transducer could lead to high-order fitted curves that gave nonphysical results. Locating and eliminating the erroneous datum required a manual work-through of the data. This disadvantage was aggravated by additional errors caused by assigning to the stations I and J the old Racal counters (see previous paragraph) which, when set to record the same time, typically disagreed by 4 µs or more, even when using the same time base.

For this study, a second order least-squares curve was fitted through the data points and the shock velocity quoted was the expected velocity computed from this curve at M. The choice of a second order curve seemed physically appropriate because the expected shock velocity would decrease monotonically, reflecting the attenuation of the shock by viscous forces. This was born out by the fact that the data consistently fit the second order curve very well for M_s from 3.0 to 18.3. The computer program which did the calculation included the deviations of all the observed times from the fitted times so that an errant datum could be easily spotted and quickly removed. These deviations did not exhibit any systematic non-random pattern in this Mach number range, indicating further the adequacy of the second order fit.

3)   In Refs. 1 and 10 the shock velocity quoted was the average
velocity calculated from the time interval measured by counter No. 7,
and this was check against the expected velocity at M; however, this
method depended upon the good working order of the pressure transducers
at I and J and upon the shock wave being quasi-stationary. Reference 19
refers to a method of obtaining a value for U that depends upon the
average velocity between H and I. After observing the magnitude of the
non-planarities of some of the shock fronts obtained before (Refs. 1,10),
it was felt that possible shock-front oscillations would render unreliable
the average velocities obtained from the time measurements along only a
few feet. Thus the second order fitting curve was used to smooth out
any potential variations in observed times due to shock-front oscillations.
Using the expected value of U at M would also reduce the dependence of U
on the working-condition of a few key counters and pressure transducers.
It must be used, of course, when a model is installed in the test section,
since the shock may be changed by the time it reaches station J.

2.1.3 Interferometer and Light Source

The diagnostics of the gas flow in the UTIAS hypervelocity shock tube are
performed with the aid of a 23-cm dia aperture Mach-Zehnder interferometer.
Details of the design and operation of this device are found in Ref. 20.
Up-dated alignment procedures are given in Ref. 19. A short description of the
optical components involved will facilitate a discussion of the application of
interferometry to the present study.

The interferometer whose dimensions are given in Fig. 12 is arranged such
that the upper arm contains the test section which is aligned properly with the
axis of the device by a continuous He-Ne gas laser. The lower arm contains a
compensating chamber with identical windows and test gas. The peripheral optics
are shown schematically in Figure 13. The light source for this instrument is
a TRG, Model 104, pulsed ruby-laser system. The 8 mm dia beam of parallel light
is focussed by a lens to the desired source configuration at f_1 (point for
interferometry and shadow, narrow rectangle for schlieren). The light which
passes through the test section as a parallel test beam, due to defocussing by
parabolic mirror 1 and reflection by splitter 1 and mirror 1, is focussed by
parabolic mirror 2 to f_2 and passes into the camera. For interferograms the
compensating beam consisting of that light passing through splitter 1 is
reflected by mirror 2 and splitter 2, interfering with the test beam. For
shadow and schlieren pictures of events inside the test section, the
compensating beam is blocked. The test section object plane is imaged at the
camera's ground glass by parabolic mirror 2 and the camera lens with a net
magnification of about 0.5.

A short-duration pulse of light is obtained from the ruby laser by
Q-switching the laser cavity with a Pockels cell electro-optical shutter and
polarizer. A retarding voltage of 3 kV is applied to the Pockels cell
preventing lasing until the picture is desired. At this time, the voltage
is removed, that is, the laser is Q-switched, and lasing converts the stored
energy into a 30-ns pulse of coherent, monochromatic light of wavelength
λ_1 = 6943 Å. A second-harmonic generator (SHG) provides a shorter wavelength
λ_2 = 3471.5 Å. The total optical energy output is 0.8 Joules.

The distance between the desired shock position and station I divided by the predicted (see Eq. 2.3) shock speed is used as the time delay between the detected arrival of the shock at I and the triggering of the Q-switch. The difference between the observed and desired shock position depends on the predictibility of the shock speed, and is usually within a few centimeters over the 23-cm field of view.

The flash-lamp pumping time t_p is the time between the triggering of the laser flash lamp and the Q-switching, and normally is designed to be 900 μs for optimal single-exposure photos. A different value of $t_p = 500$ μs was used for some of the present experiments. The station which is closest to the test section and which is expected to detect the shock at a time at least t_p before the time that the shock is calculated to reach the desired position, initiates a time delay unit which accounts for the excess time over t_p and starts the flash-lamp pumping. Counter No. 6 records the actual time interval t_p between the flash-lamp trigger and the Q-switch which is determined mainly by the actual shock speed. The measured t_p for an expected 900 μs ranged from 850 to 950 μs with no consequential loss in picture quality. The measured t_p for an expected 500 μs ranged from 460 to 540 μs and had an effect on the strength of the multiple pulses. This showed up in the number of visible translational shock-front images in one multiple-exposure schlieren picture.

Focussing of the test section object plane is facilitated by providing cross-wires on the windows which can be sharply defined on the ground glass and film plates. Where the wires cross can be used as absolute reference points whose separation can be measured (.25 mm) so that an accurate scale for observed phenomena can be provided in the final pictures. The wires can also be strung in the x and y directions (correct orientation ± 0.01 rad) to conveniently establish the channel axes on the final picture (see Fig. 1).

In the camera the light passes through the camera lens and through a λ_1-line filter, which effectively filters out the second harmonic and the broadband radiation from the ionizing argon shock, and onto the film plate marked λ_1. When dual-wavelength interferograms are desired, part of the light is reflected by a beam splitter and is folded by a mirror down the second arm of the camera, and passes through a λ_2-line filter to expose the film plate marked λ_2. Kodak, Royal Pan X (1250 ASA), 10 cm x 13 cm plate film was used. Upon exposure of the plates, which included a no-flow set taken immediately before each experiment, they were processed in Kodak, DK 50 developer for 7 minutes, stop solution for 15 seconds, and then fixer for 20 minutes.

2.1.4 Accuracy of Measurements

The initial temperature T_1 is measured directly from a standard mercury-bulb thermometer with an uncertainty of ±0.1°K. Thus the absolute error associated with T_1 is $E(T_1) = 0.2$°K.

The initial pressure P_1 is measured indirectly from a sensitive oil manometer from which the oil height is observed. The absolute error associated with any initial pressure from 0.2 to 20 torr is less than 0.1 torr.

The incident shock-wave Mach number M_s must be calculated from the shock velocity and initial sound speed in the argon gas. The shock speed is obtained from a measured distance S, traversed in a measured time t, while the sound speed is calculated from the initial temperature T_1 mentioned above. The uncertainties in the distance, time interval and temperature measurements cause a maximum relative error associated with M_s which can be written as (Ref. 19)

$$\frac{E(M_s)}{M_s} = (1.05 \times M_s + 10.18) \times 10^{-3} \quad \text{for argon.}$$

At $M_s = 10$, the relative error is 2% and $E(M_s) = 0.2$ whereas at $M_s = 18$, the relative error is 2.9% and $E(M_s) = 0.52$. The error $E(M_s)$ is the maximum possible error and in most cases would actually be much less.

As discussed in the previous section, the method of calculating the average shock velocity between I and J by measuring the time interval the shock takes to traverse the short distance (S=61 cm), was not used in this study. This was justified also by the fact that the reading of the interval t on counter No. 7 was often spoiled by circuit noise due to the large number of free electrons (high n_e) inside the steel tube. In such circumstances it was in fact necessary to use the expected velocity at M provided by the second order fitted curve for the shock velocity. When a good reading for t was obtained, the shock velocities derived by these two methods differed by less than 1%, the latter always giving a greater velocity.

Bristow (Ref. 1) states that the shock oscillations must be an ionization phenomenon, appearing when the maximum electron number density $n_{e,E}$ becomes significant. The temperatures T_a and T_e also seem to be involved. To discover what range of values of $n_{e,E}$ and temperature T_a (reflected in M_s) were available in this facility, the equations in Sect. 2.1 and a thermodynamic routine were used to calculate M_s and $n_{e,E}$ for all the values of p_1 and p_4 practical in this shock tube. The result is plotted in Fig. 14 for $T_1 = 298°K$. The driver pressure is limited to $p_4 = 6500$ psi for safety. Large values of p_1 and p_4 give post-shock pressures too great for the test-section windows ($p_2 = 100$ psi). Very low values of p_1 give densities too small to trigger the shock detectors. Note that a maximum value of $n_{e,E}$ is obtained for a given p_4 for a Mach number of about 14.5. An absolute maximum value for this shock tube operation of $n_{e,E} = 2.48 \times 10^{17}$ cm^{-3} is possible.

2.2 Multiple-Pulse Light Source

2.2.1 Pulsed Laser in Combined Mode

A multiple-exposure schlieren system required a multiple-pulse light source which was realized in a ruby laser operated in a combined giant-pulse/normal-lasing mode. For a full description of the ruby laser and discussions on modes of operation, see Ref. 29. Here a simple description will reveal the behaviour behind the combined mode used specifically for this application.

The flash lamp inside the laser irradiates the ruby crystal rod for about 1.5 ms and the absorbed radiation causes population inversion. Normal lasing, in the ruby starts as soon as the inversion level permits it, and the inverted level

12

is depleted very quickly (fraction of a µs), giving a small pulse of coherent monochromatic light. Consequently, while the flash lamp is on, small pulses random in time and energy are emitted (Fig. 8a). In the giant-pulse mode, the lasing-cavity resonance, or Q, is spoiled by directing incipient radiation away from the end mirrors until the desired instant when the Q-spoiling is switched off. During the time interval t_p between the onset of discharge through the flash lamps and the Q-switching, the inversion level in the crystal has been allowed to build up to a level much larger than that obtained during normal lasing. After the Q-spoiling is removed, lasing occurs until the inversion population is depleted, dumping in about 30 ns the stored energy into a "giant" pulse of coherent monochromatic light.

If the flash lamp is still on after Q-switching, i.e., t_p < 1.5 ms, then normal lasing occurs after the giant pulse. The energy in the giant pulse and the total energy in the normal lasing pulses depend upon t_p. Setting t_p = 0 µs disables the Q-switch and gives normal lasing with no giant pulse. Setting t_p = 900 µs gives the largest giant pulse with insignificant normal lasing; this is the setting used to take interferograms at this facility, in order to get one set of bright fringes with no "ghost" fringes (Ref. 19). For this study it was found that operating the Q-switch at an intermediate value of t_p produced a moderate-strength giant pulse and several very-short-duration normal-lasing pulses of usable energy. The optimum value was t_p = 500 µs, and was used in each of the multiple-exposure schlieren experiments. In practise t_p varied from 460 µs to 540 µs; the reason for this is given in Sect. 2.1.2.

The reason for the existence of an optimum value of t_p is clear if these simplified arguments are considered. Inductances in the discharge circuit and a finite heating time in the flash lamp cause the maximum power output of the lamp to occur about 500 µs after the discharge is initiated, that is, at t_p = 500 µs. The energy in the giant pulse depends upon the accumulated energy which is reflected in the area under the flash-lamp power output curve corresponding to the pumping period. However, once the giant pulse empties the energy stored in the ruby crystal, the energy in the normal lasing pulses depends upon the energy transfer rate, i.e., the height of the curve. Hence optimum multiple-pulse output is achieved when energy transfer to the ruby crystal is greatest, about 500 µs after discharge initiation.

For shock speeds of about 5 km/s the shock wave is in the field of view for about 50 µs. The light output of the laser for the 50 µs following a giant pulse with t_p = 500 µs was obtained by measuring on an oscilloscope the current through a photodiode exposed to the light. Figure 15 shows such an oscilloscope trace. The giant pulse p_1 is an order of magnitude stronger than the other pulses, and P_2 is the second strongest. As shown by this and all other traces as well as all schlieren pictures, P_2 follows P_1 by the same time interval—about 7.3 µs. An explanation for this probably involves details of the Pockels-cell Q-switching process. The remaining pulses were random in energy and quite unreliable, in contrast to P_2. Over about 40 experimental runs P_1 produced a clear image each time, P_2 produced a usable image in nine tenths of them, and a third image caused by P_3 was seen in less than one third of them.

Unlike the normal pulses shown in Figure 8a where t_p = 0 µs, those immediately following the giant pulse shown in Fig. 15 had very short durations. This observation was reinforced by the sharpness of the schlieren images caused

13

by these light pulses. At this shock speed no perceptible blurring of the shock front image implied that the pulse durations were less than 0.1 µs.

The time interval between P_1 and P_2 was not adjustable, but was sufficient for the present purpose. In fact, it was very convenient for two reasons. First, this time interval was long enough that the images of the shock wave produced by them were definitely different, that is, a change in shape was clearly seen. Secondly, the interval was short enough that the relationship between the two images was clear. The presence of a third or even fourth image tended to confirm this.

Thus a multiple-pulse light source capable of determining with a certain degree of confidence the time behaviour of the instabilities was realized simply and cheaply merely by changing the operational parameter t_p using the giant-pulse mode of the existing ruby laser. Also, it was fortunate that the light pulses used were monochromatic of wavelength λ_1 = 6943 Å so that a λ_1 notch filter could pass the light from the light source but essentially reject the radiation emitted by the hot plasma behind the strong shock wave, before it reached the camera.

2.2.2 Laser/Spark Light Source

At the beginning of the experimental work it was felt that two separate controlled light pulses could be obtained from the ruby laser and a simple spark light source, each contributing one pulse. The time between pulses was to be variable to provide two images of the shock-wave translational front separated by an adjustable time and, hence, distance. The incumbent laser was to remain unchanged, producing a 0.8 mm dia beam of parallel light converged by a lens to a point at f_1 to act as a point source as required by the interferometer (Ref. 20)(Fig. 13). The spark light source was designed so that the electrodes straddled the point f_1, producing a good approximation to a point source at f_1 while allowing the laser light to pass through in its turn. The spark source designed, built and tested, by A. Morte had a 0.01 µf capacitor and was operated at about 15 kV, thus stored about 1.0J, of which only a small fraction was emitted as broadband light (Ref. 17). Likely less than 10^{-3}J of this was collected and used to produce a photographic image. In contrast, the laser power supply stored 1 kJ. Of that, about 10 J was emitted as radiation by the flash lamp, and about 1 J was emitted by the ruby crystal as a 30-ns pulse of coherent monochromatic light of wavelength λ_1 with a bandwidth of about 0.1 Å (Ref. 29).

The first system consisted of the usual Pockels cell triggering system for single-exposure interferograms, to which was added only a time delay unit adjustable in the range 0 to 100 µs and the triggerable spark light source. The delay unit was started when the Pockels cell was triggered, that is, when the laser pulse occurred, and the delay unit triggered the spark source after the set time delay.

The light output of the spark was just great enough to give a good shadowgraph image on a Kodak Royal Pan X negative plate of non-radiating shock waves in the absence of the λ_1 notch filter which is a necessity for obtaining interferograms of radiating shocks with the laser. The spark emitted a light pulse with a duration less than 50 ns and gave sharp images of shock waves up to about M_s = 7 in argon, i.e., shock speed of about 2.5 mm/µs. However,

above $M_s = 7$ significant radiation from the plasma behind the shock overpowered the spark light. Since both sources were emmitting broadband light and were of comparable brightness, the spark image could not be seen nor separated, and the picture was spoiled.

The author feels that this two-exposure system would be very useful in studying many other problems based on evolving non-radiating shock waves in the UTIAS hypervelocity shock tube, since it was easy to set up and reliable in operation. The spark source was subsequently not used in the present study only because the phenomenon considered involved radiating shocks, to which the above mentioned system was therefore not applicable. Installing a capacitor of higher value would certainly increase the spark energy and hence the usefulness of this simple yet effective auxiliary spark light source.

2.2.3 Discussion of Other Light Sources

Reference 30 describes the design and operation of an eight-channel high-speed multiple-spark camera which gave eight separate schlieren pictures arranged in a circle on a 4" x 5" plate. However, the energy of each spark was about the same as that of the spark source described in Sec. 2.2.2, and for the same reason the light source could not be used here. This camera could produce eight good quality schlieren photos separated by adjustable times, at the cost of a complex triggering system. If only two exposures of shock waves will suffice, the pulsed-laser/spark-source system has the great advantage of economy, convenience and reliability.

A previous spark source (Ref. 20) used alone with this interferometer employed a very high-energy spark with a notch filter to obtain a strong pulse of light with a very narrow frequency distribution, similar to that of a laser beam but not as narrow. A similar filter was placed in the beam's path after the test section to filter out most of the broadband shock radiation, letting through the source light which contained more energy than the filtered shock radiation. Because the capacitance of the discharge circuit was so high (22 μf), the pulse duration was very long (5 μs) and the pulse had to be shuttered to less than 0.1 μs with a Kerr cell. This system was later replaced by the ruby laser and the λ_1 notch filter.

Neither the high-power-spark source nor the Ker cell were available, so the simple spark source discussed previously was tried. Unfortunately, none of the characteristics of the instabilities appeared at Mach numbers at which the spark gave a usable picture, i.e., below Mach 7. Hence the simple spark light source could not be employed.

The ideal additional light source would be, of course, another ruby laser capable of giant-pulse operation, which would make feasible two-exposure photography of radiating-gas flows. Unlike the first two light pulses P_1 and P_2 obtained from the ruby laser in the combined giant-pulse normal-lasing mode discussed above, two lasers would provide light pulses of adjustable time separation and comparable strengths. This would obviate the need for the special modification of the schlieren method discussed in Sec. 2.3.2. However, all the ruby lasers available on loan had for the giant-pulse Q-switch a rotating mirror which has an uncontrollable time delay between the Q-switch trigger and laser light output of anywhere from 0 to 125 μs. These lasers were therefore of little practical use, because in this situation where the shock travels at up to 4.5 mm/μs there should be a delay between trigger and light pulse of no more than tenths of a microsecond, as is the case with the Pockels cell. Hence,

15

the existing laser was used for generating two pulses, although the separation time was fixed at 7 μs. As pointed out previously, this compromise presented no serious drawback to the achievement of the purpose of the present work.

2.3 Optical Techniques

This section describes how the schlieren method was applied to the space-resolved multiple-exposure visualization of shock waves. It tells why schlieren was chosen, how schlieren was adapted to multiple-exposure photography, and how an optimal picture was obtained.

2.3.1 Space vs Time-Resolved Photography

The non-planar translational front of strong shocks in argon was first observed in interferograms obtained with the UTIAS Mach-Zehnder interferometer (Refs. 2,9). The theory and application of the interferometer are discussed in Refs. 16 and 15, but a few points pertaining to this study are emphasized here.

The interferometer gives a circular side view of the shock tube channel which is 17.78 cm (7.00") high, through two 23 cm (8") diameter 9.515 cm (3.75") thick windows, thus, a two-dimensional space-resolved image of the test section is obtained, as opposed to a time-resolved image produced by a rotating-mirror camera by passing the image of a narrow slit over the film. Time-resolved pictures are most meaningful when the phenomenon in the shock tube is quasi-stationary and one-dimensional. Space-resolved interferograms can confirm one-dimensionality by showing that the fringe shifts and hence flow properties are independent of y, i.e., the height. In the present case the shock is two-dimensional, in the x and y directions, so the interferometer which resolves the x and y directions is the right tool to use to observe these non-planar effects. Dependence of flow variables on z is small and does not significantly effect the pictures except that sometimes the translational front has the appearance of a twisted ribbon, as seen in Fig. 3.

To observe the time dependence of the shock front the two-dimensional image of the shock front must be resolved in time. This cannot be done continuously on a single photographic plate. However, since the shock wave is travelling, discrete pulses of light through the test section will cause images of the translational shock front to appear at different places on the film plate. Thus a multiple-exposure picture would show some evolution of the non-planarities of the shock front. The multiple pulse provided by the ruby laser, as described in Sec. 2.2.1, was used for this purpose.

2.3.2 Interferometry vs Schlieren Method

Several multiple-exposure interferograms were taken to test the technique, but the results were dissappointing. Giant pulse P_1 filled the entire field of view with bright fringes, and the additional faint fringes produced by p_2 were very difficult if not impossible to detect. Figure 16 is a multiple-exposure interferogram of a shock wave travelling from right to left in argon with M_s = 14.3, p_1 = 10.2 torr, T_1 = 298.56°K, and t_p = 494 μs. The fringes produced by the pulse P_1 are clear, and the shock-front shape is evident at A. The shock front for the second exposure should appear near B, but the P_2 fringes are barely discernible, giving no useful information about the time behaviour of the phenomenon.

Multiple-exposure interferograms would be more feasible if the light pulses were of lesser and comparable energies as would be the case with two ruby lasers. Since another ruby laser with a Pockels cell was not available, it was concluded that, even though interferometry was the most useful single-exposure space-resolving visualization method, it could not be used with the present system.

Since only the translational shock front was initially of interest, the schlieren method (Ref. 21) of visualizing density gradients, which would show primarily the very high density gradient of the translational shock front, was the best method to use in this case. Thus it was expected that each pulse of light which passed through the test section when the shock was present would leave on the photographic plate the ambient illumination and the schlieren image of only the translational front of the shock. The image of the translational front would appear as a thin vertical line, straight if the shock front was planar, or curved or kinked if otherwise. Hence, when several distinct pulses of light passed through the test section while the shock was travelling in it, corresponding images of the translational front would fall on the photographic plate in different places, showing the position and geometry of the shock front at the times at which the light pulses occurred. Each thin vertical image would be displaced horizontally from the previous one by a distance determined by the time between light pulses from the laser and the velocity of the shock wave. Of these three quantities, the shock velocity and image displacement were accurately measurable. The time between P_1 and P_2 calculated in this manner could be compared with those observed on the traces of laser light output (Fig. 15). This time was consistently observed and calculated to be 7.3 ± 0.5 μs. In addition, it was found that the images of flow phenomena besides the shock front did appear, but assigning them to the correct shock front image was facilitated by referring to single-exposure interferograms and schlieren pictures of similar experiments.

2.3.3 Multiple-Exposure-Schlieren Technique

The interferometer is readily available for employing the schlieren method to visualize density gradients in the shock tube, requiring only slight modifications to the peripheral optics to obtain optimal results. Figure 12 shows the particular arrangement used in this study (see Sec 2.1.3).

To obtain dual-wavelength schlieren pictures, Igra (Ref. 8) focussed the laser beam to a point at f_1, introduced a knife edge at the light source image at f_2, and blocked the compensating arm of the interferometer. The quality of the resulting pictures (Fig. C4, C5 of Ref. 7) was unsatisfactory for the present study. Igra points out several pertinent factors: 1) the undiffused coherent laser light and the very small source size caused significant diffraction phenomena to appear on the film plate, (Ref. 34); 2) the focussing of the powerful laser beam caused burning at the knife edge, and 3) attempting to place the knife edge near the source image of both wavelengths (f_2 depends on wavelength and $|f_{\lambda 1} - f_{\lambda 2}| = 3$mm) gave inferior results for both. All these factors contributed to the detriment of the schlieren images.

These problems were avoided in the present study by focussing with a cylindrical lens the powerful laser beam onto a masked glass diffuser to produce a sharply-defined narrow rectangular light source of less coherent

17

monochromatic light at f_1. The glass diffuser made the resultant ambient field of the test-section image more uniform and reproducible, which was of great importance in identifying flow phenomena by comparing flow pictures with no-flow pictures. The laser beam did not burn the glass diffuser when focussed to the narrowest attainable line, but the large focal length (175 mm) of the 50 mm x 60 mm cylindrical lens may have prevented precise focussing. The second harmonic of the laser light was not used so the knife edge was placed at the red λ_1-image of the source by using the red ($\lambda = 6923$ Å) continuous light of the He-Ne aiming laser. Retaining or removing the SHG had no observable effect on the schlieren images.

Since the visualized phenomenon, the shock front, had its density gradient in the x-direction, that is, horizontal, the slit source was oriented vertical, parallel to the knife edge. The knife edge was arranged so that a positive refractive index gradient in the x-direction would cause the source image at f_2 to be displaced to let more light past to fall upon the photographic plate. The camera was focussed on the reference wires 15 cm from the center of the test section toward the camera as suggested by Hall (Ref. 20). This made possible accurate spatial interpretation of the schlieren images by determining from the real wire separations and their sharp images on each picture the magnification of that picture. Since the vertical wires were indeed parallel to the y-axis, deviations of shock-front images from vertical could be easily detected and analysed.

Despite the above-mentioned disadvantages, Igra used no diffuser in the laser optics in order to generate a light source as small as possible to maximize the sensitivity of the schlieren system. In the present study it was felt that any sensitibity lost by using a diffused slit-source instead of an undiffused point-source would be gained in the increased quality and uniformity of the resulting pictures. A maximum sensitivity was necessary to obtain good schlieren pictures because of the quite low densities involved in producing strong shocks in shock tubes, and because of the low energy of the normal-lasing pulses used.

In a conventional schlieren system the knife edge is adjusted to let about half the light from the rectangular light source pass by to fall upon the photographic plate, thereby creating an ambient or "no-flow" field. Density gradients of one sign, which are normal to the knife edge, cause more light to pass while gradients of the opposite sign cause less light to pass. Thus areas lighter and darker than the ambient field are seen on the picture and are interpreted as corresponding to positive and negative density gradients inside the test section.

In this multiple-exposure schlieren system, however, where the giant pulse from the laser is much stronger than the subsequent normal-lasing pulses, an ambient field of significant intensity (about half total) caused by the giant pulse would overpower the images of the translational shock front produced by the weak normal pulses. To prevent this, the knife edge was adjusted to block off more of the source image so that the ambient field created by the giant pulse was very weak and the normal-lasing pulse images would show up clearly through it. This procedure was feasible in this case because the flow phenomenon to be observed, the translational shock front, had density gradients of only one sign. The knife edge was oriented such that

these density gradients bent the light past the knife edge, causing the shock front to appear in a photograph as a light area on a dark ambient field (and opposite on the film plate). Since no density gradients of opposite sign were of concern, it was not necessary to distinguish areas darker than the ambient field to be as dark as was thought best. Due to the nature of the light pulses emitted by the ruby laser operated in the combined giant-pulse/normal-lasing mode (t_p = 500 µs), this modification was essential to the success of the multiple-exposure technique.

This explains why the schlieren pictures that appear in this experimental work seem to be unusually dark. They generally consist of a background that shows the elliptical image (owing to inclination of the beam-splitters and mirrors) of the round test-section windows and the reference wires, and several brighter shock-front images. The number and brightness of the images depended upon the unpredictable energies contained in the normal-lasing pulses described in Sec. 2.2.1. The faint horizontal streaking found in many of the darker schlieren pictures was caused by the grain in the glass diffuser when the source width was very small, but this nonuniformity in the background was identical in flow and no-flow pictures, and was not an obstacle in identifying flow disturbances. Also, the shock front images which were thin, vertical lines were perpendicular to these streaks and the former were easily perceived despite the presence of the latter. A very-fine-grain diffuser would improve future schlieren pictures obtained in this manner.

The reason for maximizing the sensitivity of the schlieren system and for maintaining a very faint background field was to obtain a usable contrast between the giant-pulse ambient field and the normal-lasing images of the shock front in order to successfully observe the shock-front geometry of an ionizing shock wave at different times. This contrast was enhanced in both the photographic and printing process. Kodak, high-density B & W negative plates were exposed to the schlieren image. Prints from these negatives were done on Kodak F-5 high-contrast paper and given a high-gloss finish. The plates were capable of representing a very wide range of exposure. On the other hand, the high-contrast paper could represent only a fraction of the plate's total range, expanding this limited range to the complete set of tones of the paper. The middle of this fractional range was determined by the exposure to which the paper was subjected in printing. In practice, this meant that in spite of the wide variation of absolute exposure on the film plate of the shock images and background due to changes in both controllable and random optical parameters (see Appendix III), the contrast between them could be successfully optimized by varying the exposure given to the printing paper. Flow and no-flow plates and prints were processed identically to minimize differences not associated with flow phenomena, although differences in plate exposure did occur because of slight random variations in laser output energy.

Simultaneous monochromatic dual-wavelength schlieren pictures of the instabilities studied here would have provided information on the refractive index gradients in the test section at wavelengths of λ_1 and λ_2. Since the magnitude of the electron refractive index is greater at λ_1 than at λ_2, information about the presence of mass-density gradients and electron-number-density gradients separately in the disturbed areas behind the curved translational shock front could be obtained. This is practical because of the appreciable refractive index associated with the electron-number density (five times as great in magnitude than that of the mass density at wavelength λ_1) and the

large electron-number densities (up to 2.5×10^{17} cm^{-3}) associated with this phenomenon. The information might have led to a better understanding of the possible ion-acoustic behaviour of the plasma behind the shock as related to the observed geometry. However, there are several disadvantages to this method. The presence of the SHG attenuates the laser output at wavelength λ_1, resulting in light of wavelength λ_2 of only about 10% of the original energy. The beam splitter in the camera attenuates both beams again by at least one half. The fact that the source image position f_2 is not the same for both λ_1 and λ_2 means that the knife edge must be placed to give a compromise in picture quality. All these detract from the sensitivity of the system. These attenuations would most likely prevent the appearance of the fainter images produced by the weaker normal-lasing light pulses, certainly for the second harmonic, if the multiple-exposure mode (t_p = 500 μs) were used. However, to obtain one acceptable image for each wavelength, the giant-pulse mode (t_p = 900 μs) must be used, at the expense of any information about the time behaviour of the shock front geometry.

Since it was this time behaviour information and hence the multiple-exposure method that was desired, the second harmonic λ_2 was not used. The SHG and the camera beam splitter was removed to prevent any attenuation associated with them. The knife edge was placed precisely at the source image at f_2 since only λ_1 was present. All these measures served to increase the source-image intensity at the knife edge and hence increased the sensitivity of the schlieren system in order to observe the images produced by the low-energy normal-lasing pulses when t_p = 500 μs. Thus, knowledge of the time behaviour of the shock front was gained at the expense of observing any separable density and electron-number-density gradients in the complex region behind the non-planar shock front.

2.4 Shock-Wave Signature Technique

The technique of visualizing the pressure pulses and slipstreams associated with detonation waves by observing the imprints left on a film-coated wall (Ref. 27) was attempted here. It was hoped that in this way any local pressure pulses or slipstreams caused by shock intersections linked with the non-planar shock-front geometry would appear, that is, leave a "signature", if they moved transversely across the sidewall of the shock tube.

Each of the two removable test-section window frames is a rectangle 18 cm (7") high and 38 cm (15") wide, containing in the center the window which is 20 cm (8") in diameter, and leaving an open area on each side 18 cm high and 9 cm (3.5") wide. The downstream area of each was chosen for the coating to avoid any damage to the interferometric-quality windows. Due to the high gas speeds and very high temperatures behind the shock wave (over 10,000°K) it was felt that no Mylar or tape should be left in the tube [Oppenheim (Ref. 31) coated sheets of thin Mylar which were taped to his shock-tube wall]. Thus, a thin film of soot from an over-rich acetylene torch was applied directly to these two areas as evenly as possible. Despite the utmost care, blacker streaks made by the thin stream emitted by the torch nozzle were evident. The area on the window frame which was removed was coated most successfully and photographed. The corresponding area on the other frame which was not removed was more difficult to reach to coat and photograph because of the presence of the interferometer and delicate window surface only centimeters away.

The window frame was installed, the shock wave produced, and the frame was removed and photographed again. In this way comparable no-flow and flow pictures of the soot-covered wall were obtained.

3. EXPERIMENTAL RESULTS

3.1 Performance of Multiple-Exposure Schlieren System

Twenty-three runs were successfully conducted using the multiple-exposure schlieren technique, nineteen of which resulted in pictures showing more than one image of the translational shock front. The giant pulse P_1 from the Q-switched ruby laser gave a good schlieren image of the shock each time. The clearness or absence of the images produced by the subsequent normal-lasing pulses varied from run to run; if any of these showed up, the image corresponding to P_2 was certain to be most distinctive.

To examine the behaviour and effectiveness of this technique for the purpose of multiple-exposure photography, the number of usable shock-front images in each picture was plotted versus the pumping time t_p in Fig. 17. from data in Table 3. A shock-front image was considered usable if its geometry or shape could be observed and measured. This graph shows that to obtain the multiple-exposure objective the operational parameter t_p (defined in Sec. 2.2.1) is to be kept below 515-520 µs.

The brightness of the normal-lasing images ranged from almost the same as the giant-pulse image to barely perceptible but still usable. Near t_p = 490 µs the image produced by p_2 was good, but for lower t_p all the images were very faint. This agrees with the laser-pumping described in Sec. 2.2.1, where neither the energy stored in the ruby crystal was due to population inversion nor the power available for normal lasing had reached its peak before the maximum flash-lamp output occurred near t_p = 480 to 500 µs. On the other hand, after about t_p = 530 µs the flash-lamp output had dropped but the energy accumulated in the crystal had increased, and only a bright giant-pulse image was produced upon Q-switching. This was indeed observed.

Thus the best multiple-exposure pictures occurred, as expected, for t_p between 470 and 520 µs. All runs were designed for t_p = 500 µs, but the scatter in the observed values is due to 1) the failure to predict precisely the diaphragm breaking pressure and hence the shock speed, 2) failure to fill the channel with exactly the designed initial pressure because of a reading error of about 0.1 torr, 3) variations in performance of the shock detectors, and 4) uncertain deceleration of the shock. Future experiments of this type should design for about t_p = 485 µs.

3.2 Schlieren Images of Ionizing Shock Wave

Runs conducted to calibrate the schlieren system were designed for lower shock speeds in order to observe the behaviour of the multiple-exposure technique under well-known shock conditions. Figure 18 shows a multiple-exposure schlieren picture of a shock wave travelling from right to left at M_s = 2.99 into argon at an initial pressure of 27.0 torr and temperature of 299.1°K. At this Mach number the only (significant) density gradient occurs at the translational shock front. Each shock-front image is labelled according to the pulse from the laser, operating in the combined giant-pulse/normal-lasing mode

21

$(t_p = 527$ μs), which produced it. Thus P_1, the giant pulse created by the Q-switch, gave the image labelled I_1. The first normal-lasing pulse P_2 produced I_2 some time later, and so on. Four shock images appear clearly in Fig. 18, and much fainter ones can be found on the original print. This is consistent with the typical laser output trace in Fig. 15. As with all others of its type, this picture was printed on high-contrast photographic paper so as to maximize the contrast between the shock images and the background; otherwise a fainter shock image such as I_3 is indistinguishable from the background.

The shock waves appear as a straight white line on a darker background because of the orientation of the knife edge as discussed in Sec. 2.3.3. The thickness of the schlieren image of the shock front reflects not the actual thickness but instead optical parameters, such as the source size (width) and the degree to which the shock surface is parallel to the z-axis. Note the darkness of the background or ambient field illuminated chiefly by P_1, and how little actual contrast there is between I_3 and this field which, if any lighter, would have obscured it. This shows that the practice of cutting out most of the source light at the knife edge was justified for this technique. Most of the normal-lasing images were in fact near this broaderline contrast.

In addition to the schlieren image, a slight shadow graph effect appears at each shock image as a very thin dark line to the left of and immediately adjacent to the thicker white line, a higher density behind the travelling shock wave as expected. A v inverse shadowgraph effect is caused by the vertical wire w_V but not by the horizontal wire w_H whose shore dimension is parallel to the knife edge. Compare the straightness of I_1 to I_4 with w_V which is nearly perfectly vertical and serves in defining the y-direction. The wire w_H is parallel to the shock-tube bottom wall which is visible in each picture, and serves in defining the x-direction.

The shock velocity in this case is $U_S = 963$ m/s and the distances between the shock images can be measured accurately. Thus the times between the emission of the giant pulse p_1 and the three pulses P_2, P_3, and P_4 to create the four images of the travelling shock wave, as shown, were 7.36 μs, 30.8μs, and 58.7 μs, respectively. It was soon discovered that the time of 7.36 μs between the emission of the first two light pulses was very typical, giving only a horizontal displacement in shock images at Mach 3 of 7.1 mm; but at Mach 15, where ionization occurs, one of 3.54 cm.

Figure 19 is a multiple-exposure schlieren picture of a shock wave travelling from right to left at Mach 6.38 into argon at a pressure of 7.45 torr and a temperature of 299.0°K. The shock-wave images $I_1 - I_4$ are produced by the successive light pulses $P_1 - P_4$ from the laser operated with $t_p = 489$ μs. The shock velocity is 2.02×10^3 m/s, giving the time between the emissions of P_1 and P_2 as 6.94 μs, again near 7 μs. The times between the images other than I_1 and I_2 are not reproducible amongst experiments, as can be seen by comparing this picture with Fig. 18. The post-shock temperature T_2 is 3950°K and very little ionization occurs ($\chi < 10^{-8}$). Hence, the shock wave is observed in the picture to be perfectly straight. For Mach 3 and 6.2, removing the λ_1 band-pass filter which screens out broadband radiation has little effect since there is no detectable radiation from the hot gas at this temperature. In these cases the laser/spark light source described in Sec. 2.2.2 could be used, but, as

shown in Figs. 18 and 19, no non-planar shock geometries appear.

Figure 20a is a multiple-exposure schlieren record of an ionizing shock wave moving from right to left at $M_s = 11.5$ into quiescent argon at a pressure of 9.98 torr and a temperature of 299.2°K (Run #2 in Tables 2 and 3). There are two good images I_1 and I_2 caused by P_1 and P_2, and two faint ones may be seen at I_3 and I_4. The shock images are thicker here than in Figs. 18 and 19. This is most likely due to the shock not being parallel to the illuminating light beam, that is, the z-direction as defined in Fig. 1. The greater thicknesses of the succeeding images may also be caused by normal-lasing light pulses that fail to be short enough to "freeze" the shock motion, although this is doubtful. The width of the rectangular (slit) light source which is located at the interferometer input focal point f_1 was reduced significantly from that for Fig. 19. The increased schlieren sensitivity shows the vertical wire as white (schlieren effect) instead of dark (blocking effect) as before.

The larger image thickness does not prevent us from detecting and describing the geometry of each. Using the vertical wires as a reference, pairs of vertical lines containing the shock images can be drawn parallel to these wires which are perpendicular to the bottom wall evident at the bottom of the picture. (The top wall does not appear in any picture since both cannot be viewed simultaneously with the interferometer.) Each pair of lines is illustrated in Fig. 20b and is defined as follows: The left one 1* was drawn to be tangent to the shock image at its left-most extent, and right one 1' was drawn to be tangent at the right-most extent. The lines in Fig. 20b for l_1 are 1_1^* and $1_1'$, respectively. Each pair of lines constructed in this way was separated by some distance in the x-direction which was measured and divided by the picture magnification to get the real separation. The distance between these two tangents to the extreme points of the perturbed shock front is called the "total perturbation" by Lapworth (Ref. 26). Here, we define the amplitude g of the shock front non-planarity to be one half of this quantity. Thus, the amplitudes of the various images of the same shock can be compared. For a planar shock, of course, this amplitude is zero, and 1* and 1' coincide. The shock position 1 was defined as the mean position of 1* and 1'. Thus the image separations are defined, and the time between light pulse emissions can be carried out as before. The shock speed for Fig. 20 is 3.71×10^3 m/s, so the time delay between P_1 and P_2 as indicated by I_1 and I_2 is 6.86 μs.

The shock appears to be perpendicular to the bottom wall at $1_1'$ and approaching the top wall in the same manner at 1_1^*. The curve traced by the image I_1 is very smooth, with no kinks (infinite curvature) that indicate the presence of triple points which are evident in pictures of multi-headed gaseous detonation waves (Refs. 32,33). The shape of the curve in fact suggests a sinusoidal deviation from a straight line, consistent with the observations of Bristow (Ref. 2). If the origin of the (x'-y') plane is fixed to the intersection of l_1 and the bottom wall, then the shock image may be closely described by the locus of points satisfying

$$x = g \cos(ky) \qquad (3.1)$$

where g is the non-planarity amplitude described above and $k = \pi/L$ where L is the height of the shock tube. When y ranges from 0 to L, the angle ky goes through π radians producing one half of a complete cosine wave. Since any number of these half-waves can be connected to fill the length L and still

satisfy the boundary condition, they are used as the unit to describe the shock image geometry. The number of half-waves n_h is the number of these geometrical units detected in a shock image. Thus the number of half-waves in image I_1 in Fig. 20 is $n_h = 1$.

A curve with n_h of these units between $y = 0$ and $y = L$ is

$$x = g \cos(n_h ky) \tag{3.2}$$

The parameter n_h is also equal to the number of times this curve crosses $x = 0$. If an actual shock image I at 1 is close to sinusoidal, then counting the intersections of 1 with the wavy image I to find n_h is easier in practise than other methods involving points of tangency mentioned in the definitions of 1^* and $1'$. Identifying the exact geometry of each image of the same shock and subsequently determining the change over time is also done more reliably by examining the $I - 1$ intersections. Uncertainties in the value of the interger n_h are due to the non-sinusoidal shape of I where intersections with the straight line 1 are difficult to determine. The maximum error in this study is ± 1, but most images have a well-defined value for n_h.

Figure 21a is the multiple-exposure schlieren picture of an ionizing shock wave travelling from right to left at Ms = 14.4 into argon at a pressure of 4.11 torr and a temperature of 297.0°K (Run #8). A value of 504 µs was observed for t_p. The giant pulse P_1 gave a bright image I_1 (compare with I_1 in the three previous pictures), but no other images are detectable. Since the shock speed was 4.62×10^3 m/s the consistent time delay of about 7 µs between P_1 and P_2 would cause I_2 to appear near the place marked "I_2". The absence of any secondary images is probably due to the weakness of the normal-lasing pulses for t_p over 500 µs. The value of $n_h = 3$, and g is measured as 1.6 mm.

Behind the shock image there is a system of intersecting lines W_1 that seem to indicate transverse-moving and colliding shocks. Disturbances behind a steady shock in the shape of a half-wave would be caused by rarefaction and shock (compression) waves. These components are shown in the drawing Fig. 21b for clarity.

A vertical band D_1 about 1.5 cm wide, that is darker than the background, appears about 4 cm behind the shock image, where the lines W_1 are found. This feature is conspicuously absent in the no-flow picture. This dark area is most likely due to the large electron number density gradient dn_e/dx (electron cascade) just before n_e reaches its maximum value n_e,E at the point of quasi-equilibrium behind the strong shock. Since the electrons make a negative contribution to the refractivity of the gas, a positive dn_e/dx would cause a negative refractive index gradient, leaving a dark area on the schlieren record. This explanation coincides with the fringe shifts observed in the monochromatic interferogram in Fig. 22 of a similar ionizing shock in argon where $M_s = 14.77$, $p_1 = 3.95$ torr, and $T_1 = 297.6$°K. The large dn_e/dx is indicated by a large sudden fringe displacement in a direction opposite to that occurring at the translational shock front. Note that the lines W_1 are much brighter inside the band D_1. This signifies that these transverse waves or shocks are intensified in this region. This effect can also be seen in the interferogram of Fig. 22, in which the fringes are disturbed most in this region of sudden fringe shift, caused by the electron-cascade front where n_e achieves its equilibrium value.

Figure 23 is a multiple-exposure schlieren record of an ionizing shock wave moving from right to left at $M_s = 14.5$ into argon at a pressure of 3.18 torr and a temperature of 299.0°K (Run #7). The most notable features of this picture are the large amplitude of I_1, the closeness in shape of I_1 to an ideal cosine curve with $n_h = 2$, and the uniform image width of I_3. The amplitude g of I_1 is 3.2 mm. and the image is sharp because of the very short duration of the giant pulse P_1. Image I_2 is faint but of comparable width, with the same n_h but different g. Image I_3 appears to have been exposed by a light pulse of about 0.7 µs in duration. Despite this, a value for g_3 and n_h can be determined without difficulty. Since the shock speed was 4.66×10^3 m/s, the separation of I_1 and I_2 gives a delay time between P_1 and P_2 of 6.57 µs.

Figure 24 is a multiple-exposure schlieren picture of an ionizing shock wave travelling from right to left at $M_s = 12.3$ into argon at a pressure of 17.04 torr and a temperature of 298.5°K (Run #13). Since the shock speed was 396×10^3 m/s, the time between P_1 and P_2 was 6.64 µsec. In this case all three shock images have a large thickness, even I_1 which was exposed by the short-duration P_1. Thus this image thickness must be done to a three-dimensional effect where the shock viewed exposes its nonplanarity in two directions as well. Other clues to this phenomenon are the decreased image thickness of I_1 near the top of the picture and the increased image brightness at the edges of the image where the gradients are greatest. This is exactly what is seen in the interferogram in Fig. 25. Determining a value for n_h for each shock image is possible, but identifying g is somewhat ambiguous. Equation 3.2 describes the locus of points of the shock translational front in the shock tube only when the shock is two-dimensional, that is, independent of z, as in I_1 of Fig. 23. The non-planarity in the z-direction is well shown by I_1 in Fig. 25. Here $M_s = 12.7$, $p_1 = 11.52$ torr, and $T_1 = 298.1$°K (Run #10); $t_D = 511$ µs and only one image I_1 appears. The edges of I_1 are very well-defined, and seem to constitute two separate shocks with $n_h = 2$ and different amplitudes. The wave system W_1 behind the curve shock front is similar to that observed in Fig. 22.

Figure 26 is a multiple-exposure schlieren record of an ionizing shock wave moving from right to left at $M_s = 16.1$ into quiescent argon at 5.79 torr and 299.4°K (Run #20). Two usable images I_1 and I_2 of the translational shock front appear, each with $n_h = 6$.· Each has behind it a complex system of disturbances (W_1 and W_2) intimatedly linked with it. The shock has moved forward far enough that there is insignificant overlap between the schlieren images of the complex reacting shock produced by light pulses P_1 and P_2 which were separated by 7.37 µs. The shape of I_1 is descri-ed by Eq. 3.2 quite well with $n_h = 6$, and the disturbances behind, which appear to be converging compression waves and intersecting transverse shocks, are related to I_1 in the same manner as in Fig. 22 and 24. Again, the basic geometric unit seems to be the half-wave, and the compression-shock waves are observed for each half-wave in I_1. Each shock in turn intersects with its neighbour to produce the characteristic patterns so apparent here in both W_1 and W_2. The disturbances W_2 are related in exactly the same way to the geometry of I_2. The images of these disturb-ances are remarkedly well-defined and sharp. The cross-hatching observed here bears a resemblance to the pattern left by a multi-headed gas-detonation wave on a soot-covered wall (Refs. 31,32).

Figure 27 is a multiple-exposure schlieren picture of an ionizing shock wave travelling from right to left at $M_s = 14.5$ into quiescent argon at 11.35 torr and 300.1°K(Run #21). Five distinct shock-front images are visible, and

25

some parts of the disturbances behind each can be seen as well. I_1 is clear and shows some three-dimensional effects. The intensification of the transverse shocks in the electron cascade region is clearly seen. This may be coupled to the transition from a compression wave to a shock wave. Images I_2 and I_3 are very close together and are not discernibly different, appearing as a "double" image. This cescription applies as well to the corresponding disturbances W_2 and W_3 behind. Images I_4 and I_5 are similar to the previous pair but are slightly more separated. Only one part of each of W_4 and W_5 is observable. P_1 and P_2 were separated by 7.44 μs.

All interferograms and schlieren pictures of ionizing shocks in argon had some degree of curvature in the shock front. It should be noted that for each one the shock front was perpendicular to the visible bottom wall at the wall. Sometimes this was achieved in only the last few millimeters from the wall as a required boundary conditions. Also, no kinks (infinite curvature) or evidence of triple points was found in the schlieren image of any shock front observed in this study. This can also be said for all such interferograms obtained at this facility except for a few where the fringe spacing makes interpretation of the exact position of the translational shock front difficult. This shows that although the nonplanar shock fronts observed here seem similar in appearance to the multi-headed gas-detonation waves described and illustrated in Figs. 5 and 7 of Ref. 32, there is an essential difference indicated by the lack of triple points in our cases.

3.3 Temporal Behaviour of Non-Planar Shock Front

Single-exposure interferograms and multiple-exposure schlieren pictures with only one visible image would give us no definite information about the time behaviour of nonplanar shock fronts. Only those schlieren pictures with more than one useful image are considered in this section. The sinusoidal shapes of each shock front observed in all the interferograms of ionizing shocks in argon obtained previous to this study led to the following three hypotheses regarding their time behaviour:

1) The shock front was curved but quasi-stationary

   (stationary in the shock-fixed coordinates).

2) The shock front behaved like a standing cosine wave.

3) The shock front behaved like a travelling cosine wave.

A shock wave is either perpendicular to or reflected by a solid wall to maintain an overall flow deflection of zero at the wall. In the absence of any reflections, hypotheses (1) and (2) would be consistent with this boundary condition but, strictly speaking, (3) would not. No triple points, Mach stems, or reflections were found near the wall, but occasionally a shock front image was oblique for all but a few millimeters away from the wall. The amplitude of a standing wave is near zero for a fraction of the time, and a series of single-exposure random pictures should show some in which the amplitude is very small. However, this was not the case. Consequently, single-exposure pictures were insufficient to determine the propagation mechanism, as realized by Bristow (Ref. 1).

26

Equation 3.2 describes the idealized shock-front geometry at one moment, in shock-fixed coordinates. The evolution in time of the shock front for the above hypotheses would be described in shock-fixed coordinates as

1) $\qquad x' = g \cos(n_h k y')$ $\hspace{4cm}$ (3.3)

for a quasi-stationary sinusoidally curved shock front;

2) $\qquad x' = g \cos(n_h k y') \cos \omega_s t$ $\hspace{3cm}$ (3.4)

for a standing cosine wave where $T_s = \dfrac{2\pi}{\omega_s}$ is the period of oscillation; and

3) $\qquad x' = g \cos(n_h k y' + \omega_t t)$ $\hspace{3cm}$ (3.5)

for a travelling cosine wave whose phase velocity is $V_t = \dfrac{\omega_t}{n_h k}$, and whose period is $T_t = \lambda / V_t$.

All the multiple-exposure pictures were examined with these three models in mind. Observations of the change in geometry of the shock front with time consisted of the measurements of several key parameters, suggested by the above three models, of the two shock-front images I_1 and I_2 which were created by the ruby laser giant pulse P_1 and the first normal-lasting pulse P_2 that occurred about 7 μs after P_1. These measurements are listed in Table 3, the Run numbers corresponding to those in Table 2. Parameters t_p and n_s are discussed in Sec. 3.1. The time Δt between laser pulses P_1 and P_2 is the quotient of the distance between the mean positions I_1 and I_2 in the test section of the nonplanar shock-front images, and the shock velocity. Except for Run #10, this delay time is quite consistent.

The relationship between pumping time t_p and the number of distinctive shock images n_s is illustrated in Fig. 17. These findings may be useful to future researchers considering the ruby laser used in this combined mode as a multiple-exposure light source. The parameter g is described in Eq. 3.1, and the larger of the two for I_1 and I_2 is given. The number of half-waves n_h determines the wavelength λ of each. Note that each shock image for a particular run had the same value of n_h. Hence, the value of n_h for any run is well-defined and is applicable to all shock images in the photograph obtained from that run.

The pairs of shock images could be divided roughly into three groups: those exhibiting travelling-wave behaviour, those exhibiting standing-wave behaviour, and those that show neither. In the first group, the images I_1 and I_2 are essentially similar but displaced vertically, suggesting a change in phase of a travelling wave. The measured vertical displacement between images divided by Δt is the phase velocity. The period T_t in Table 3 in this case is the time for the shock front to be displaced vertically by one wavelength from I_1; the wave type is denoted as T. An example of this type appears in Fig. 27, which corresponds to Run #21. The two images appear to be quite smooth and sinusoidal

27

in shape, but appear to be reversed in phase. However, examination of I_4 reveals that the antinode at C is displaced from the antinode B on I_2, and hence must have come from the antinode A on I_1. A comparison of nodes and other features of I_1 with those of I_2 and I_4 gives a similar result. The vertical displacement $\Delta y'$ between I_1 and I_2 is 3.47 cm ±13%, the phase velocity is

$$V_t = \Delta y'/\Delta t = 3.47/7.44 \stackrel{\sim}{=} 0.47 \text{ cm/ } \mu s$$

and the period is

$$T_t = \lambda/V_t = 7.1/0.47 = 15.1 \ \mu s$$

In four runs among a total of 23 runs performed the resulting pair of shock-front schlieren images suggested a travelling sinusoidal wave as opposed to a standing wave, that is, a definite phase displacement as well as equal amplitude was observed. It should be noted that the system of intersecting shocks behind the curved shock front (e.g., W_1 in Fig. 27) was consistent with the latter's geometry for each shock image. For each I_2 displaced in phase from I_1, the system W_2 was moved in the same way from W_1. This is further proof that the curved shock front and the regular pattern of disturbances behind it are intimately linked. In each case observed, the phase displacement between I_1 and I_2 was downward. This is reflected in the plus sign which appears in Eq. 3.5.

In the second group the two shock images I_1 and I_2 have different amplitudes but seem to have the same phase, i.e., a node or antinode would occur at the same height (y value), su-gesting the evolution of a standing wave. Therefore, information about the change with time of this model comes from the two distinct values of g only. In all cases there was a larger value and a smaller value. In order to obtain a rough idea of the period in this mode of motion, the larger value is assigned to the maximum amplitude, so that $(x')_{max} = g$ in Eq. 3.4. Since the time between images is Δt, the angular velocity is $\omega_s = \Delta\theta/\Delta t$, and the period

quoted is $T_s = \dfrac{2\pi}{\omega_s} = \Delta t \dfrac{2\pi}{\Delta\theta}$.

In Fig. 20 (Run #2 in Tables 2 and 3) the images I_1 and I_2 have g measurements of 1.8 mm and 1.1 mm. If this shock was a standing wave with amplitude 1.8 mm, then the angular displacement between them is $\Delta\theta = \cos^{-1} \dfrac{1.1}{1.8} = 0.91$

radians. Since this change occurred in t = 6.86 μs, the period is T_s = 6.86 μs $\times (\pi/\Delta\theta)$ = 48 μs. The fourth image I_4, which has g = 0, can be used to check this result. It is 4.67 cm from I_1, and consequently was exposed 12.6 μs after I_1. This change in angle is one quarter of a period, so one period is 4 x 12.6 μs = 50.4 μs, a time quite consistent with the preceding result. In

this way the presence of additional images again increases the certainty of the applicability of the model.

There are some multiple-exposure schlieren pictures which definitly show a travelling wave and some in which a standing wave is indicated. Others do not show definite evidence of either type and are marked in Table 3 by no wave-type designation. These pictures either show no discernible difference between I_1 and I_2, or they show a difference accountable by both models. Doubtful decisions are accompanied by a question mark.

3.4 Shock-Wave Signature Records

As described in Sec. 2.4, a method for recording the possible trajectory of a shock-front triple point on a layer of black soot on the tube wall was implemented here. Great care was taken to obtain a uniform soot layer, but broad black streaks are seen in pre-run photos of the blackened area. These photos were compared with post-run pictures of the area to detect systematic transverse traces. It was assumed that such traces would be consistent with the geometry of the same shock wave observed by normal photographic means in the window located immediately upstream.

A high driver pressure p_4 was necessary to produce conditions suitable for shock-front oscillations. This required the combustion of a large amount of O_2 and H_2, which resulted in a great quantity of water vapour in the shock tube immediately after an experiment. Condensation caused the interior walls to be coated with water. The imprints were preserved by opening the tube and allowing the inside to dry slowly.

Three experiments were conducted using this technique. An inspection of the blackened areas after each run revealed no markings that could be interpreted as a triple-point trajectory trace. The chief character of these areas was that of a multitude of horizontal steaks supposedly created by the passage of the wet expanding driver gas.

It is concluded that this visualization technique was not appropriate for oscillating ionizing shocks generated in this manner. Another reason for the lack of triple-point traces may simply be due to the absence of any triple points. This conjecture agrees with the observation that no triple points were detected in interferograms of the shock front taken in the same three experiments. Also, no triple points were observed in any schlieren or interferometric records taken of this oscillating ionizing shock front.

4. Discussion and Conclusions

The problem studied here could be classified under several categories. The shape and size of the nonplanarity of the translational shock front suggest that a stability analysis might be in order. The hydrodynamic effects of a sinusoidally curved shock front on the relaxation region behind could be considered. One could also apply the principles of plasma acoustics to the two-temperature ionizing gas in order to predict the origin and type of oscillations. Each of these approaches will be considered, relating the phenomenon observed to the most relevant literature.

Many theorists have concerned themselves with the stability of a plane shock wave (Ref. 35-43). Of the several different types of instability considered, the one applicable to this phenomenon was called by Freeman (Ref. 35) "stability of form". He looked at the shock wave resulting from moving a corrugated piston impulsively into a fluid. Small deviations of the piston surface from planar allowed a linearized theory which showed that the shock's corresponding perturbations from a planar form decayed in time like $t^{-\frac{1}{2}}$ in the strong shock limit, where t is the time between the formation of the shock and the measurement of the perturbations. This technique was applied to the more experimentally tenable geometry of a weak shock passing over thin wedges on the walls of a shock tube, with similar results (Ref. 36). The corresponding experiments were done by Lapworth (Ref. 26) whose composite picture (see Sec. 1.3) depicts a shock which seems to undergo several oscillations somewhat like a standing wave, with two half-wavelengths ($n_h = 2$ in Eq. 3.4) contained in the 5.875 in high channel. In fact, a model similar to Eq. 3.4 with g decreasing with time was used to describe the observed shock. Closer inspection yields some important differences, however, between this and the presently studied phenomenon. Lapworth's shocks have pronounced kinks and reflected (or transverse) shocks projecting backwards from these kinks. No kinks or triple points were observed in the shocks of this study. Lapworth's shock waves were in the perfect gas regime for air, with Mach numbers less than 2, as opposed to the strong ionizing shocks in argon used here. Also, he reported no travelling-wave behaviour. With these disparities in mind, it seems unlikely that the two instabilities utilize the same propagation mechanisms or sources, despite their superficially similar appearance and time behaviour. Thus, a stability-of-form analysis as applied to the present problem would be of limited usefulness.

Other researchers considered the passage of a shock wave through a medium with an arbitrary equation of state, examining the kinds of state equations and small disturbances that would lead to instability. A fundamental paper by D'Iakov was revised and clarified in an illuminating paper by Swan and Fowles (Ref. 38) who used as an initial perturbation to the plane shock wave a travelling wave equivalent to that expressed in Eq. 3.5. (Remember, Eq. 3.5 is in a sense empirical, since it derives from shocks observed in this study.) They found that a linear analysis resulted in stability criteria involving the gradient $(\frac{dp}{dv})_H$ of the Rankine-Hugoniot curve, the Mach number M of the fluid behind the shock in shock-fixed coordinates, and the slope $-j^2$ of the Rayleigh line, the straight line on the p-v plane joining the pre-shock state (v_1, p_1) with the post shock state (v_2, p_2). Here v is the specific volume. Figure 28 illustrates these quantities, including the mass flux j through the shock. With $A = j^2 (\frac{dv}{dp})_H$, the criterion for stability of the shock was found to be

$$-1 < A < 1 + 2|M|. \tag{4.1}$$

They show that if A violates the lower/upper limit, then the shock could degenerate into two waves whose directions of travel are similar/opposite.

Griffiths et al (Ref. 39) obtained time-resolved interferograms of very strong shocks in argon in a cylindrical shock tube. A shock was deemed unstable if, after it reached the window, the shock front or flow behind it was nonplanar but distinct from the contact surface. Unstable shocks were observed for shock Mach numbers in the range $31 < M_s < 34$, which coincided with velocities

30

such that the first ionization of argon was near completion, causing $(\frac{dp}{dV})_H$ to become positive. This observed stability limit was related to neither inequality in Eq. 4.1. Their data suggested the different upper limit stability condition $A < A'$, where

$$A' = \frac{1 - M^2(1 + w_1/w_2)}{1 - M^2(1 - w_1/w_2)} \tag{4.2}$$

and where w_1 and w_2 are the pre- and post-shock gas speeds relative to the shock. The velocity range of observed instabilities occurred when A approached A' closely. The equilibrium post-shock state was used in each case in Ref. 39, but no comment was made concerning the frozen state immediately behind the translational shock front, or the two-temperature plasma in the ionization relaxation region. As well, no attempt was made to link the non-planar shock front and the equilibrium plasma behind it. Unlike the present study, they observed several shocks with planar translational fronts accompanied by nonplanar flow behind.

The shock waves produced in this study were not near completion of the first degree of ionization. That is $\chi < 0.2$ (Tables 1 and 2). The maximum Mach number was 18.0, far short of the observed region of instability of Ref. 39. However, their shocks with disturbances attributed to the contact surface, as opposed to those with $(\frac{dp}{dV})_H > 0$, were placed in a separate class. It is interesting to note that Ref. 39 assigns all shocks with Mach < 25 to this class. In other words, no stable ionizing shocks in argon appeared below $M_S = 25$ to their minimum of $M_S = 18$. Whether or not these disturbances, due to the contact surface, are in fact similar in appearance to those observed in this study, cannot be seen. Although only a limited range of Mach numbers considered by the two investigations were in common, both observed that ionizing shocks in argon around $M_S = 18$ were unstable. A more definitive look at this "contact surface disturbance" would be in order, possibly with space-resolved interferograms. It is safe to conclude that the present nonplanarities cannot be due to the completion of the first degree of ionization as observed in Ref. 39.

It should be noted that none of the shock-wave stability theories, including those using arbitrary state equations, took into account explicitly a nonhomogeneous or a nonequilibrium post-shock state, such as the two temperature ionization relaxation zone behind the shock. Whether or not these effects could be included somehow in the Hugoniot curve or the state equation is not clear. Nonequilibrium studies have generally been in the areas of one-dimensional shock structure (Ref. 2,3,11,23,25,44) and acoustic stability (Ref. 45,46). Also, each theory assumed shocks and perturbations of infinite extent, so that sidewall and reflection effects were ignored. As noted before, when a travelling wave perturbation was observed in this study by the multiple-exposure method, reflections of the perturbations off the walls were not evident, making the shock front conform to Eq. 3.5 more closely than would be expected in a shock tube of finite dimension.

The hydrodynamic consequences of a sinusoidally curved shock wave can be used to explain the compression waves immediately behind the shock, which converge to give transverse shocks. These intersect with their neighbours to

give the system of waves denoted W_n in Figures 2, 25, 26, and 27, where, for example, W_1 corresponds to the image I_1 of the translational shock front. In order to understand this wave system, consider the stationary shock wave in Fig. 29, where the amplitude of the perturbation has been exaggerated for clarity. The gas enters from the left and passes through the shock at an angle β, where $\beta = \frac{\pi}{2}$ for a normal shock. Since $\tan(\beta) = \frac{dy}{dx}$, $\cot(\beta) = \frac{dx}{dy}$, and

$$\beta = \cot^{-1}[-gn_h k \sin(n_h ky)] \qquad (4.3)$$

We can see from the diagram that the shock is normal when $\cos(n_h ky) = \pm 1$, coinciding with $\sin(n_h ky) = 0$, and giving $\beta = \cot^{-1}(0) = \frac{\pi}{2}$, as expected. The quantity gk is dimensionless, representing the relative magnitude of the perturbation. The maximum deviation of the shock front from normal is found for the one in Fig. 26, for example, where $n_h = 6$ and $g = 1.6$ mm, to be $9.7°$.

Assume that the shock shape is stationary, so that the Mach number is the same along the shock front. At each point on it, the gas is deflected toward the shock, as shown in the inset of Fig. 29. The overall pattern of gas deflection immediately behind the shock front is shown by arrows which represent the direction of mass flow. Because of this deflection, compression occurs at C behind the shock front with positive curvature, and expansion occurs at E behind the shock front with negative curvature. These regions C are visible in Figs. 26 and 27. This compression has nothing to do with the real-gas rise in density due to the ionization relaxation, but is a perfect-gas effect at the curved frozen shock front. Compression waves form and converge to weak shocks S. Neighbouring shocks intersect, forming the subsequent system of waves that appear in schlieren pictures as thin lines (Fig. 26 and 27) and in interferograms as barely discernible fringe shifts. The schlieren method shows up these transverse waves better than interferograms (Fig. 22).

Figure 26 also shows the effect that the ionization relaxation has on these transverse waves. After the shocks intersect twice they become significantly steeper and remain so further from I_1. This occurs very near the electron-cascade front. It is not clear what is happening here, since the nature of the transverse waves is still ambiguous.

One important deduction can be made, however, about the curved shock front. Regions marked C in Fig. 29 have a higher than average pressure due to the compression caused by the flow deflection introduced by the curved shock front. Since this region is subsonic relative to the shock, this increased pressure is felt at the shock and tends to increase the shock speed; thus lagging regions would tend to catch up. Similarly, leading parts tend to fall back. This seems to be an argument for stability of form, but the influence of the relaxation region would complicate matters. In any event, the part that is played by this possible mechanism is open, since stability is, in fact, never observed.

Now assume that the shock shape evolves as a standing wave, and consider the two extremes of its oscillation, using Fig. 26 as an example. To get from I_1 to I_2, the shock moved to the left with an average Mach number M_s ($=16.1$). In addition to this, the leading and lagging parts of I_1 travelled different distances in the same time $\Delta t(=7.37$ μs$)$ to reach the configuration I_2. This difference in distance is at most $4 \times g = 6.4$ mm, using the standing wave model

32

Eq. 3.4, and the average distance between I_1 and I_2 is 38.2 mm. Thus, one point along the shock front could attain an average Mach number between I_1 and I_2 as high as 17.4, while another point could have one as low as 14.8. Significant differences in frozen and equilibrium pressure and temperature, as well as the electron number density and the relaxation length, occur between these two Mach numbers. An unsteady two-dimensional reacting-gas shock structure would result. This rough model serves only to gain insight into the complexity of this problem, and does not fully exploit the standing-wave model.

Experimental evidence of the variation, along the shock front, of the relaxation lenth x_E can be observed in Fig. 21. From typical profiles of n_e through the shock wave (Ref. 2), we see that the distance between the shock front and the place where dn_e/dx is a maximum is nearly equal to x_E. The region where dn_e/dx is large shows up on this schlieren record as a dark band D_1. This distance between the shock image I_1 and the band D_1 is least when I_1 lags the mean shock position and greatest when I_1 leads. Since we know that x_E decreases as M_s is increased, this observation implies that the lagging parts of I_1 have been travelling faster than the leading parts. This implies, in turn, that the shock image had a greater amplitude at a previous time. Unfortunately, only one exposure was obtained in this run which is the only run to exhibit a dark band. It must be remembered, however, that D_1 is the result of the geometry of the translational shock front as it was at a time preceding the pulse P_1 by the induction time (the time taken for the gas to reach ionization equilibrium after passing through the shock front). Thus, such an extrapolation could be completely unfounded. However, the fact that D_1 follows I_1 with no detectable shift in the y-direction supports the standing-wave model. Even though Fig. 21 is not able to verify the standing-wave model regarding physical parameters such as x_E, it can help stimulate discussion on the instability phenomenon.

Experimental and analytical research into acoustic stability phenomena in monatomic plasmas has been carried out almost exclusively on electrically heated plasmas, where high-energy electrons from a voltage discharge heat the gas to ionization. The heating is done by the net transfer of energy from the electrons to the atoms by elastic and inelastic collisions, where $T_e \gg T_a$. The availability of high-voltage sources and the elegant theoretical treatments possible with this type of plasma have contributed to its popularity. One such case is the phenomenon of ion-acoustic waves.

On the other hand, the plasma behind a strong shock wave in argon is a thermal plasma, where the atom temperature is suddenly raised significantly in the absence of any free electrons. Ionization occurs initially by inelastic collisions between the atoms and then later by inelastic collisions between the atoms and electrons. Here the relation $T_a \gg T_e$ holds over most of the relaxation regions. Appropriately, the only literature available that discusses thermal plasmas deals with the more specialized topic of shock structure in strong monatomic gases (Refs. 1,6,9,11). Except for papers related to the presently-studied phenomenon (Refs. 2,10), no experiments or theoretical treatment regarding waves in a thermally heated plasma have been found.

Morse and Ingard (Ref. 7) give derivations for several types of acoustic disturbances in the electrically heated plasma ($T_e \gg T_a$), further dividing these into two cases; a weakly ionized gas ($\chi \ll 1$) and a strongly ionized gas ($\chi \sim 1$). The former implication leads to a dominately neutral gas which receives some of the energy that the electrons draw from the external fields,

making acoustic feedback and amplification possible. The latter gives rise to "ion-acoustic" waves in which the neutral particles may be ignored. In each case, the authors' emphasis is on the effect that external fields, such as a strong electric field, have upon the charged particles in the plasma. These theoretical considerations and the present situation differ in three ways: 1) we have here $T_a \gg T_e$ instead of $T_e \gg T_a$, 2) we have a intermediate value for the degree of ionization ($0.03 < \chi < 0.21$), so that neither theory is applicable, and 3) there are no external fields. However, since the net energy exchange between species of different temperatures was instrumental in the acoustic disturbances in Ref. 7, a look at the process is warranted here.

Expressions for the net energy transfer rate between electrons and atoms and between electrons and ions in elastic and inelastic collisions are given in Ref. 2. The energy transfer rate for elastic collisions between electrons and atoms is proportioned to n_e, n_a, T_e, and $T_a - T_e$. The corresponding rate for ions instead of atoms is proportioned to n_e, T_e and $T_a - T_e$. It appears that the electron number density n_e and the species temperatures T_e and T_a probably play a significant role in determining the rate of energy supplied to the plasma disturbance which creates the nonplanar shock front. This was realized by Bristow (Ref. 1) when he added some hydrogen to the argon to force $T_a - T_e = 0$, and hence prevent energy transfer to the hypothesized plasma oscillation. The "resonant cavity" he mentions is roughly the length of the relaxation region times the shock tube internal cross-sectional area, and this cavity follows behind the shock front as it travels. It was thought that some resonance condition existed, depending upon the volume of this "cavity" and the energy input rate, explaining why this phenomenon was not observed in smaller shock tubes. According to observations in this study, discrete resonance conditions seem very unlikely owing to the continuity of n_h over wide ranges of shock parameters. In other words, even though n_h has integer values, shock with a particular value of n_h occur over a range of shock parameters. Also, evidence of a translational front nonplanarity with an amplitude comparable (gk from Eq. 4.3) to those in Table 3 was found in time-resolved interferograms in Refs. 13 and 24. The value of n_h seems to be 1, and the amplitude over the 5 cm channel height is very small, about 1 mm. The authors make no mention of this, most likely because it is so difficult to notice unless looked for. However, the observation of the effect of the hydrogen impurity still stands, suggesting that the notion of some plasma oscillation, supported by energy transfer whose rate depends upon $T_a - T_e$, is valid.

No qualitative description can be given of the plasma oscillation at this time, because it is not clear what type of oscillations: 1) could occur under these plasma conditions (values of n_e, χ, T_a, T_e); 2) would be consistent with the hydrodynamic environment of the shock wave; and 3) give rise to the nonplanar translational shock front as observed here with the corresponding time behaviour.

Since no trend in the amplitudes g of the instabilities was observed, attention was focussed on the number of half-waves n_h in an attempt to link a characteristic of the instability to the physical parameters of the shock, most notably n_e and T_e. As mentioned in Sec. 2.1.2, because the initial temperature T_1 is fixed (room temperature), the shock wave produced in argon is completely determined by the two independent pressures p_1 and p_4 (from p_{mix}). From these two values one can calculate the shock Mach number M_s (Eq. 2.3), and from the conservation equations and Saha equation all the flow and thermodynamic

variables n_e, n_a, χ, T_a, T_e, etc. Out of this complete set of variables we may choose any two as the independent ones. Thus, to determine a run, that is, determine p_1 and p_4, exactly two of these variables must be chosen. In practise this is how a run was planned.

In view of the importance of n_e and $T_a - T_e$ in the expressions for the energy transfer associated with possible plasma oscillations, each run was planned by choosing the maximum electron number density $n_{e,E}$ at quasi-equilibrium and the frozen temperature $T_{2(fr)}$ behind the translational shock front. Although the value of n_e is zero at the shock front and rises to $n_{e,E}$, it was felt that the magnitude of $n_{e,E}$ would give an indication of n_e throughout the region where $T_a > T_e$. For simplicity, T_a is considered instead of $T_a - T_e$; $T_{2(fr)}$ is the atom temperature immediately behind the shock front for most of the relaxation length (Ref. 2), so T_a may be approximated by $T_{2(fr)}$. Since $T_{2(fr)}$ is just the perfect-gas temperature behind the shock front, it depends only on M_s since T_1 is practically fixed. This justifies choosing $n_{e,E}$ and M_s as the independent parameters of the shock. The value of p_1 was found from thermodynamic tables, and p_4 was obtained from Eq. 2.3. The experiment was then performed, and the observed M_s and initial pressure p_1 were measured (with accuracies given in Sec. 2.1.4). To add the experimental data to Fig. 30, a thermodynamic routine was used to calculate $n_{e,E}$ from these, and a symbol representing the value of n_h observed from the schlieren picture was placed at the point given by M_s and $n_{e,E}$ (all three for each run are given in Tables 1 and 2). In this way trends regarding the values of $n_{e,E}$ and M_s for one value of n_h would be seen. Figure 14 serves to give the region containing values of $n_{e,E}$ and M_s attainable, consistent with the constraints of the driver [$p_4 \leq 443$ atm (6500 psi)], the shock detectors ($p_1 \geq 1$ torr), and the test-section windows [$p_2 \leq 6.8$ atm (100 pse)]. As well, experiments were designed to get sample experiments from as many parts of the $n_{e,E} - M_s$ plane as possible, in order to obtain comprehensive data on the phenomenon. It must be emphasized here that the position of a plotted point in Fig. 30 has significance only with regard to the value of n_h. Thus, curves formed by points with different values of n_h have no meaning, whereas a distribution of points with the same n_h suggests a relationship amongst $n_{e,E}$, M_s and n_h.

Some trends can immediately be observed from Fig. 30. For some constant M_s, n_h increases with $n_{e,E}$ almost in proportion. Second, for some constant $n_{e,E}$, n_h increases with M_s. Remember that the uncertainty of n_h is ±1.

Despite the scatter of points with the same value of n_h, a general relationship amongst n_h, $n_{e,E}$, and M_s can also be seen. Its most conspicuous manifestation is the accumulation of $n_h = 6$ in the upper-right corner of the concentration of $n_h = 2$ in the lower-left. These distributions are reflected in the diagonal lines, one for each n_h, drawn such that an equal number of points with that value of n_h fall on either side. A regularly spaced progression from $n_h = 1$ in the lower-left to $n_h = 6$ at the upper-right is indicated, except for $n_h = 4$. Other than this anomaly, it seems that the value of n_h can be predicted for a given experiment within ±1 in this facility given the value of $n_{e,E}$ and M_s. If the $p_1 - p_4$ grid from Fig. 14 is superposed on Fig. 30, n_h can be predicted within ±1 in terms of the initial experimental pressures p_1 and p_4.

Formulating this prediction in terms of the straight lines in Fig. 30 (analogous to n_h "contours") would result in equations with no physical

foundation. This would be remedied by determining: 1) the physical process which gives rise to the instabilities: 2) the dependence of this process upon the various parameters such as n_e, n_a, χ, T_e, and T_a; and 3) the link between the instability characteristic n_h and the relevant parameters. No solution to these steps is offered here. To investigate n_h as a function of these variables several combinations of n_e, n_a, T_e, and T_a were considered keeping in mind their roles in the previously-mentioned energy transfer rates, Comparing the values of these expressions over runs with the same observed n_h met with less success than the simple graphical predictor of Fig. 30. However, the possibilities are by no means exhausted.

As a predictor of the geometry of the nonplanarity of the shock front from given $n_{e,E}$ and M_s, Fig. 30 applies only to this shock tube facility. A more universal indicator would be the wavelength of the sinusoidally curved shock-front disturbance, given by $\lambda = 2L/n_h$, where L is the channel height. The physical meaning of λ is more amenable to nonintegral values of n_h, which woule contradict the wall condition but would be no more troublesome than the travelling-wave model. If λ is used instead of n_h then a quantitative comparison could be made with other shock tubes. Thus it seems reasonable that in a smaller shock tube say with, a channel height of L = 6 cm one would observe $n_h = 2$ for a shock wave that in this facility would appear as $n_h = 6$, the wavelength λ of the disturbance being the same. The values of λ are listed for each run in Table 3.

In Table 3 are listed the apparent periods of oscillation of the shock-front instability. Each travelling wave has a period of about 15 μs. Three standing waves have periods of the magnitude 50 – 90 μs and lower n_h, whereas the other two have periods also near 15 μs with $n_h = 6$. Note that the longest periods are for runs with the lowest $n_{e,E}$, whereas the shortest period occurs for the run with the highest $n_{e,E}$ and a measureable period. This observation is consistent with the notion that a higher electron number density in the reacting region of the shock would increase the rate of energy transfer to the electrons. No such correlation can be seen using the amplitude.

Conclusions:

1) It is possible to obtain multiple short-duration monochromatic light pulses from a ruby laser in a combined giant-pulse/normal-lasing mode with a flash-lamp pumping time of about 500 μs, the first two pulses consistently being about 7 μs apart.

2) Using a very sensitive schlieren system with a dark background, this light source can be used to photograph a high-speed low-density ionizing shock wave in argon at two discrete times. This apparatus was used to investigate the time-dependent behaviour of the unstable translational shock front observed in ionizing shocks in argon.

3) The shock-front nonplanarities, which consistently appear as smooth sinusoidal curves, were observed to change in time either like a travelling wave or like a standing wave, with periods of oscillation decreasing and number of wavelengths increasing with increasing $n_{e,E}$.

36

4) A comprehensive series of experiments led to a graphic predictor designed to give within ±1 the number of half-waves in the nonplanar front of a given shock wave in argon. In terms of wavelength of the sinusoidal disturbances, the predictor might be applied to other facilities.

5) An extensive system of transverse waves was observed behind some of the curved shock fronts. A possible hydrodynamic explanation is given which relates these waves directly to the geometry of the shock front.

6) Additional analyses are required in order to explain this phenomenon in terms of the ionizing shock properties and the experimental data obtained in the present investigation.

REFERENCES

1. Bristow, M. P. F.   "An Experimental Determination of the Polarizability for Singly Ionized Argon", UTIAS Report No. 158, 1971.

2. Glass, I. I.
   Liu, W. S.   "Effects of Hydrogen Impurities on Shock Structure and Stability in Ionizing Monatomic Gases: I - Argon", Journal of Fluid Mechanics, Vol. 84, Pt. 1, Pg 55-77, (1978).

3. Glass, I. I.
   Liu, W. S.
   Tang, F. C.   "Effects of Hydrogen Impurities on Shock Structure and Stability in Ionizing Monatomic Gases: 2. Krypton", Can. Jour. Physics, Vol. 55, No. 14, 1977, 1269-1279

4. Glass, I. I.
   Hall, J. G.   "Handbook of Supersonic Aerodynamics, Section 18, Shock Tubes", NAVORD Report 1488 (Vol. 6), Bureau of Naval Weapons, 1959.

5. Bose, T. K.
   Kannappan, D.   "Transport Properties of a Two-temperature Argon Plasma", The Physics of Fluids, Vol. 20, No. 10, Pt. 1, Oct. 1977, Pg 1668-1673.

6. Petschek, H.
   Byron, S.   "Approach to Equilibrium Ionization Behind Strong Shock Waves in Argon", Annals of Physics, Vol. 1, No. 3, Pg. 270, 1957.

7. Morse, P. M.
   Ingard, K. U.   "Theoretical Acoustics", McGraw-Hill, New York, 1968.

8. Igra, O.   "An Experimental Investigation of a Nonequilibrium Corner-expansion Flow of Ionized Argon", UTIAS Report No. 161, 1970.

9. Brimelow, P. I.   "An Interferometric Investigation of Shock Structure and Its Induced Shock-tube Boundary Layer in Ionized Argon", UTIAS Technical Note No. 187, 1974.

10. Tang, F. C.   "Effects of Impurities on Shock-Wave Stabilities and Structure in Ionizing Moatomic Gases", UTIAS Technical Note No. 212, 1977.

11. Liu, W. S.   "An Analysis of Shock Structure and Nonequilibrium Laminar Boundary Layers Induced by a Normal Shock Wave in an Ionized Argon Flow", UTIAS Report No. 198, 1975.

12. Liu, W. S.
    Whitten, B. T.
    Glass, I. I.   "Ionizing Argon Boundary Layers. Part 1. Quasi-Steady Flat-Plate Laminar Boundary-Layer Flows", J. Fluid Mech. (1978), Vol. 87, Part 4, 609-640.

13. Glass, I. I.
    Liu, W. S.   "Effects of Hydrogen Impurities on Shock Structure and Stability in Ionizing Monatomic Gases. Part 1. Argon", J. Fluid Mech. (1978), Vol. 84, Part 1, 55-77.

14. Liu, W. S.   "Coupled Interactions of Shock-Wave Structure with
    Takayama, K.   Laminar Boundary Layer in Ionizing Argon Shock-Tube
    Glass, I. I.   Flows", J. Fluid Mech. Vol. 97, Part 3, 1980, 513-530.

15. Glass, I. I.   "Effect- of Hydrogen Impurities on Shock Structure and
    Liu, W. S.   Stability in Ionizing Monatomic Gases: 2. Krypton",
    Tang, F. C.   Can. Jour. Physics, Vol. 55, No. 14, 1977, 1269-1279.

16. Ben-Dor, G.   "Domains and Boundaries of Non-Stationary Oblique
    Glass, I. I.   Shock-Wave Reflections. 1. Diatomic Gas", J. Fluid
                      Mech. (1979), Vol. 92, Part 3, pp. 459-496.

17. Ben-Dor, G.   "Domains and Boundaries of Non-stationary Oblique Shock-
    Glass, I. I.   Wave Reflections: II. Monatomic Gas", Journal of
                      Fluid Mechanics.

18. Ben-Dor, G.   "Regions and Transitions of Non-stationary Oblique
                      Shock-Wave Reflections in Perfect and Imperfect Gases",
                      UTIAS Report No. 232, 1978.

19. Ben-Dor, B   "Interferometric Techniques and Data Evaluation Methods
    Whitten, B. T.   for the UTIAS 10 cm x 18 cm Hypervelocity Shock Tube",
                      UTIAS Tech. Note No. 208, 1979.

20. Hall, J. G.   "The Design and Performance of a 9 inch Plate Mach-
                      Zehnder Interferometer", UTIA Report No. 27, 1954.

21. Holder, D. W.   "Schlieren Methods", NPL Note on Applied Science,
    North, R. J.   No. 31, 1963.

22. Boyer, A. G.   "Design, Instrumentation and Performance of the 4 x 7
                      Inch Shock Tube", UTIAS Report No. 99, 1965.

23. Oettinger, P. E. "A Unified Treatment of the Relaxation Phenomena in
    Bershader, D.   Radiating Argon Plasma Flows", AIAA Journal, Vol. 5,
                      No. 9, Pg 1625, 1967.

24. Alpher, R. A.   "Optical Refractivity of High-Temperature Gases.
    White, D. R.   II. Effects Resulting from Ionization of Monatomic
                      Gases", The Physics of Fluids, Vol. 2, No. 2, Pg 162,
                      1959.

25. Belozerov, A. N. "Study of the Initial Ionization Process in a Strong
    Measures, R. M.   Shock Wave", Journal of Fluid Mechanics, Vol. 36,
                      Pt. 4, Pg 695, 1969.

26. Lapworth, K. C.   "An Experimental Investigation of the Stability of
                      Plane Shock Waves", Journal of Fluid Mechanics, Vol. 6,
                      Pt. 3, Pg 469, 1959.

27. Whitham, G. B.   "Linear and Nonlinear Waves", John Wiley and Sons,
                      New York, 1974.

28. White, D. R.   "Turbulent Structure of Gaseous Detonation", Physics of Fluids, Vol. 4, No. 4, Pg 465, 1961.

29. Lengyl, B. A.   "Introduction to Laser Physics", Hohn Wiley and Sons, New York, 1966.

30. de Leeuw, J. H.   "A High-Speed Multi-Source Spark Camera", UTIA Tech.
    Glass, I. I.   Note No. 26 (1962)
    Heuckroth, L. E.

31. Urtiew, P. A.   "Experimental Observations of the Transition to
    Oppenheim, A. K.   Detonation in an explosive Gas", Communicated by Sir Owen Saunders, F. R. S., Proc. Roy. Soc., A, 295, pp. 13-28 (1966).

32. Lee, J. H.   "Current Views on Gaseous Detonation", Astronatica
    Soloukhin, R. I.   Acta, Vol. 14, 565-584 (1969).
    Oppenheim, A. K.

33. Oppenheim, A. K.   "On the Use of Laser Light Sources in Schlieren-
    Urtiew, P. A.   Interferometer Systems", Proc. Roy. Soc., A, 291,
    Weinberg, F. J.   pp. 279-289 (1966).

34. Sedney, R.   "Conventional Flow Visualization Using Laser Light
    Rowe, R.   Source", AIAA Paper No. 66-127 (1966).
    Bush, C.
    Voelker, L.

35. Freeman, N. C.   "A Theory of the Stability of Plane Shock Waves", Proceedings of the Royal Society A, Vol. 228, pp. 341-362 (1955).

36. Freeman, N. C.   "On the Stability of Plane Shock Waves", Journal of Fluid Mechanics, Vol. 2, pp. 397-411 (1957).

37. D'Iakov, P.   "The Interaction of Shock Waves with Small Perturbations. I and II", JETP, Vol. 6 (33), No. 44, pp. 729-747 (1958).

38. Fowles, G. R.   "Shock Wave Stability", The Physics of Fluids, Vol. 18,
    Swan, G. W.   No. 1, pp. 28-34 (1975).

39. Griffiths, R. W.   "Stability of Shock Waves in Ionizing and Dissociating
    Hornung, H. G.   Gases", J. Phys. D: Appl. Phys. Vol. 9, pp. 1681-1691 (1976)
    Sandeman, R. J.

40. Paullay, A. J.   "Stability of Normal Shock Waves with Viscosity and
    Morduchow, M.   Heat Conduction", The Physics of Fluids, Vol. 14, No. 2, pp. 323-331 (1971).

41. Fowles, G. R.   "Conditional Stability of Shock Waves--a Criterion for Detonation", The Physics of Fluids, Vol. 19, No. 2, pp. 227-238 (1976).

42. Erpenbeck, J. J.   "Stability of Step Shocks", The Physics of Fluids,
                         Vol. 5, No. 10, 1181-1187 (1962).

43. Cowperthwaite, M.   "Properties of Some Hugoniot Curves Associated with
                         Shock Instability", Journal of the Franklin Institute,
                         Vol. 285, No. 4, pp. 275-284 (1968).

44. Goulard, R.   "Structure of Shock Waves with Nonequilibrium Radiation
    Nelson, H. F.   and Ionization", The Physics of Fluids, Vol. 12, No. 8,
                         pp. 1605-1617 (1969).

45. Srinivasan, J.   "Criteria for Acoustic Instability in a Gas with Ambient
    Vincenti, W. G.   Vibrational and Radiative Nonequilibrium", The Physics
                         of Fluids, Vol. 18, No. 12, pp. 1670-1677 (1975).

46. Ingard, U.   "Acoustic Wave Generation and Amplification in a Plasma",
                         Physical Review, Vol. 145, No. 1, pp. 41-46 (1966).

PARAMETERS OF NONPLANAR SHOCKS TRAVELLING IN ARGON

TABLE 1   OBSERVED BY SINGLE-EXPOSURE INTERFEROMETRIC METHOD

#	M_s	P_1 (Torr)	n_{eE} (10^{17} cm^{-3})	n_h	T_1 (°K)	T_{2f} (°K)	T_{2e} (°K)	P_{2f} (psi)	P_{2e} (psi)	X
P1	14.77	3.95	0.951	5	297.6	20,500	12,200	20.9	23.8	0.108
P2*	13.03	9.97	1.034	2	298.9	16,100	11,800	40.9	45.0	0.057
P3	13.91	6.49	1.060	2	297.5	18,300	12,100	30.4	34.1	0.081
P4	16.02	3.01	1.109	5	297.6	24,100	12,600	18.7	21.7	0.148
P5	17.19	2.24	1.166	6	297.6	27,700	12,900	16.1	18.9	0.189
P6	13.21	11.48	1.257	3	297.6	16,500	11,900	48.4	53.4	0.060
T1	17.2	2.47	1.26	6	297.4	27,700	12,900	17.6	20.8	0.187
T2	17.3	2.51	1.32	4	297.9	28,100	13,000	18.1	21.4	0.192
T3	15.8	5.14	1.66	4	297.6	23,500	12,800	31.0	35.8	0.136
T4	16.1	5.15	1.81	6	296.1	24,200	13,000	32.2	37.4	0.144
T5	16.12	5.15	1.82	4	295.9	24,300	13,000	32.4	37.6	0.144
T6	16.35	5.19	1.98	6	298.0	25,100	13,100	33.5	39.1	0.153
B1	13.0	4.50	0.511	2	296.5	15,900	11,300	18.4	20.3	0.061
B2	14.7	4.08	0.954	3	298.0	20,400	12,200	21.3	24.3	0.106
B3	17.0	2.33	1.137	2	295.6	26,900	12,800	16.3	19.1	0.180
B4	18.0	1.84	1.165	5	274.7	30,100	13,000	14.4	17.1	0.216
B5	18.0	1.90	1.202	5	295.3	30,100	13,000	14.9	17.7	0.216
B6	17.1	2.45	1.236	6	298.7	27,500	12,900	17.3	20.4	0.186
B7	17.0	2.65	1.278	5	295.9	27,000	12,900	18.5	21.8	0.179
B8	16.9	2.84	1.323	4	295.7	26,600	12,900	19.6	23.0	0.175
B9	17.2	2.60	1.330	6	297.5	27,700	13,000	18.6	21.9	0.187
B10	13.8	9.61	1.391	2	295.6	17,800	12,200	44.2	49.3	0.074

P - present study; T - Experiments of Tang (Ref. 10); B - Experiments of Bristow (Ref. 1).

*Single-exposure schlieren; n_h - see Table 3.

PARAMETERS OF NON-PLANAR SHOCKS TRAVELLING IN ARGON

OBSERVED BY THE MULTIPLE-EXPOSURE SCHLIEREN METHOD

TABLE 2

Run #	M_s	P_1 (Torr)	n_{eE} (10^{17} cm^{-3})	n_h	T_1 (°K)	T_{2f} (°K)	T_{2e} (°K)	P_{2f} (psi)	P_{2e} (psi)	X
1	11.79	7.00	0.366	2	296.2	13,100	10,700	23.5	25.2	0.032
2	11.52	9.98	0.414	1	299.2	12,700	10,700	32.0	34.0	0.027
3	15.06	1.39	0.418	2	298.1	21,400	11,700	7.62	8.83	0.125
4	12.32	7.47	0.563	2	300.1	14,500	11,200	27.4	29.8	0.044
5	14.33	2.66	0.574	3	297.8	19,400	11,800	13.2	15.0	0.099
6	13.70	4.30	0.687	1	298.7	17,800	11,700	19.5	22.0	0.079
7	14.48	3.18	0.715	2	299.0	19,800	12,000	16.1	18.4	0.103
8	14.38	4.11	0.852	3	297.0	19,400	12,000	20.5	23.4	0.096
9	11.61	25.88	0.900	2	296.7	12,800	11,100	84.3	88.8	0.023
10	12.71	11.52	0.983	2	298.1	15,300	11,600	44.9	49.1	0.049
11	11.93	21.04	0.993	2?	298.3	13,500	11,300	72.3	77.1	0.030
12	16.23	2.61	1.041	5	298.5	24,800	12,600	16.6	19.4	0.156
13	12.31	17.04	1.075	2	298.5	14,400	11,500	62.3	67.2	0.038
14	14.35	5.70	1.143	4	300.4	19,600	12,200	28.4	32.2	0.095
15	14.06	7.38	1.245	3	296.7	18,600	12,200	35.2	39.6	0.083
16	14.72	5.48	1.262	3	300.4	20,600	12,400	28.7	32.7	0.106
17	15.29	6.12	1.668	5	298.6	22,100	12,700	34.6	39.7	0.120
18	17.78	3.14	1.816	6	298.2	29,700	13,300	24.0	28.4	0.206
19	14.39	10.13	1.885	4	298.6	19,600	12,600	50.7	57.2	0.091
20	16.10	5.79	2.040	6	299.4	24,500	13,100	36.3	42.1	0.145
21	14.50	11.35	2.190	5	300.1	20,000	12,700	57.7	65.2	0.094
22	14.38	13.25	2.360	6	298.6	19,500	12,700	66.2	74.4	0.088
23	14.51	12.96	2.415	6	297.5	19,800	12,800	65.9	74.3	0.091

GEOMETRICAL PARAMETERS OF THE
TIME-DEPENDENT SHOCK-WAVE NONPLANARITIES

TABLE 3

Run # from Table 2	t_p (μs)	n_s	Δt (μs)	max g (mm)	n_h	λ (cm)	T (μs)	Wave Type
1	482	2	7.58	0.7	2	17.8		
2	479	4	6.86	1.8	1	35.6	48.	S
3	548	1		1.5	2	11.8		
4	492	3	6.78	1.5	2	17.8		S (or T)
5	490	1		0.8	3	11.7		
6	536	1		1.5	1	35.6		
7	490	3	6.57	3.2	2	17.8	59.	S
8	504	1		1.6	3	11.8		
9	443	7	6.99	1.0	2	17.8		
10	511	2	12.	1.0	2	17.8		S
11	490	3	7.57	1.7	2	17.8		
12	510	2	7.80	1.6	5	17.1		
13	446	3	6.64	3.3	2	17.8		S
14	493	2	7.87	1.5	4	8.9		S?
15	477	3	6.94	2.2	3	11.8	88.?	S
16	477	2	7.37	1.2	3	11.8	16.3	T
17	462	2	7.42	1.4	5	7.1		S?
18	501	2	8.1	1.0	6	5.9	16.	S
19	483	4	7.74	1.4	4	8.9		
20	496	3	7.37	1.6	6	5.9	15.	S
21	467	5	7.44	1.8	5	7.1	15.3	T
22	512	4	7.98	1.7	6	5.9	14.6	T
23	515	1		1.2	6	5.9		

t_p - laser flash-lamp pumping time; n_s - number of visible shock images;

Δt - time between P_1 and P_2; n_h - number of half-wavelengths;

T - possible period of sinusoidal non-planarity;

Wave Type - standing (S) or travelling (T) sinusoidal wave.
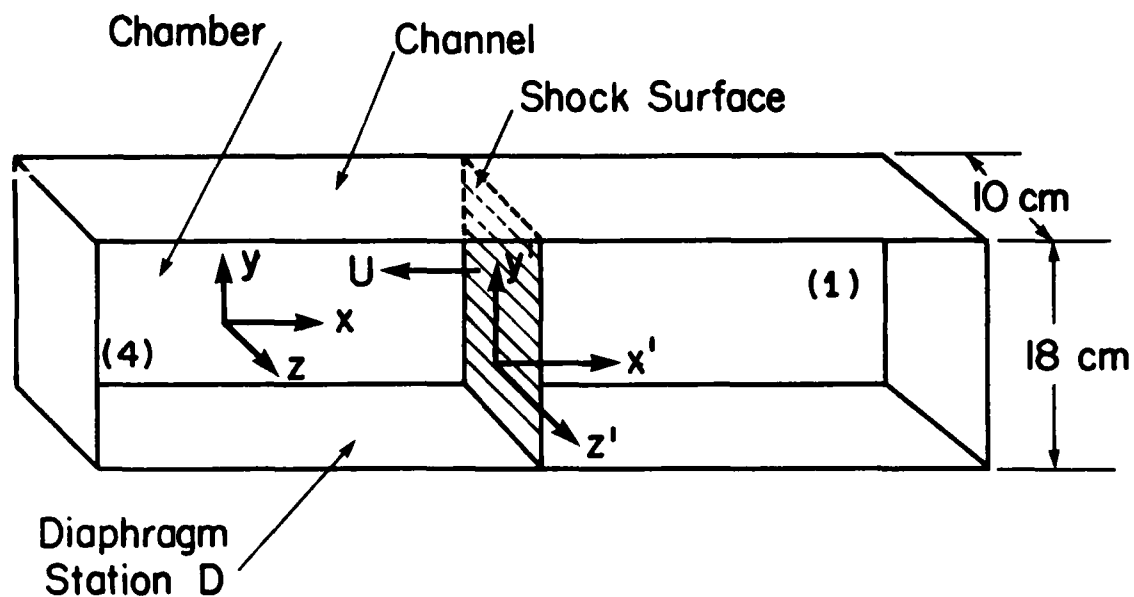
FIG. 1.   COORDINATE SYSTEMS IN THE SHOCK TUBE. x,y,z: LABORATORY
           COORDINATES. x',y',z': SHOCK-FIXED COORDINATES.
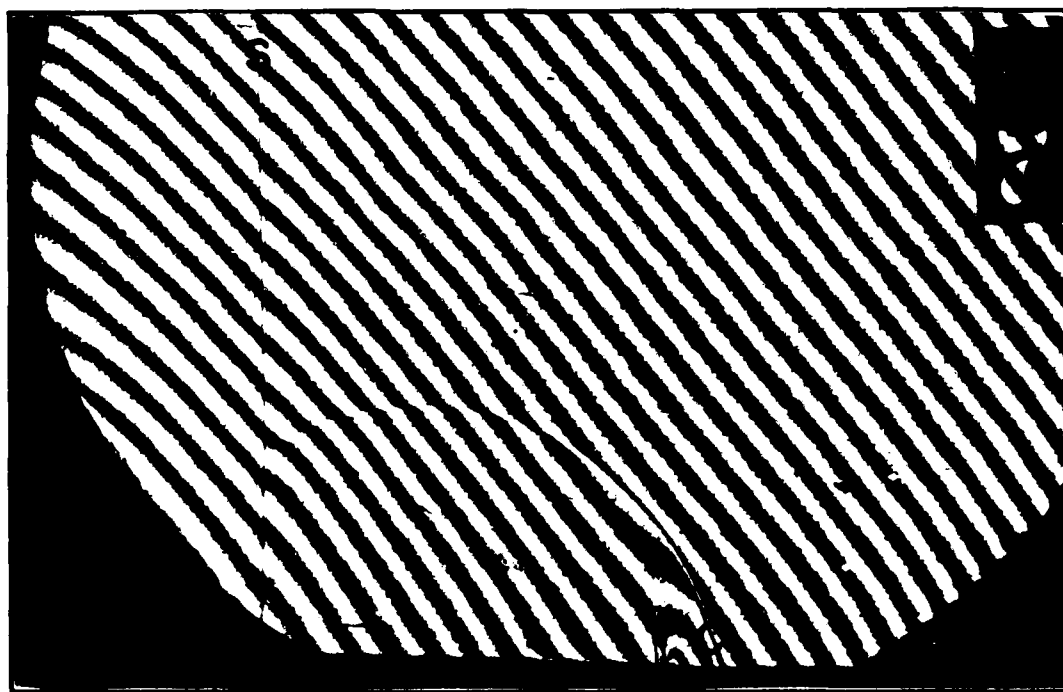
FIG. 2.   INTERFEROGRAM OF THE ONE AND TWO-DIMENSIONAL SHOCK FRONTS IN
           A SHOCK TUBE (REF. 18). S - STRAIGHT ONE-DIMENSIONAL SHOCK
           WAVE (FRINGE SHIFT IS NEARLY AN INTEGER). C - CURVED TWO-
           DIMENSIONAL SHOCK WAVE.
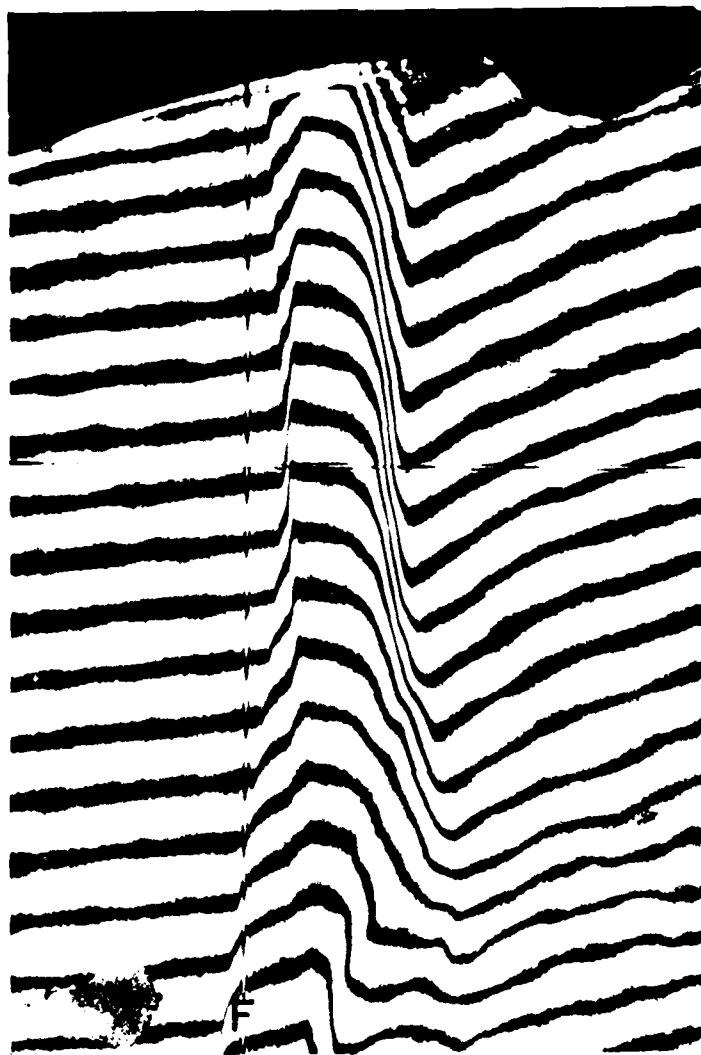
FIG. 3 INTERFEROGRAM OF A THREE-DIMENSIONAL SHOCK FRONT MOVING LEFT
IN IONIZING KRYPTON. NOTE THE 'TWISTED RIBBON' APPEARANCE
OF THE TRANSLATIONAL SHOCK FRONT. THE SHOCK SURFACE DEPENDS
ON x', y', AND z' (REF. 10).
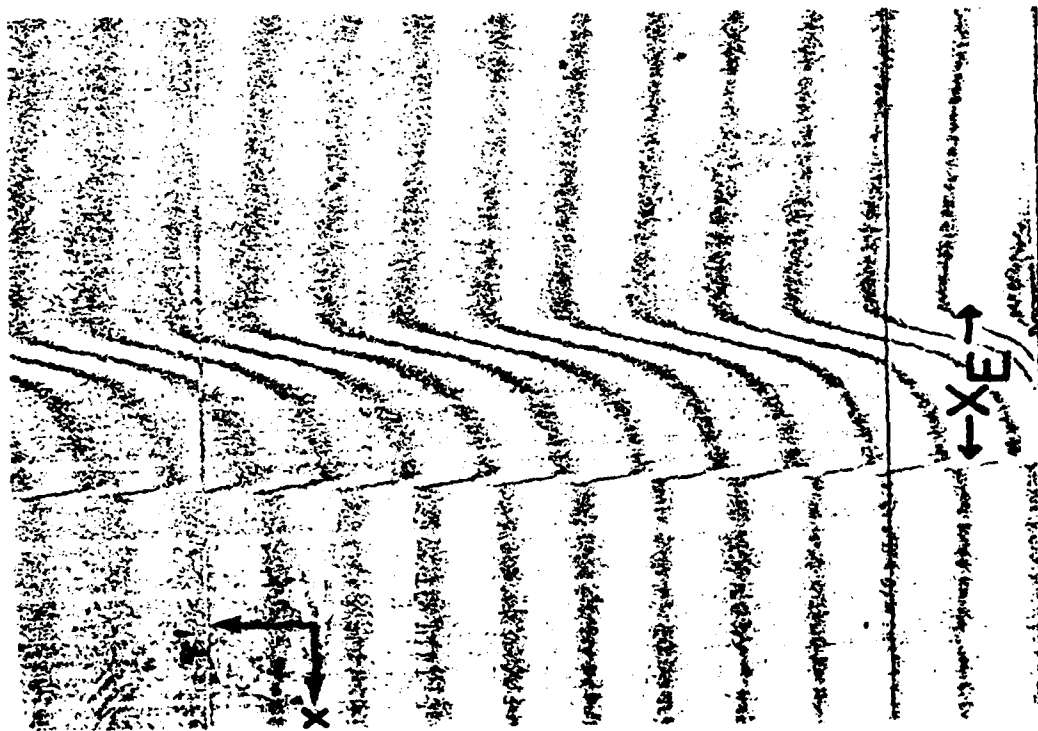
FIG. 4.   CONGRUENT FRINGES PRODUCED BY PLANAR SHOCK FRONT IN IONIZING ARGON MOVING LEFT (REF. 10).
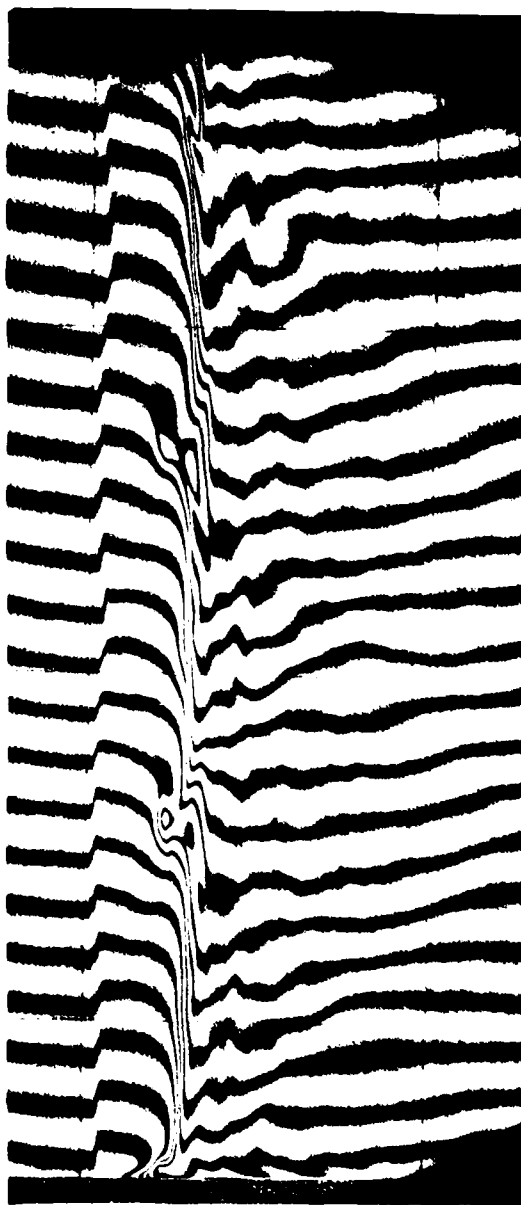
FIG. 6 NON-PLANAR SHOCK FRONT IN IONIZING ARGON MOVING LEFT
SHOWING SINUSOIDAL OSCILLATIONS (RUN B5 IN TABLE 1).
$M_s = 18.01$, $p_1 = 1.00$ TORR, $T_1 = 295.3°K$.
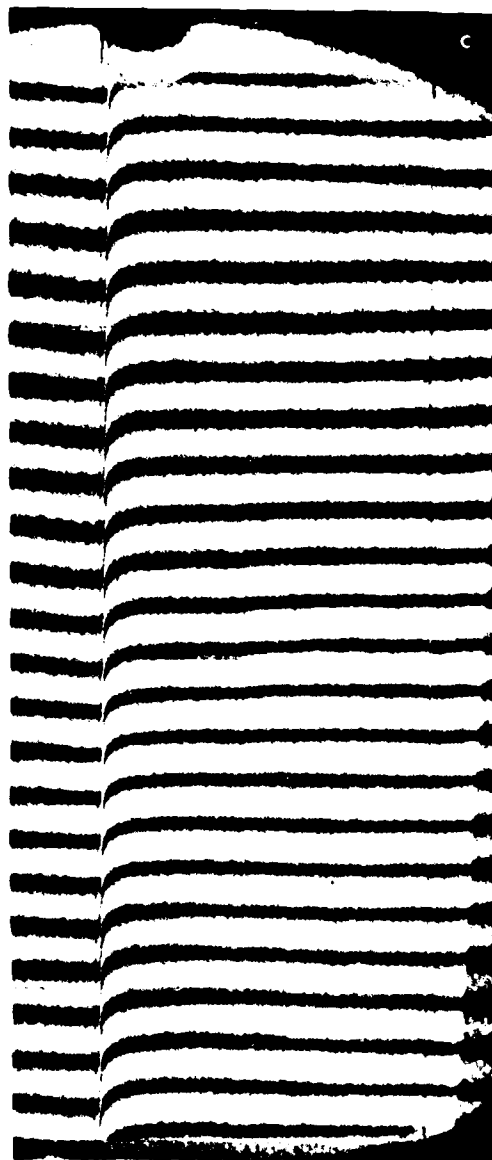
FIG. 6 PLANAR SHOCK WAVE AND INDUCED PLANAR FLOW IN DISSOCIATING NITROGEN (REF. 1). $M_s = 16.6$, $p_1 = 2.26$ TORR, $T_1 = 295.6°K$.
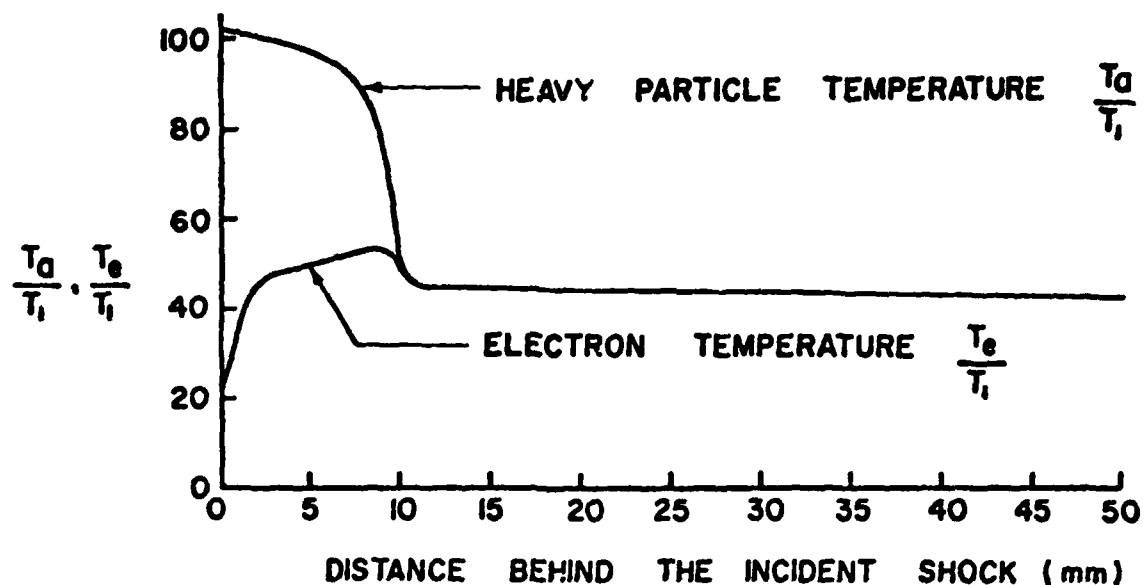
FIG. 7(a)   ATOM TEMPERATURE T_a AND ELECTRON TEMPERATURE T_e BEHIND A
STRONG INCIDENT SHOCK WAVE IN ARGON FOR $M_s = 18.0$, $p_1 =$
3 TORR, $T_1 = 296.5°K$ (REF. 23).
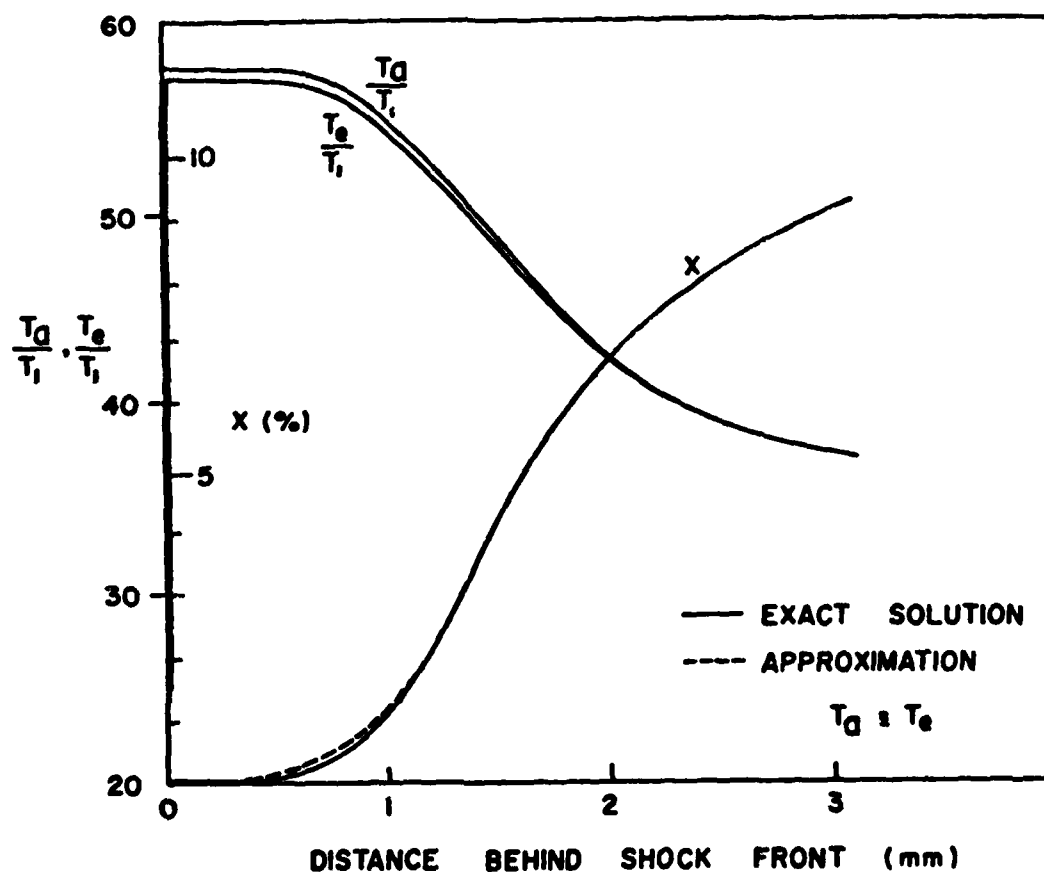
FIG. 7(b)   RATIOS T_a/T_1 AND T_e/T_1, AND DEGREE OF IONIZATION BEHIND A
STRONG INCIDENT SHOCK WAVE IN HYDROGEN FOR $M_s = 25$, $p_1 =$
3 TORR (REF. 25).
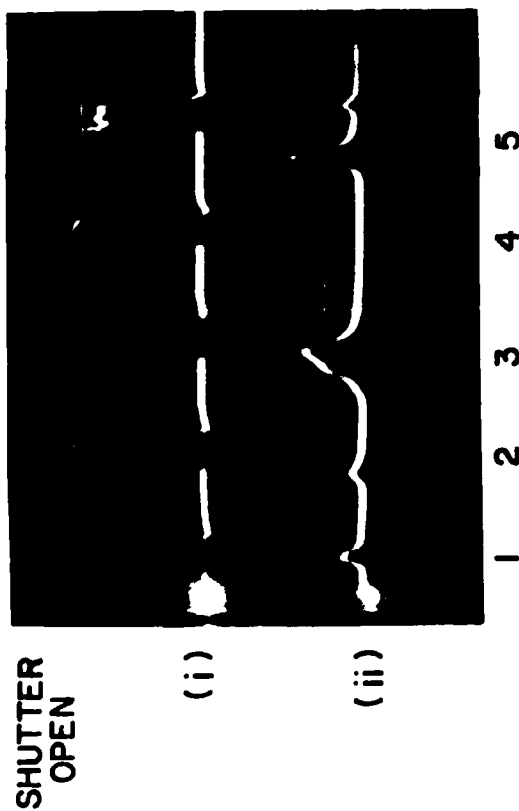
FIG. 8 IMAGE CONVERTER INTERFEROGRAMS OF A TRAVELLING SHOCK WAVE IN ARGON USING A RUBY LASER IN NORMAL-LASING MODE AS A LIGHT SOURCE.

(a) DUAL OSCILLOSCOPE TRACES VS TIME (1.0 µs/div) OF:
(i) FRAMING CAMERA SHUTTER VOLTAGE (5V/div) (SHUTTER IS OPEN AT +10 V AND CLOSED AT 0 V).
(ii) RELATIVE LASER LIGHT INTENSITY PHOTODIODE OUTPUT, 0.02 V/div).

(b) FIVE INTERFEROGRAMS RESULTING FROM (a)

a)   b)
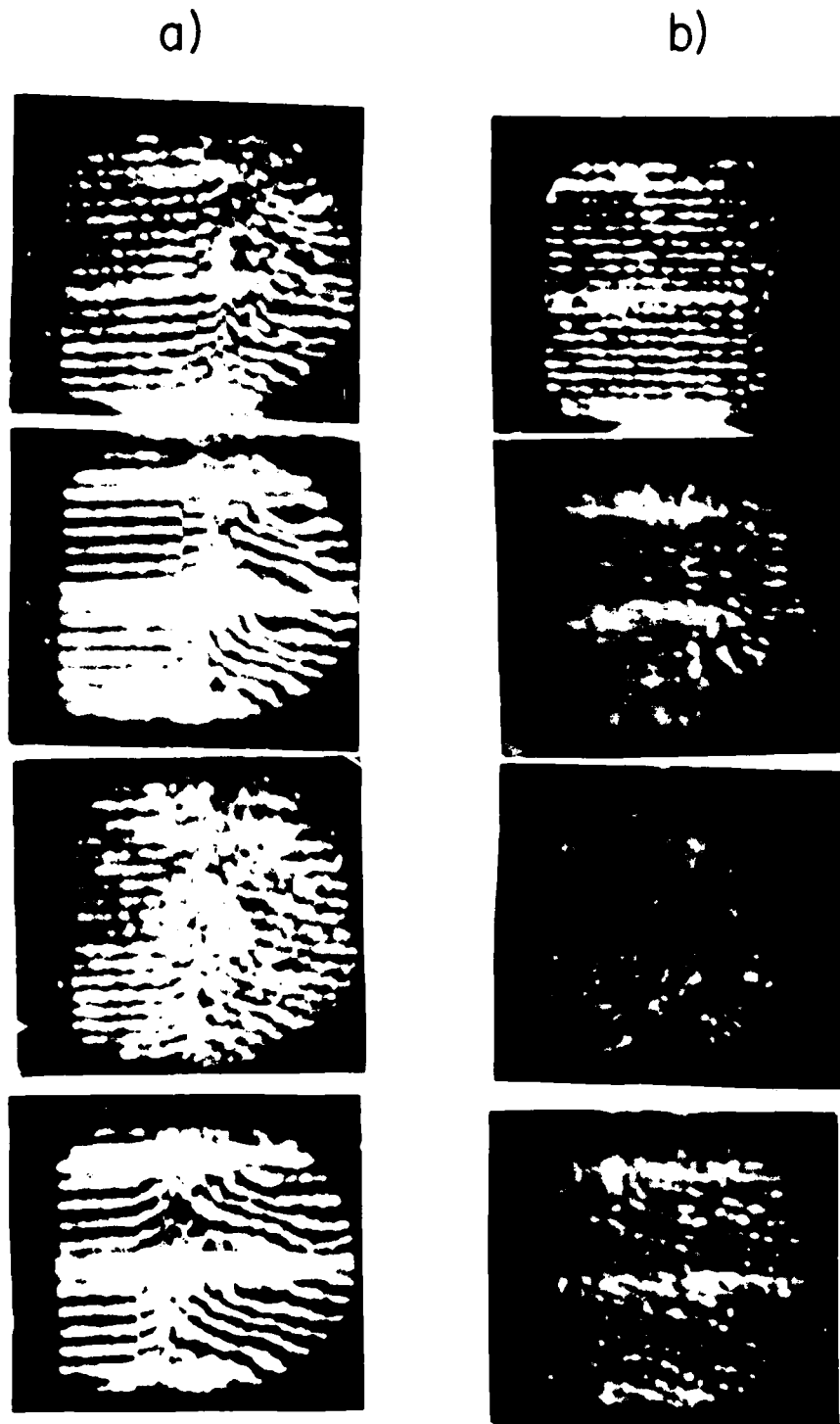
FIG. 7 FOUR INTERFEROGRAMS Δt APART FROM IMAGE CONVERTER CAMERA OF THE
SAME SHOCK WAVE MOVING LEFT INTO ARGON. THE TOP FRAME WAS EXPOSED
FIRST, THE BOTTOM FRAME LAST. EACH CIRCULAR NEGATIVE IMAGE WAS
12 MM IN DIA.

(a) $M_S = 16.2$, $p_1 = 5.15$ TORR, $\Delta t = 2$ μs.
(b) $M_S = 16.35$, $p_1 = 5.11$ TORR, $\Delta t = 7$ μs.

IN EACH RUN THE SHOCK FRONT CAN BE SEEN TO MOVE LEFT FROM THE
TOP TO THE BOTTOM FRAME.

Measured Initial Mixture Pressure $(H_2, O_2, H_e) = 423$ psi (Heise Gauge)
Calculated Diaphragm Bursting Pressure $= 2452$ psi

Final Combustion Pressure

Arrival of Rarefaction Wave after Diaphragm Burst

5 msec

500 psi

Initial Mixture Pressure

Original Base Line
P = 0
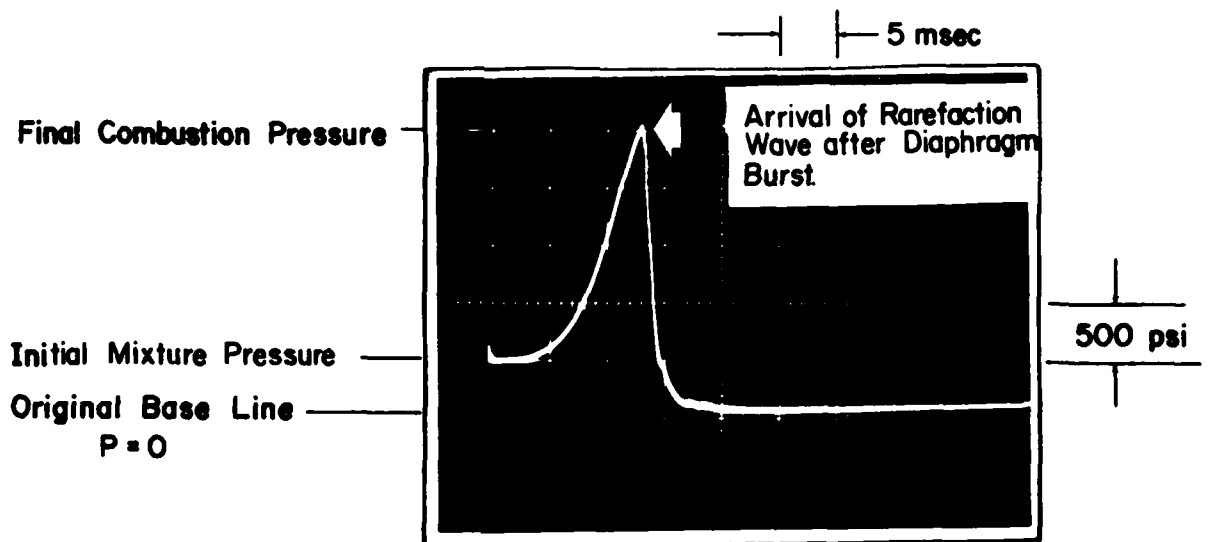
a) DRIVER PRESSURE at CLOSED END

Measured Shock Mach Number $= 15.0$ at Station M
Measured Initial Pressure $P_0 = 6.12$ torr (0.12 psi)

Predicted Equilibrium Pressure = 38.0 psi (1965 torr)

Predicted Frozen Pressure = 33.3 psi (1722 torr)

10 psi

P_0

10 μsec
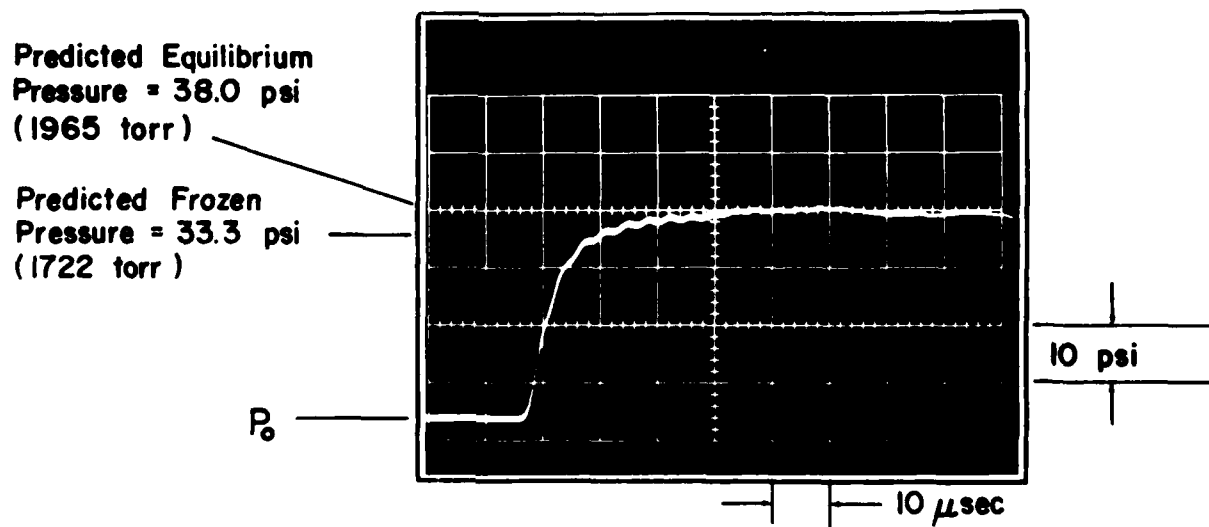
b) SHOCK - WAVE PRESSURE at STATION M

FIG. 10.   PIEZO PRESSURE HISTORIES IN COMBUSTION DRIVER a) AND IN TEST SECTION (b).
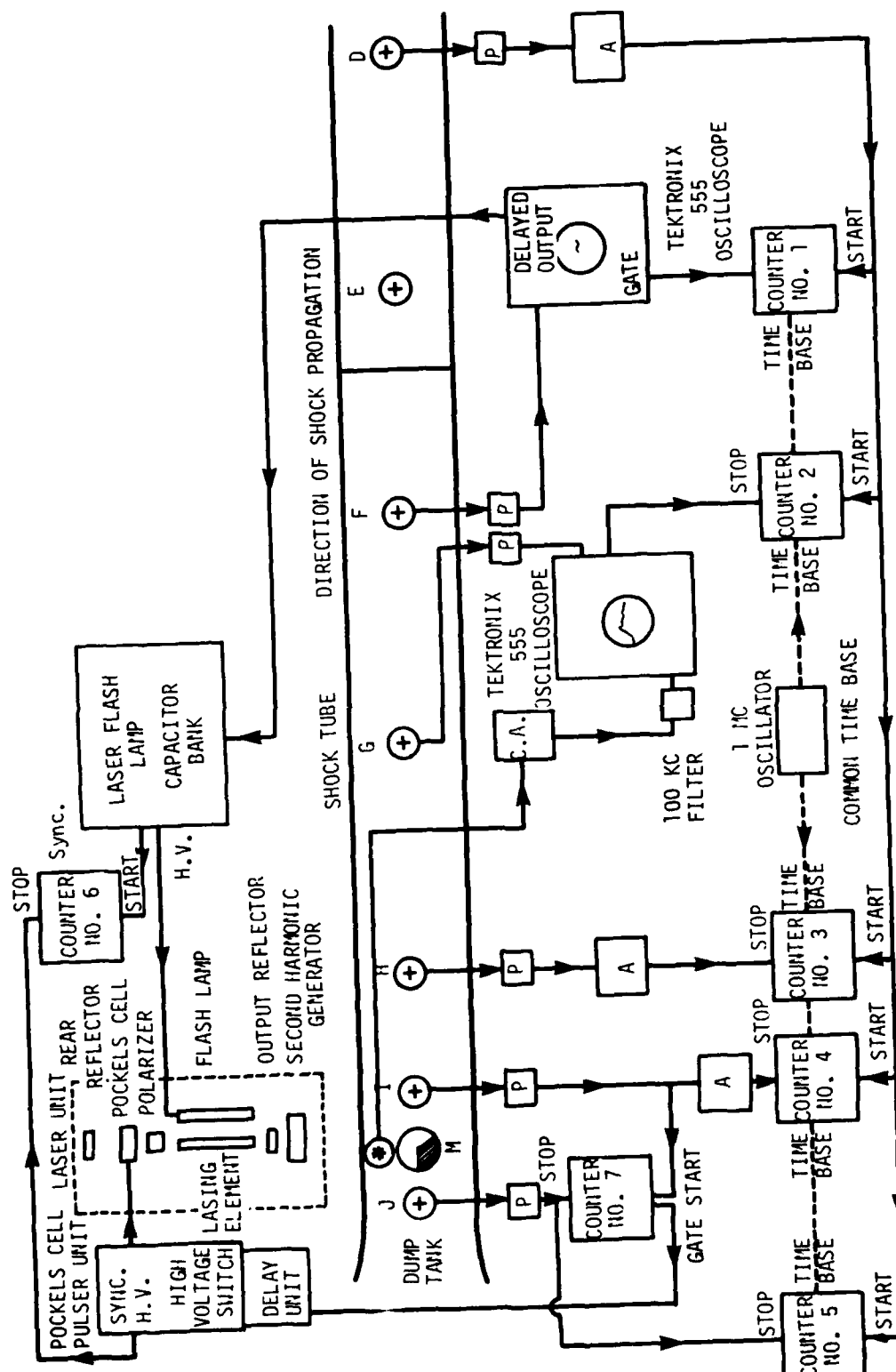
FIG. 11(a) INSTRUMENTATION SET-UP FOR RECORDING THE NONSTATIONARY PHENOMENA IN THE TEST SECTION.
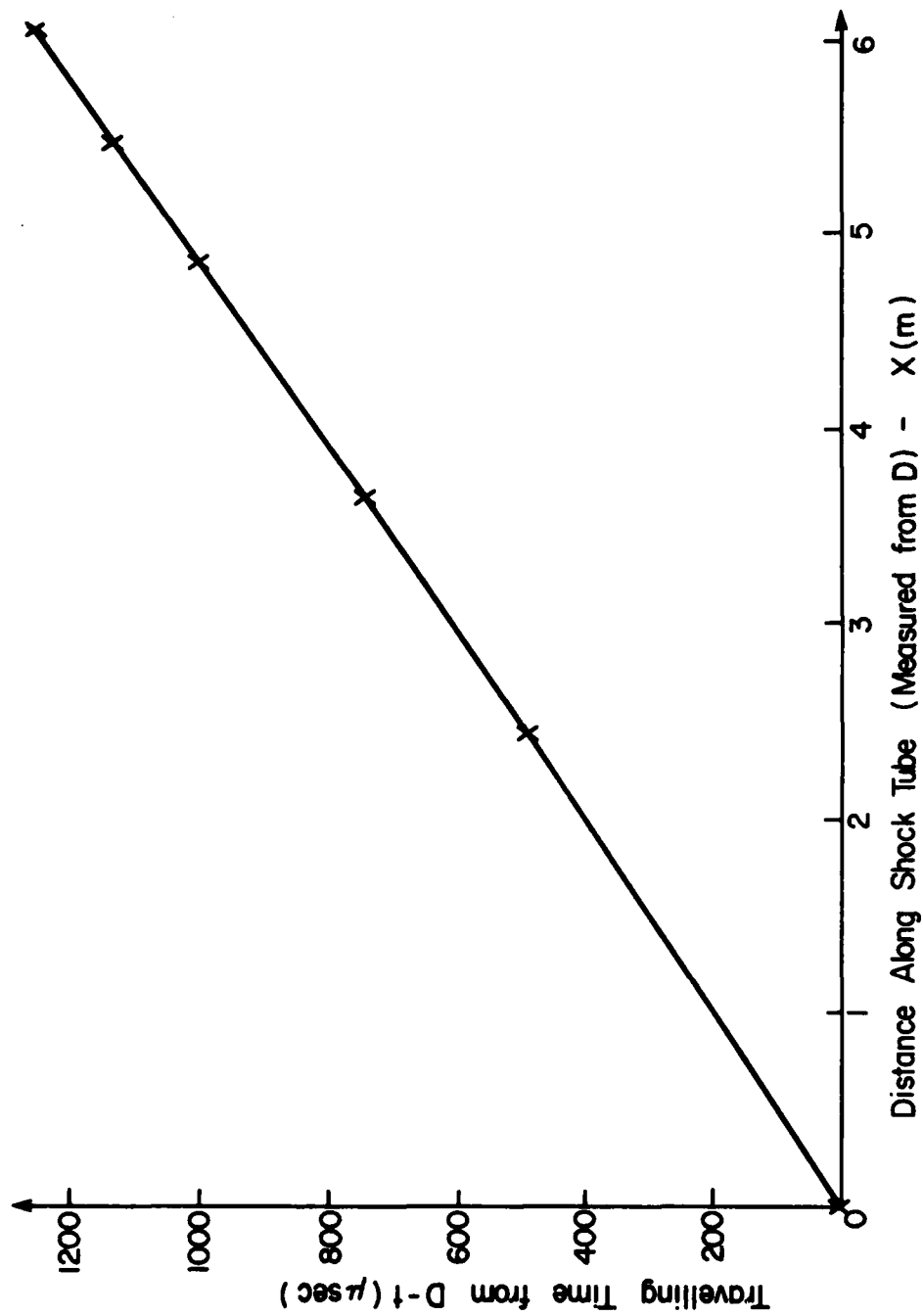
FIG. 11(b) DISTANCE-TIME CURVE OF THE INCIDENT SHOCK-WAVE AS IT MOVES ALONG THE SHOCK TUBE. THE SIX POINTS CORRESPOND TO STATIONS D, F, G, H, I, AND J OF FIG. 11(a). TIMES ARE MEASURED FROM D. THE SOLID LINE REPRESENTS THE BEST FIT ACROSS THESE MEASUREMENTS. THE VELOCITY OF THE INCIDENT SHOCK-WAVE AT ANY POINT IS dx/dt.
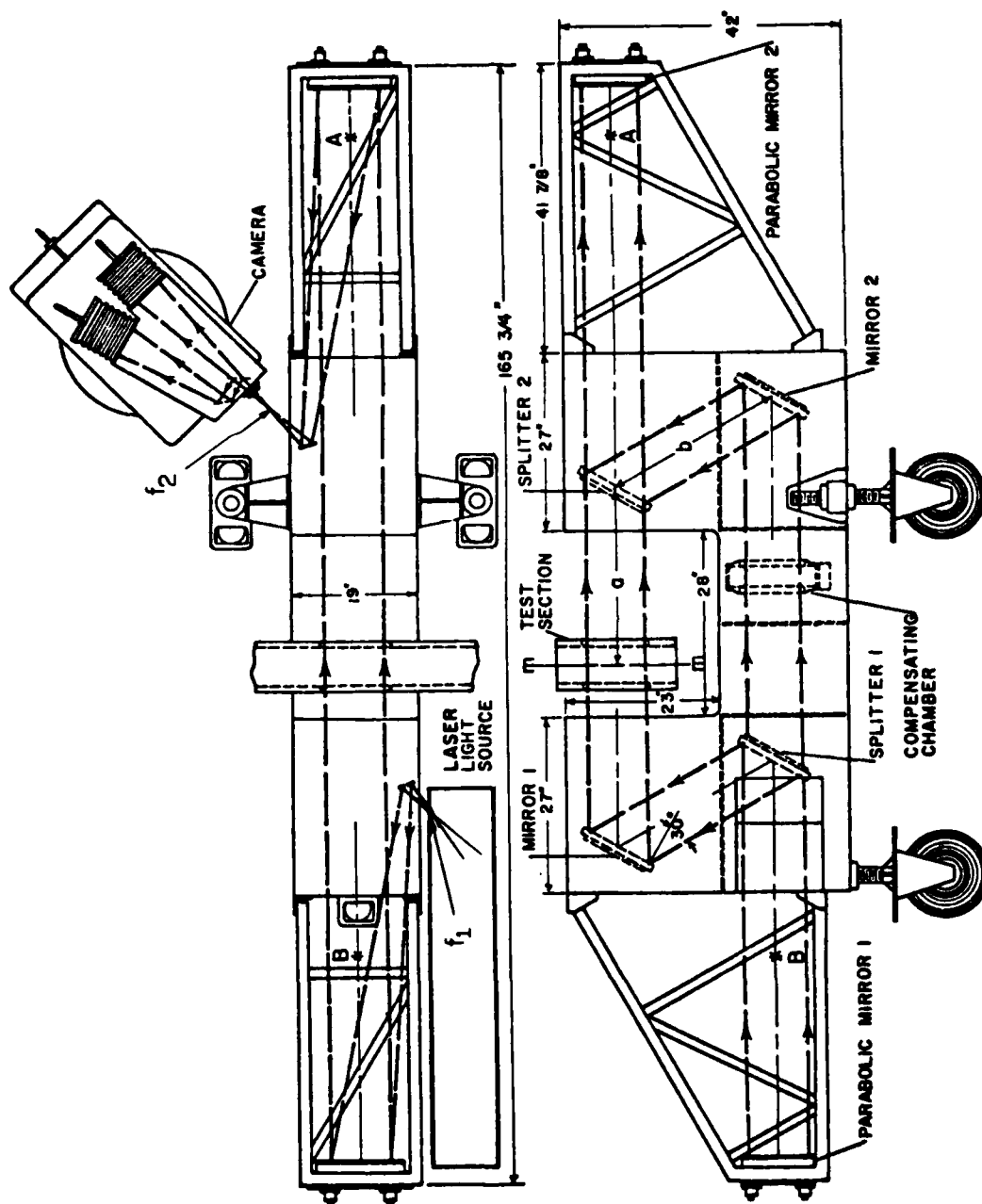
FIG. 12 SCHEMATIC OF MACH-ZEHNDER INTERFEROMETER.
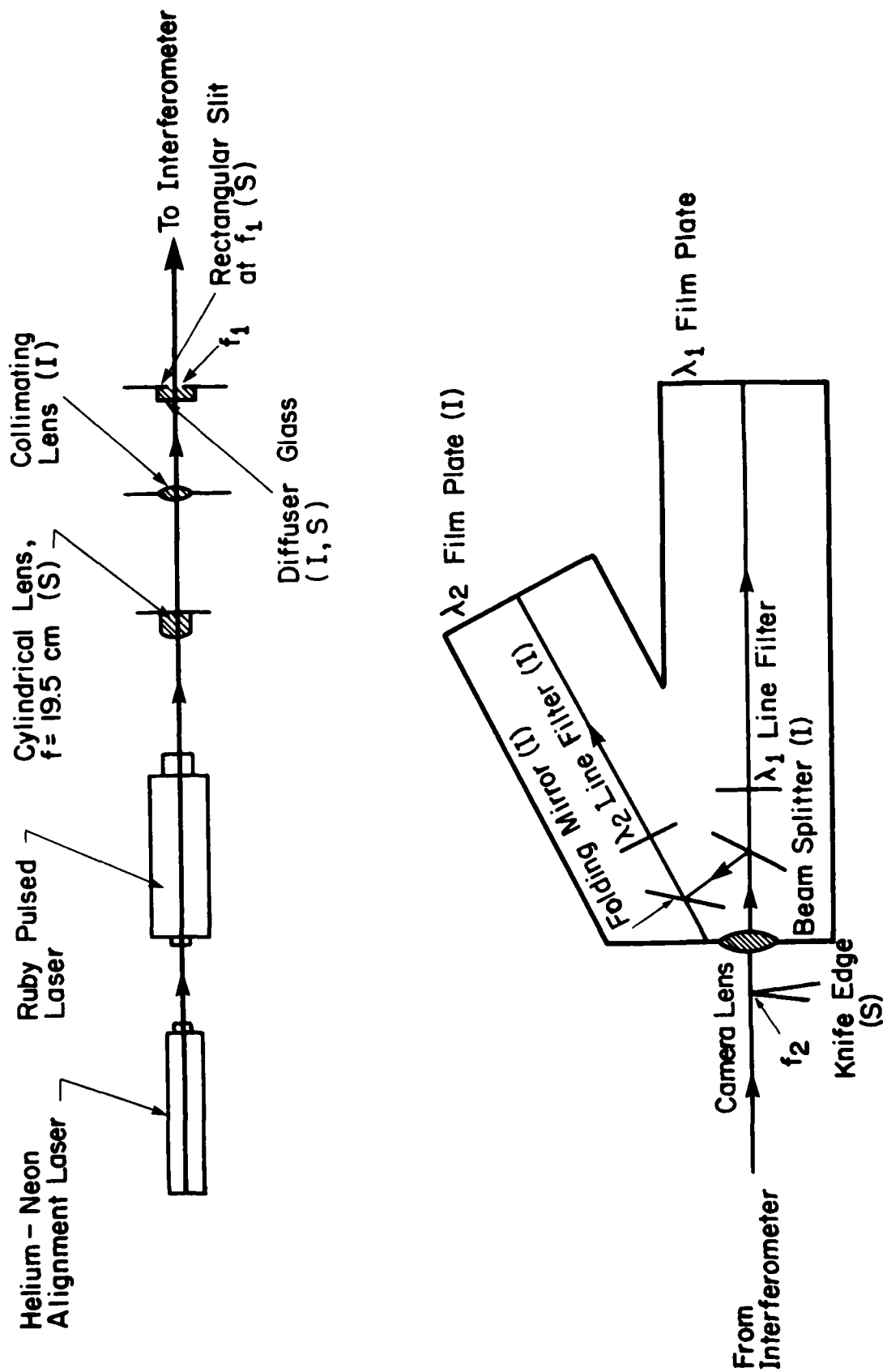
FIG. 13 SCHEMATIC OF PERIPHERAL OPTICS.

(I): USED IN OBTAINING INTERFEROGRAMS ONLY.
(S): USED IN OBTAINING SCHLIEREN PICTURES ONLY.

FIG.
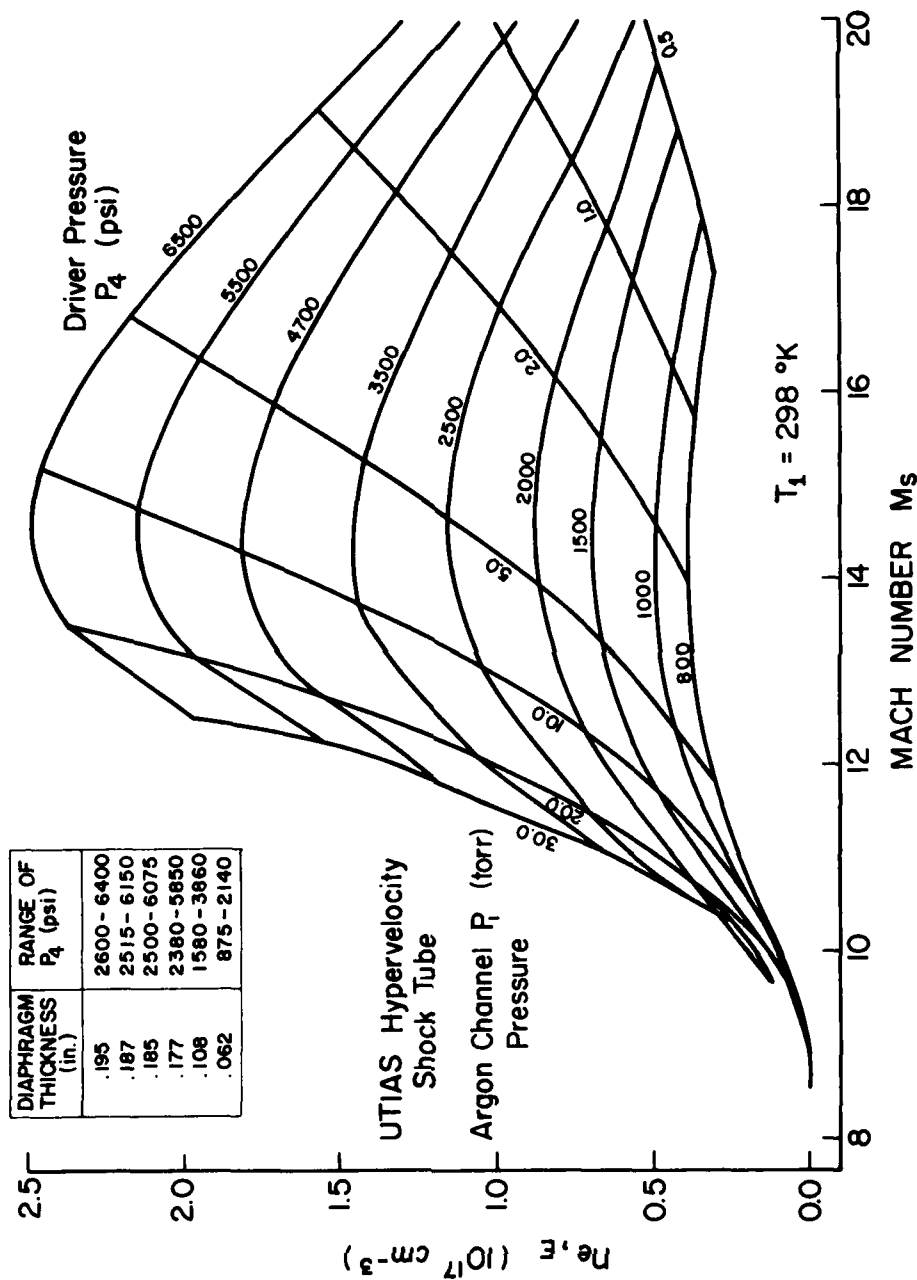
FIG. 14. VALUES OF $n_{e,E}$ vs M_s ATTAINABLE IN THE UTIAS SHOCK TUBE FOR ARGON AT T_1 = 298°K.
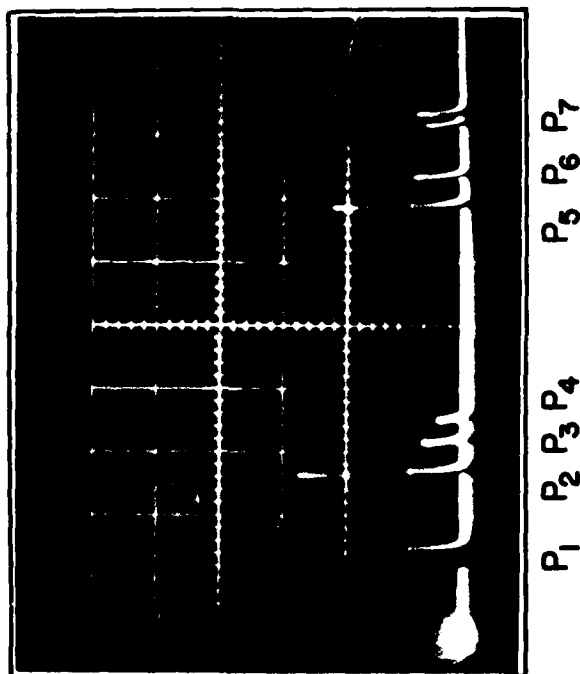
FIG. 15 OUTPUT OF PHOTODIODE EXPOSED TO LASER LIGHT WHEN t_p = 500 μs. VERTICAL - RELATIVE INTENSITY, HORIZONTAL - TIME (5 μs/div); P_1 TO P_7 ARE OUTPUT SIGNALS.

B   A   (ii)

B   A   (i)

FIG. 14. SIMULTANEOUS MULTIPLE-EXPOSURE OF AN IONIZING SHOCK WAVE MOVING LEFT
INTO ARGON. $M_s = 14.3$, $P_1 = 10.2$ TORR, $T_1 = 298.7$ °K, $t_p = 104$ ns.
(i) 6943 A, (ii) 3471.5 A. MAIN PULSE AT EACH SHOCK FRONT IMAGE AT
A AND THE SECOND IMAGE (ABOUT 7 μs LATER) NEAR B. COMPARE THE
CLARITY OF THE FRINGES OF (i) WITH THOSE IN FIGS. 3 AND 5.

Flash - Lamp Pumping Time (tp) (μs)
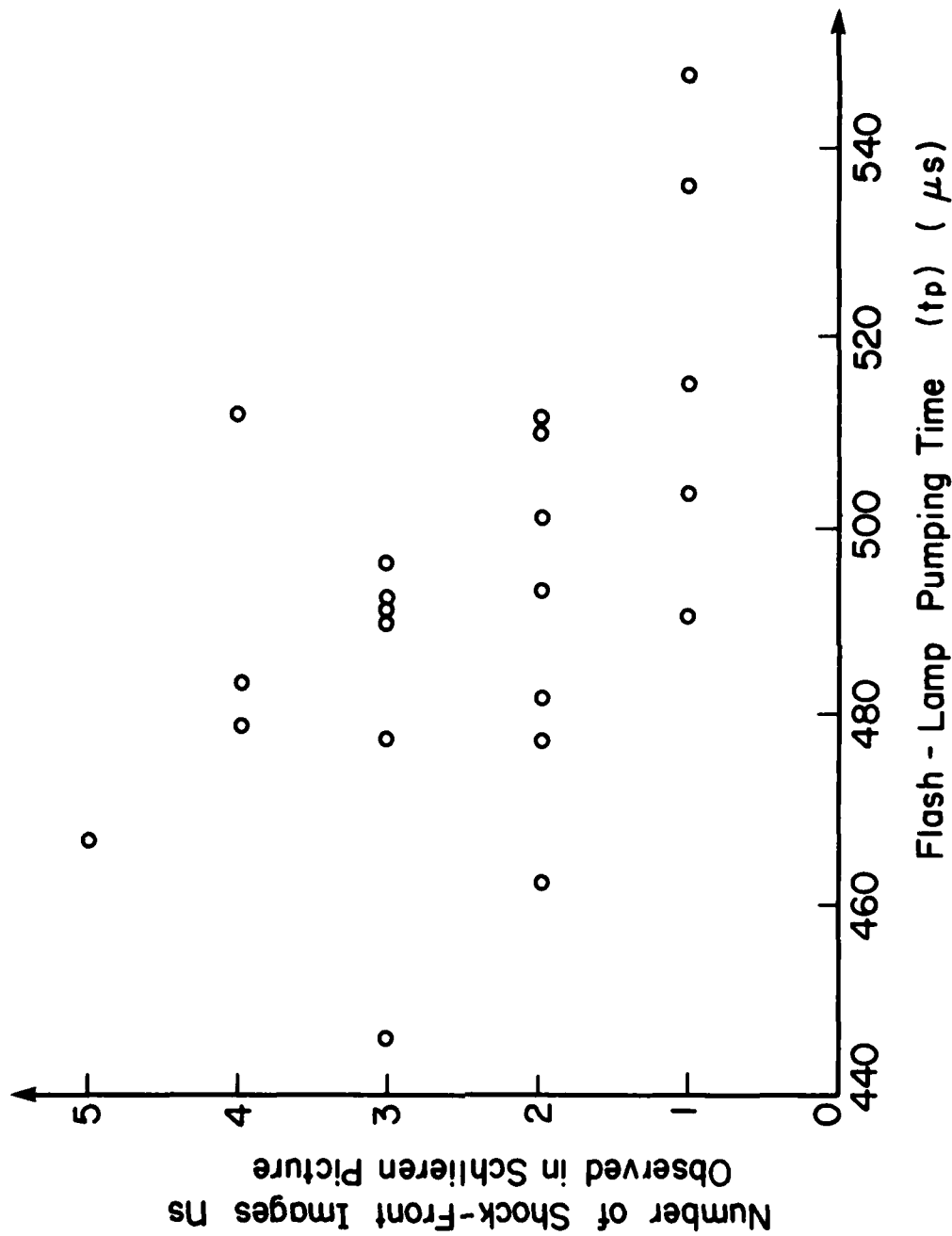
FIG. 17 NUMBER OF SHOCK-FRONT IMAGES n_s, OBSERVED IN EACH MULTIPLE-EXPOSURE
SCHLIEREN PICTURE WITH LASER FLASH-LAMP PUMPING TIME t_p. THIS
ILLUSTRATES THE REGION OF t_p IN WHICH THE RUBY LASER WAS USED
SUCCESSFULLY AS A HIGH-SPEED MULTIPULSE LIGHT SOURCE. FUTURE
EXPERIMENTS SHOULD DESIGN FOR $t_p = 485$ μs (P_1 BACKGROUND WAS TOO
BRIGHT TO SEE ANY IMAGES OTHER THAN I_1).
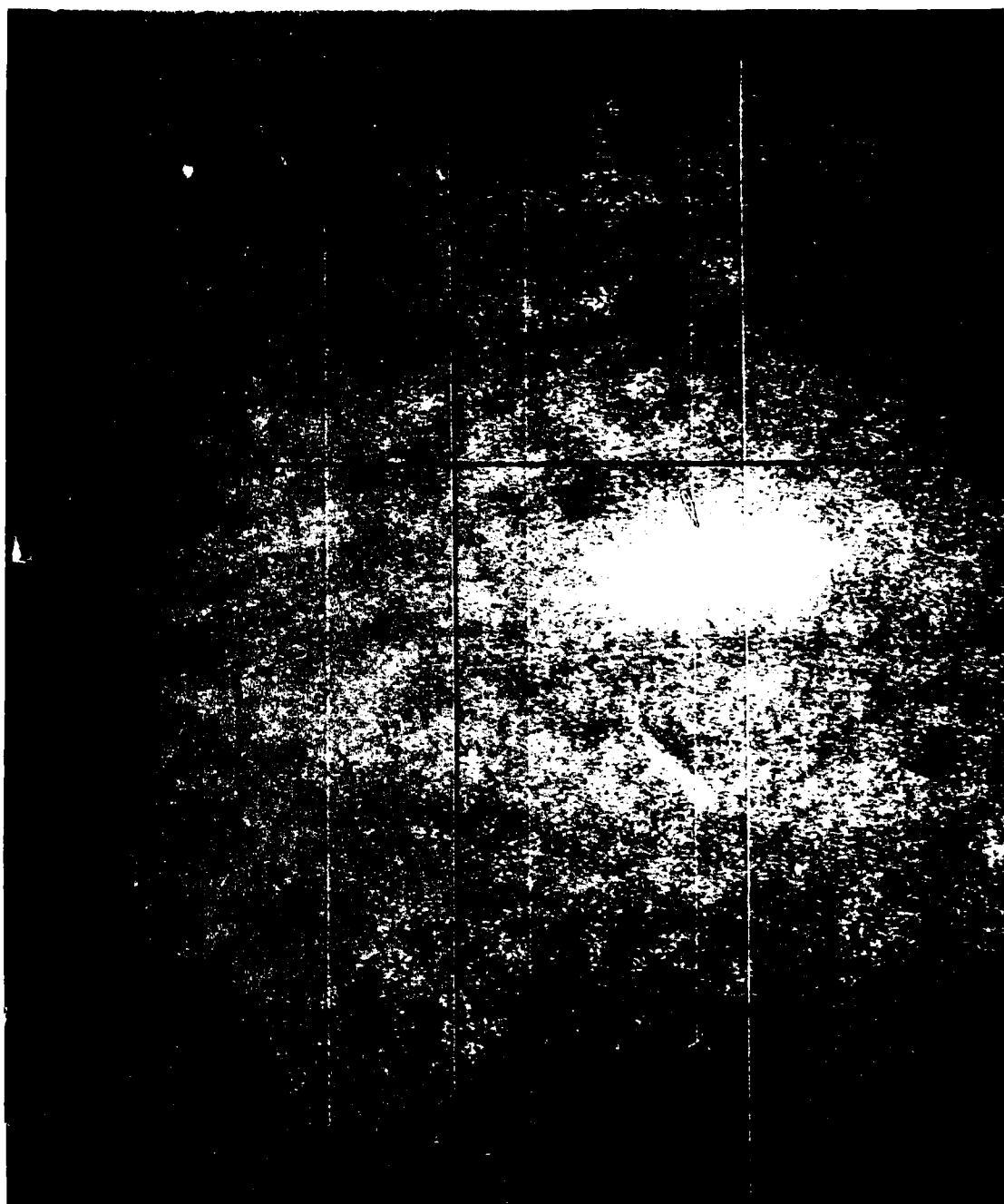
W_H

I_4 $\quad$ W_V I_3 $\quad$ I_2 I_1

W_H

I_4 W_V I_3 I_2 I_1

W_H

W_V
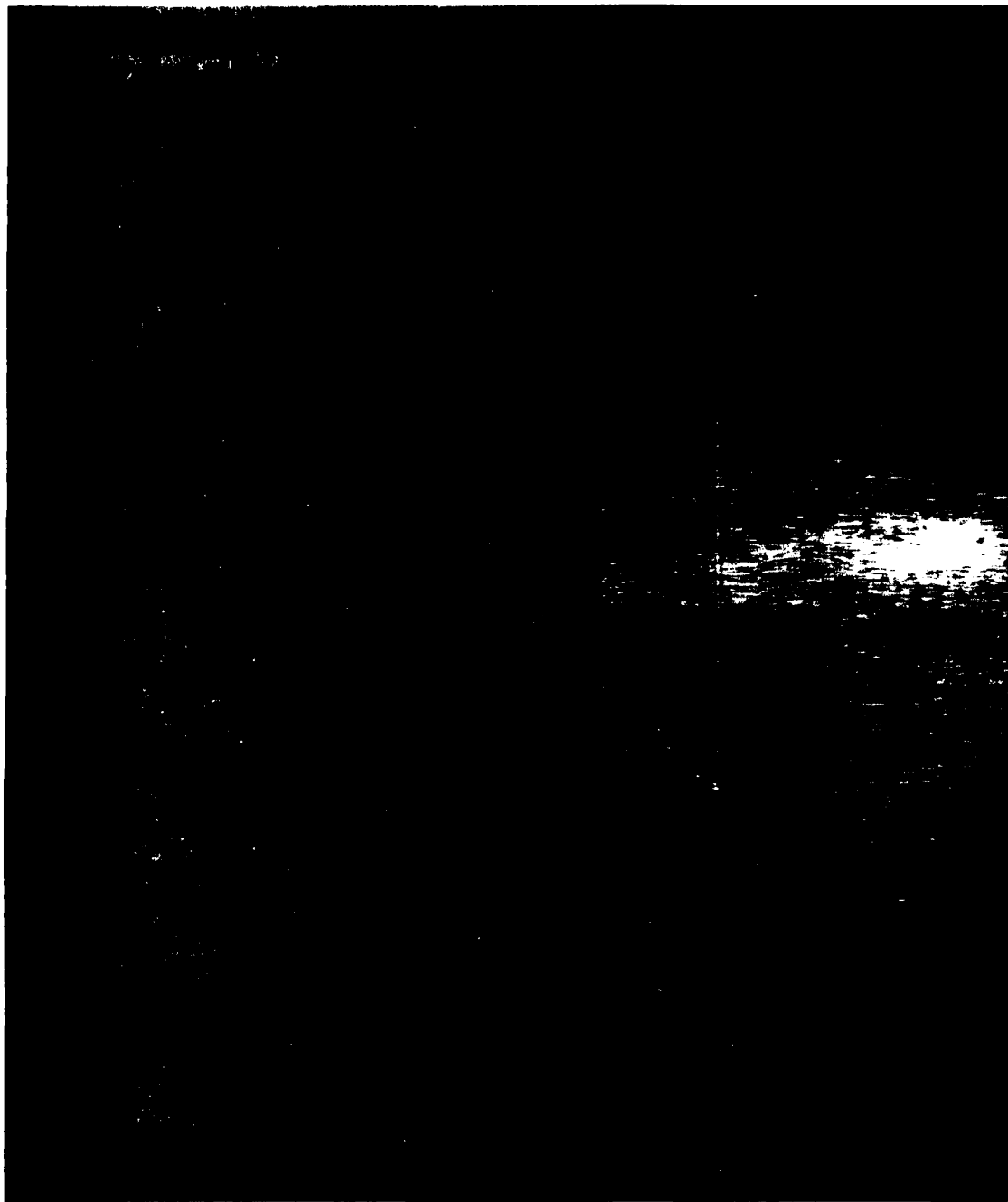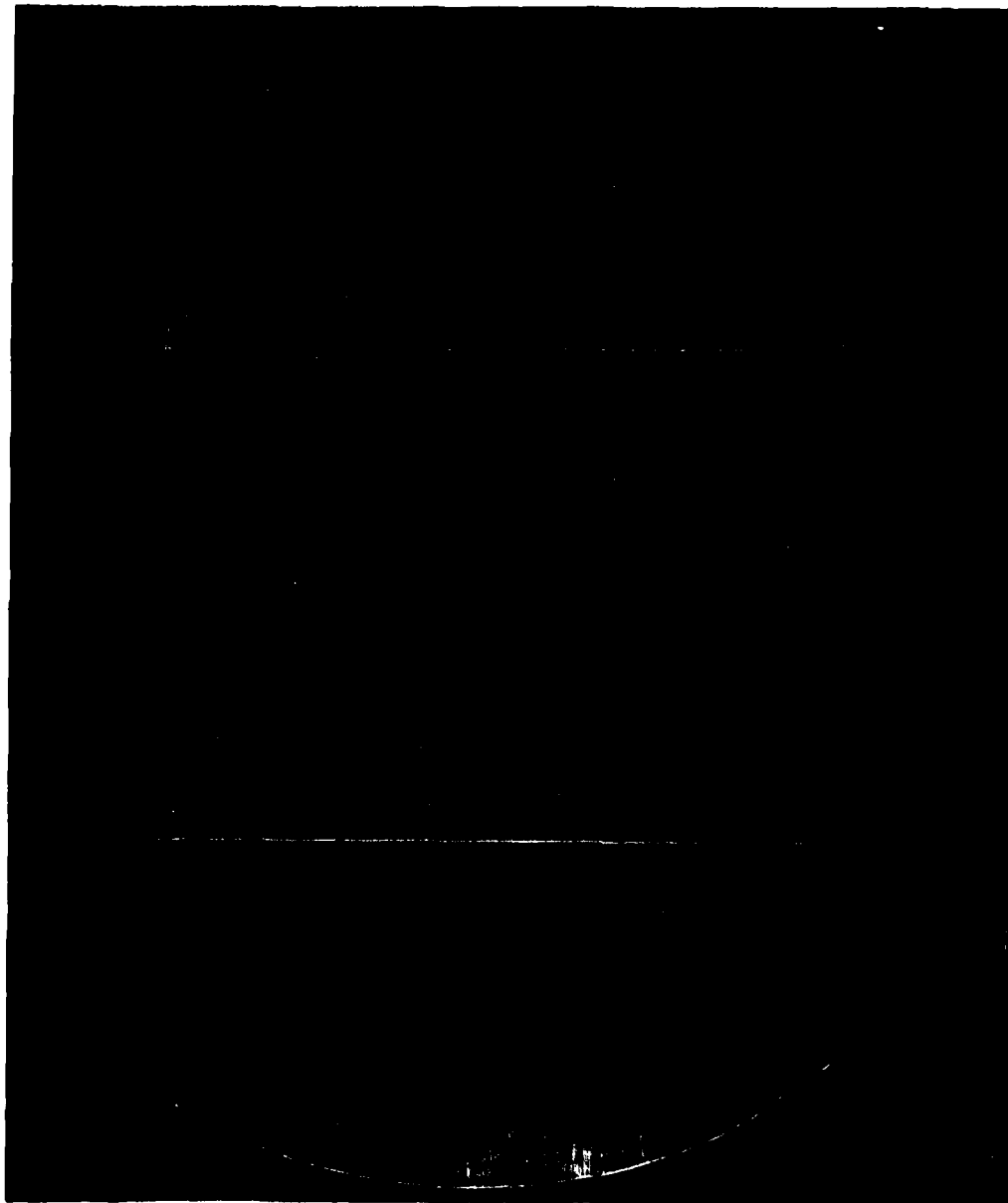
I_4 I_3 I_2 I_1

FIG. 20(a) MULTIPLE-EXPOSURE SCHLIEREN PICTURE OF AN IONIZING SHOCK WAVE MOV: LEFT INTO ARGON. M_s = 11.5, P_1 = 9.98 TORR, T_1 = 299.2°K, t_p = 4: μs (RUN NO. 2). TWO USABLE SHOCK IMAGES APPEAR AT I_1 AND I_2; TWO FAINT ONES AT I_3 AND I_4. ONLY THE TRANSLATIONAL FRONT IS IMAGED HERE, APPEARING AS A CURVED VERTICAL LINE.
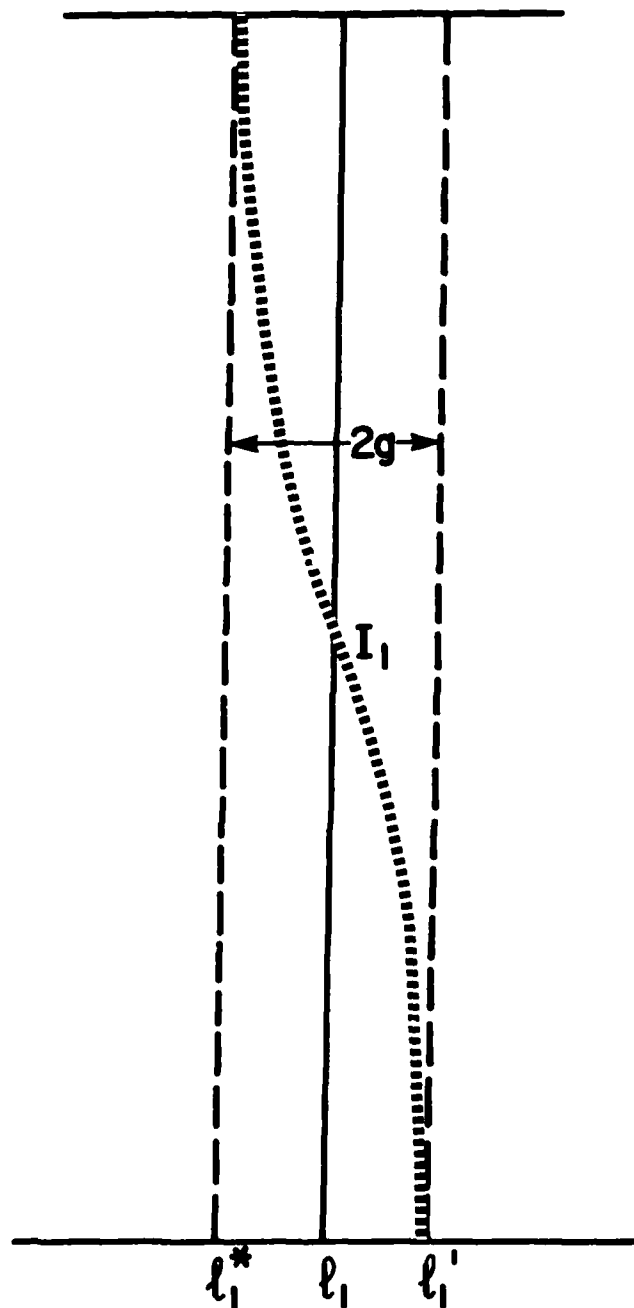
FIG. 20(b)   SCHEMATIC DRAWING OF THE CURVED SHOCK IMAGE I_1 AT LEFT, SHOWING
THE LINES ℓ_1^* AND ℓ_1' WHICH ARE PARALLEL TO w_V (THE Y-DIRECTION),
THE SHOCK POSITION ℓ_1 MIDWAY BETWEEN THEM, AND THE AMPLITUDE g
OF THE DISTURBED SHOCK FRONT, EXAGGERATED HERE FOR THE PURPOSE
OF ILLUSTRATION. IN (a) 2g = 3.7 mm. I_1 CONSISTS OF THE BASIC
GEOMETRIC UNIT, THE COSINE HALF-WAVE, WHICH IS PERPENDICULAR TO
THE TOP AND BOTTOM WALLS. NOTE THAT I_1 CROSSES ℓ_1 JUST ONCE.
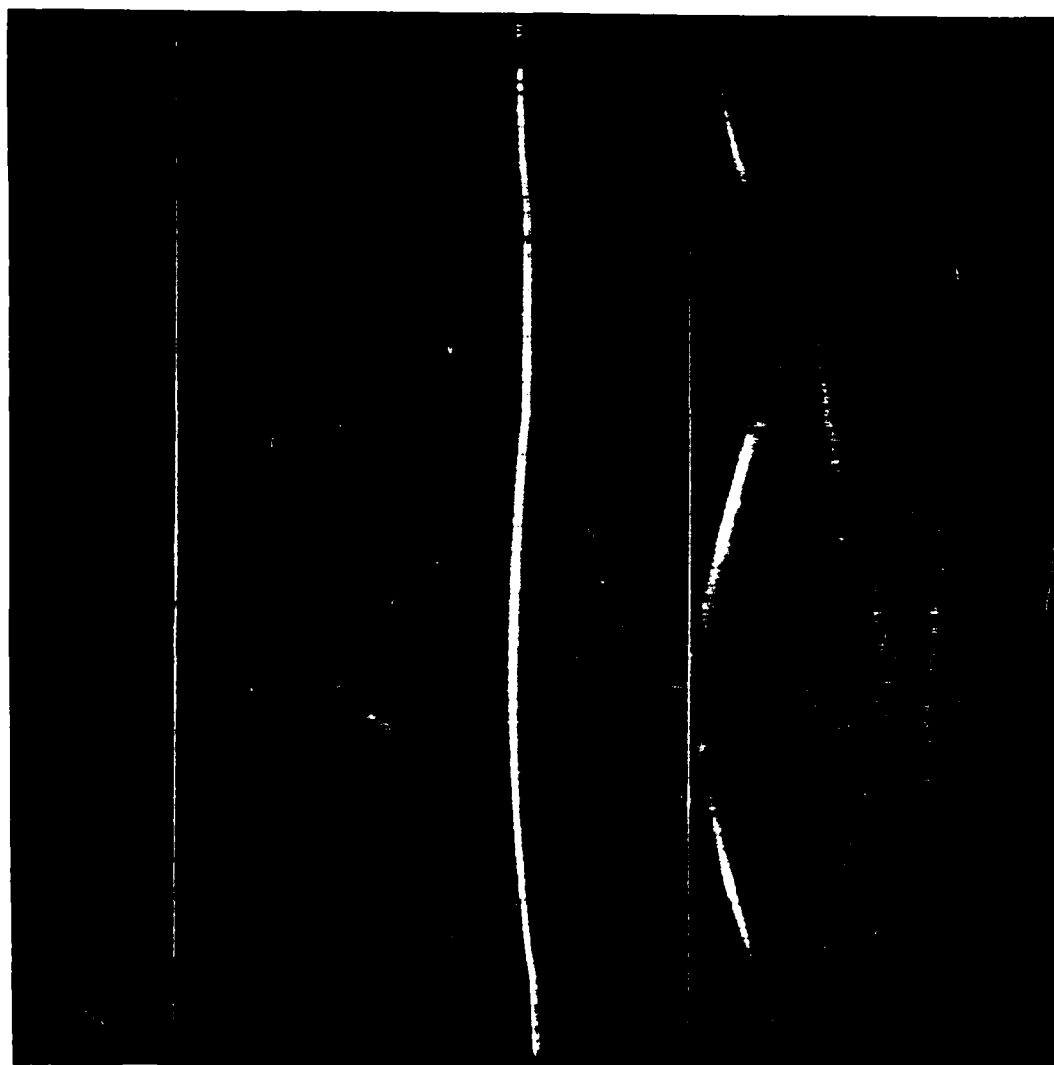
W_H

W_H

W_V I_2 I_1 W_V D_1

FIG. 1(a) IS THIS-EXPOSURE SCHLIEREN PICTURE OF AN IGNITING SHOCK WAVE IN I₂. SHOCK IN ARGON. M_s = 1..., I_1 = ..11 TORR, T_1 = 297.0°K, t_2 = 0 µs (RUN 19, 20). ONLY ONE SHOCK IMAGE IS VISIBLE AT I_1. THE SECOND SHOCK IMAGE SHOULD APPEAR "I_2"

W_V I_2 I_1 W_V D_1
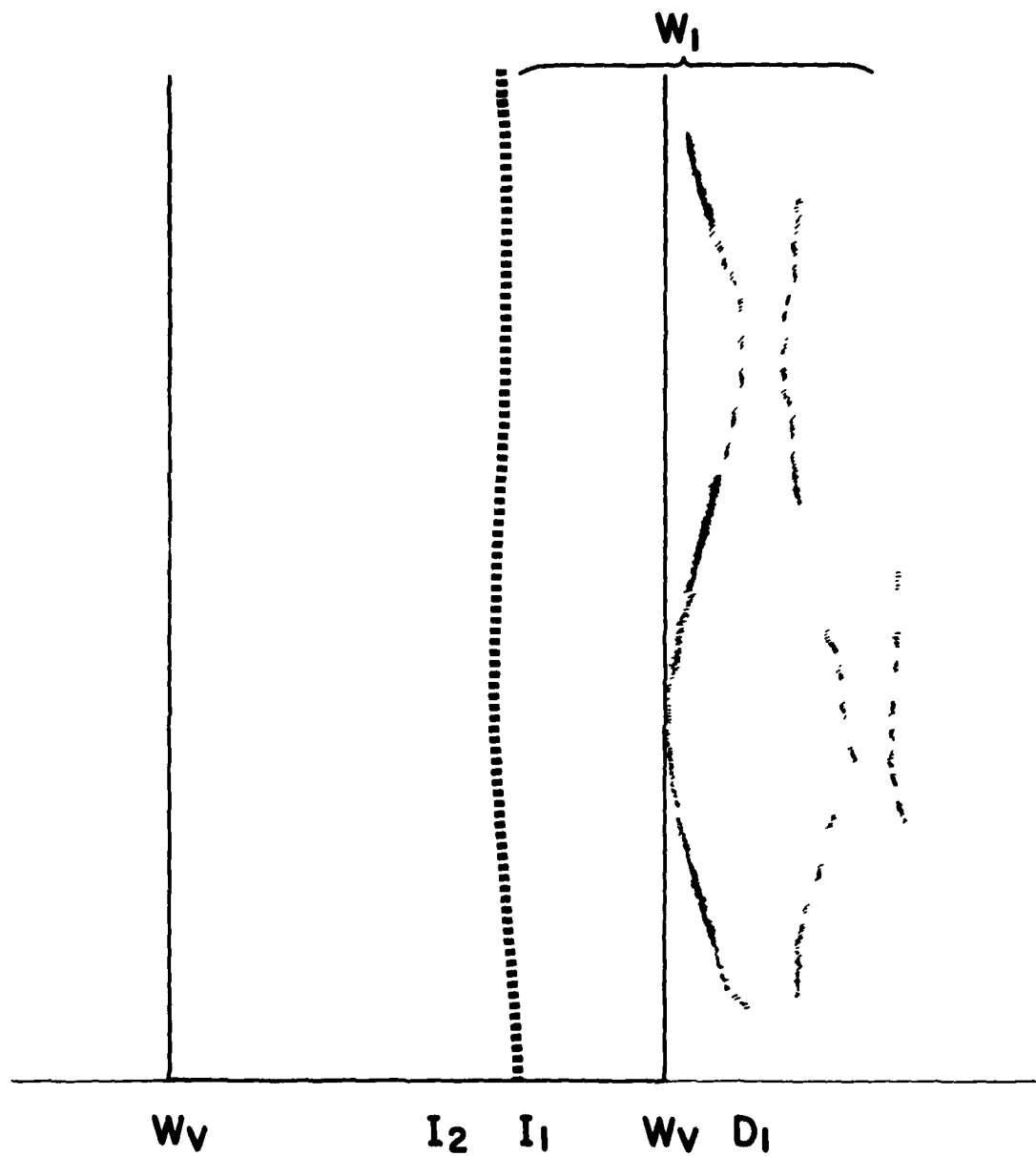
FIG. 21(b) W_1 - WAVE SYSTEM BEHIND THE CURVED SHOCK FRONT, D_1 - DARK BAND DUE TO LARGE dn_e/dx AT ELECTRON CASCADE FRONT. NOTE THAT THIS BAND VARIES REGULARLY IN DISTANCE FROM I_1 ACCORDING TO THE LATTER'S SHAPE.
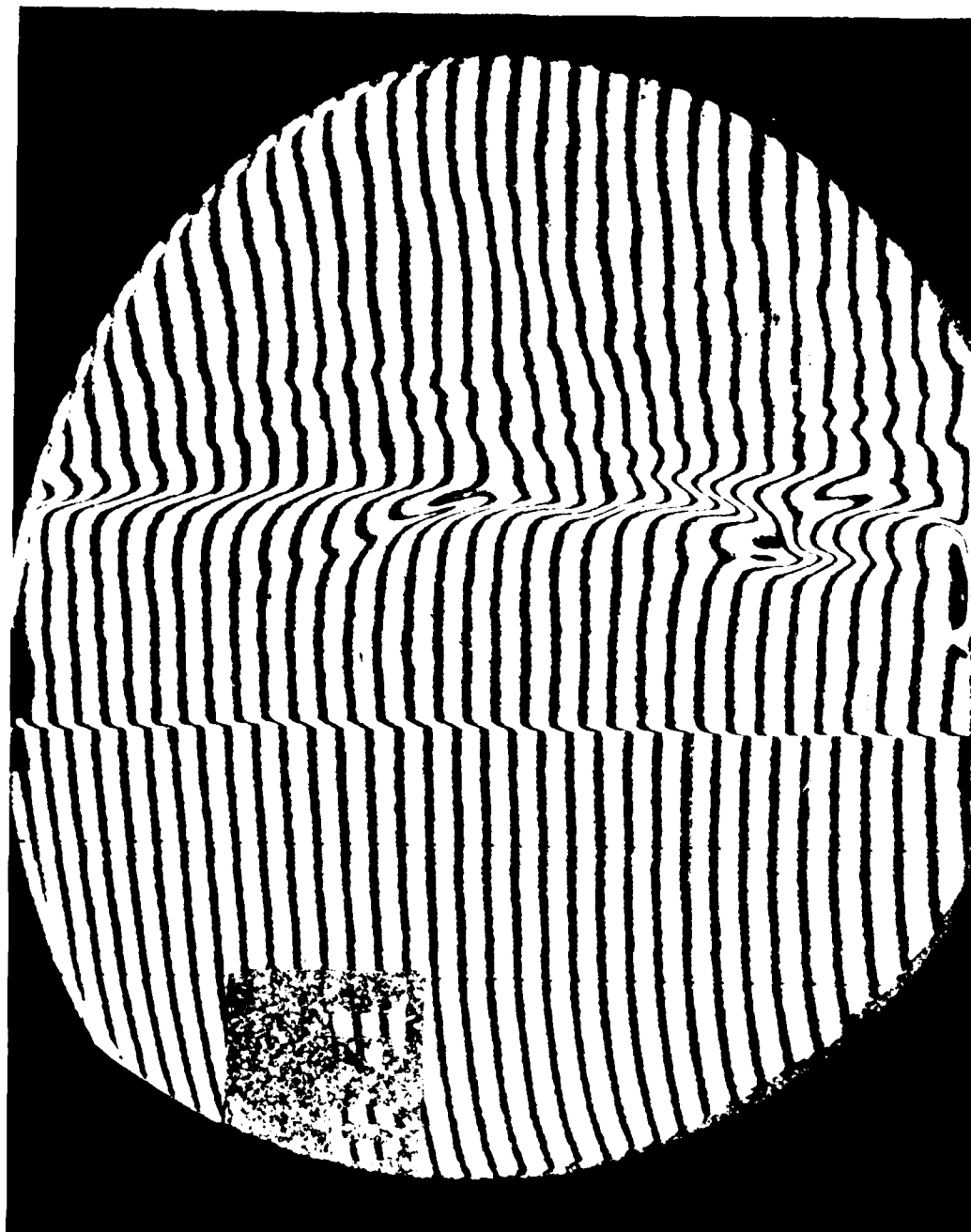
FIG. 22 SINGLE-EXPOSURE INTERFEROGRAM OF AN IONIZING SHOCK WAVE MOVING
LEFT INTO ARGON. M_s = 14.77, P_1 = 3.95 TORR, T_1 = 297.6°K
(RUN NO. P1 IN TABLE 1). AN INCREASE IN REFRACTIVE INDEX MOVES
THE FRINGES UPWARDS.
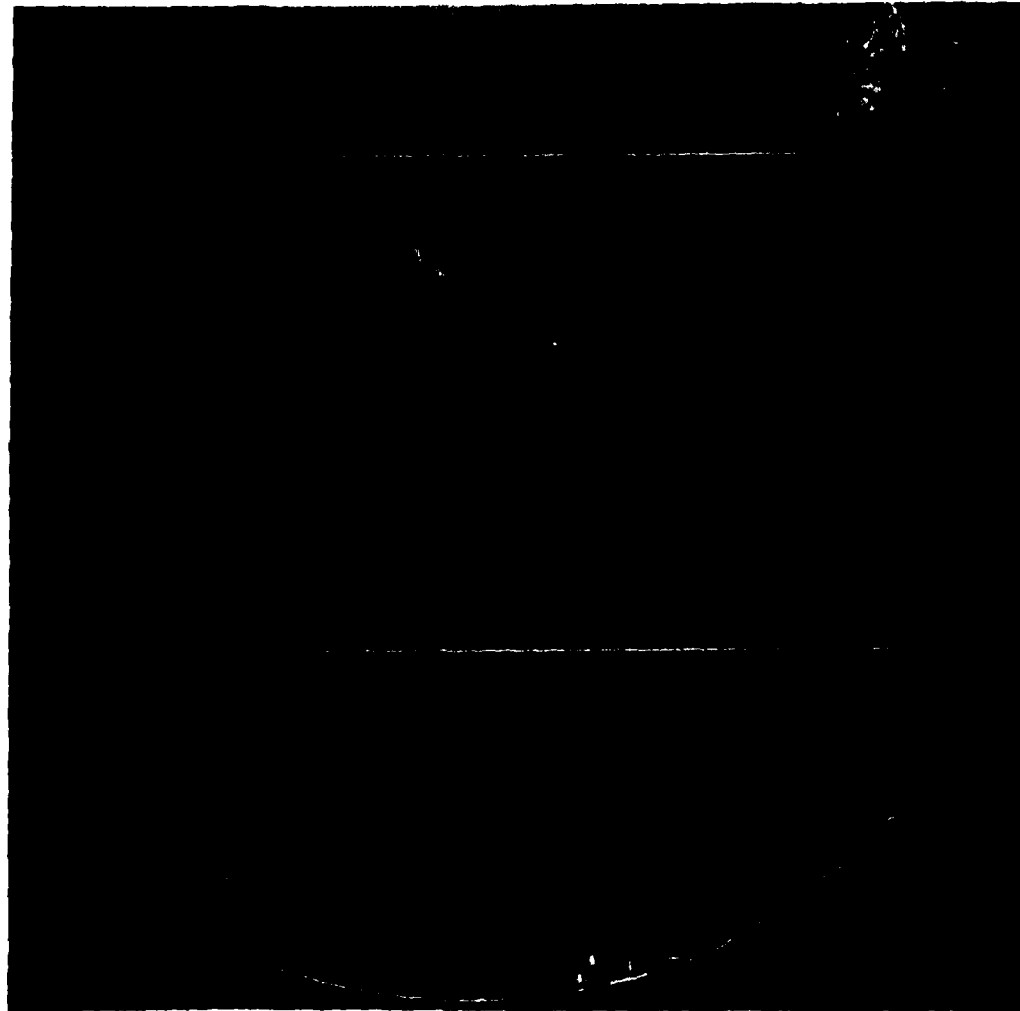
FIG. 23(a) MULTIPLE-EXPOSURE SCHLIEREN PICTURE OF AN IONIZING SHOCK WAVE MOVING LEFT IN ARGON. $M_S = 14.5$, $P_1 = 3.18$ TORR, $T_1 = 299.0°K$ (RUN NO. 7).
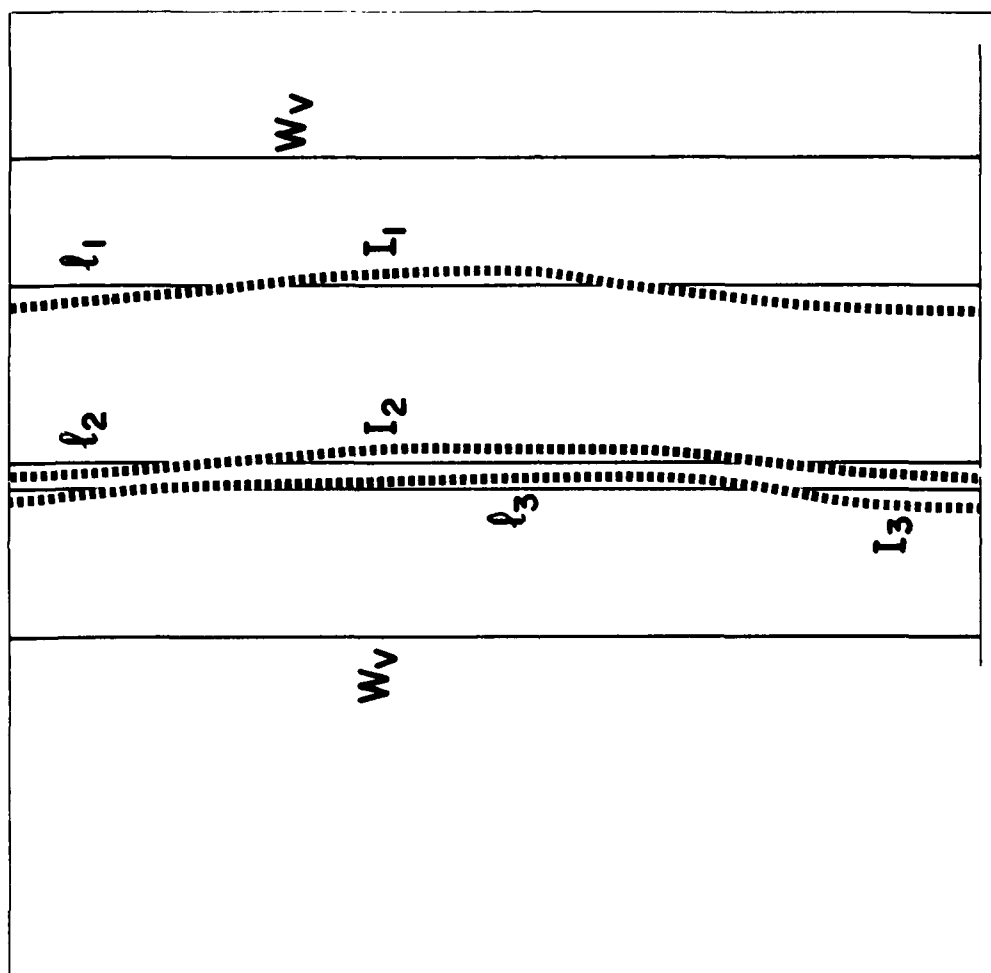
FIG. 23(b) SCHEMATIC DRAWING OF THE IMPORTANT FEATURES OF 23(a).
I_1 TO I_3 - SCHLIEREN IMAGES OF THE TRANSLATIONAL SHOCK
FRONT. ℓ_1 TO ℓ_3 - SHOCK POSITIONS. w_v - VERTICAL
REFERENCE WIRES. NOTE THAT ℓ_1 CROSSES I_1, n_h = 2 TIMES.
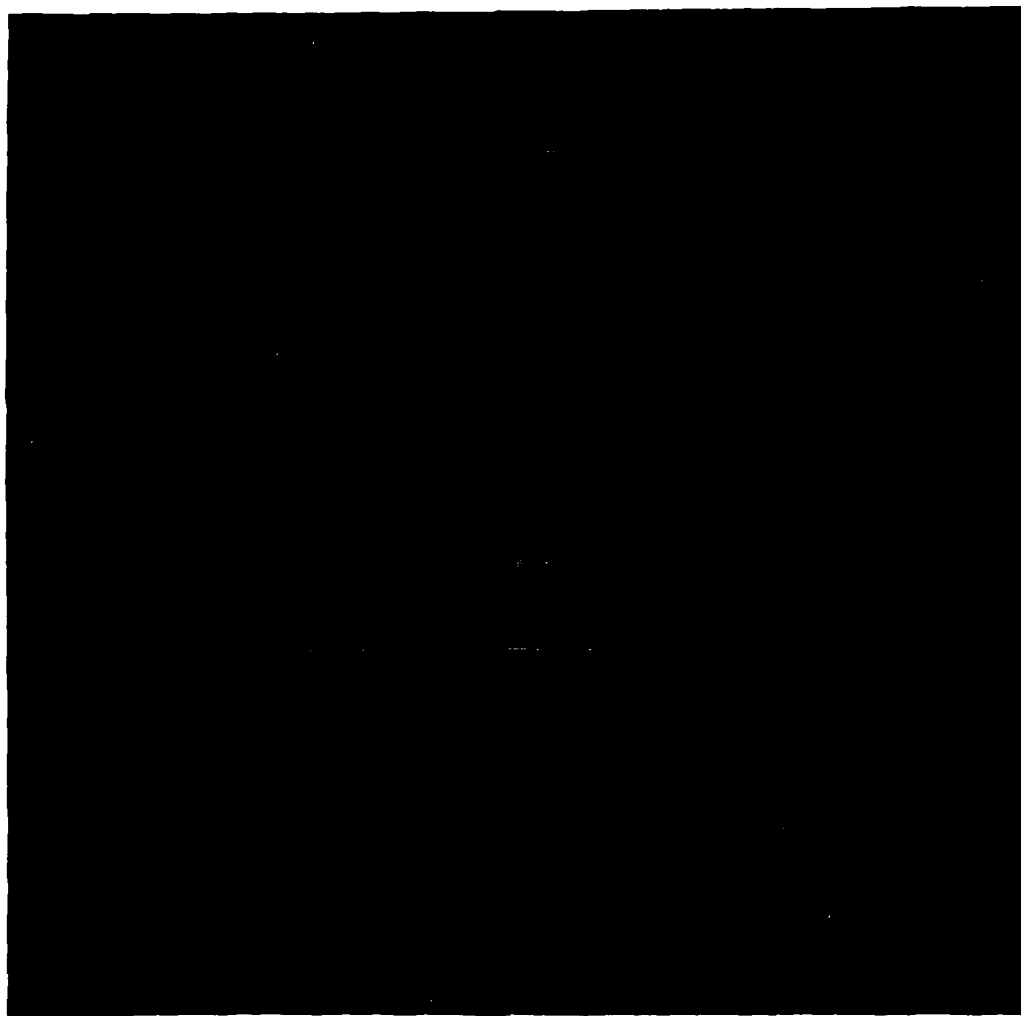
FIG. 24(a) MULTIPLE-EXPOSURE SCHLIEREN PICTURE OF AN IONIZING SHOCK WAVE MOVING LEFT IN ARGON. M_s = 12.3, p_1 = 17.04 TORR, T_1 = 292.5 K, t_p = __ μs (RUN NO. 13).
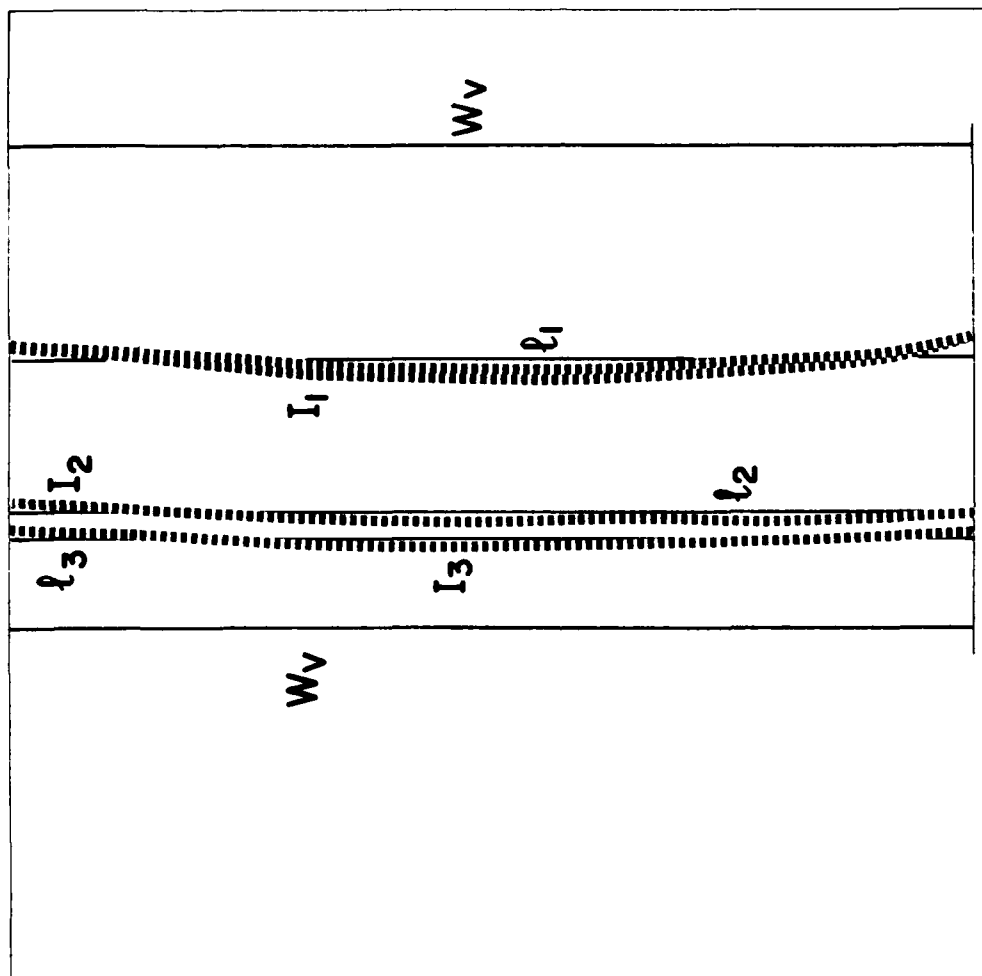
FIG. 24(b) SCHEMATIC DRAWING OF THE IMPORTANT FEATURES OF 24(a).
I_1 TO I_3 - SCHLIEREN IMAGE OF THE TRANSLATIONAL SHOCK
FRONT, ℓ_1 TO ℓ_3 - MEAN SHOCK POSITIONS, w_v - VERTICAL
REFERENCE WIRES. ALL THREE SHOCK IMAGES, ESPECIALLY
I_1, EXHIBIT THREE-DIMENSIONAL EFFECTS.
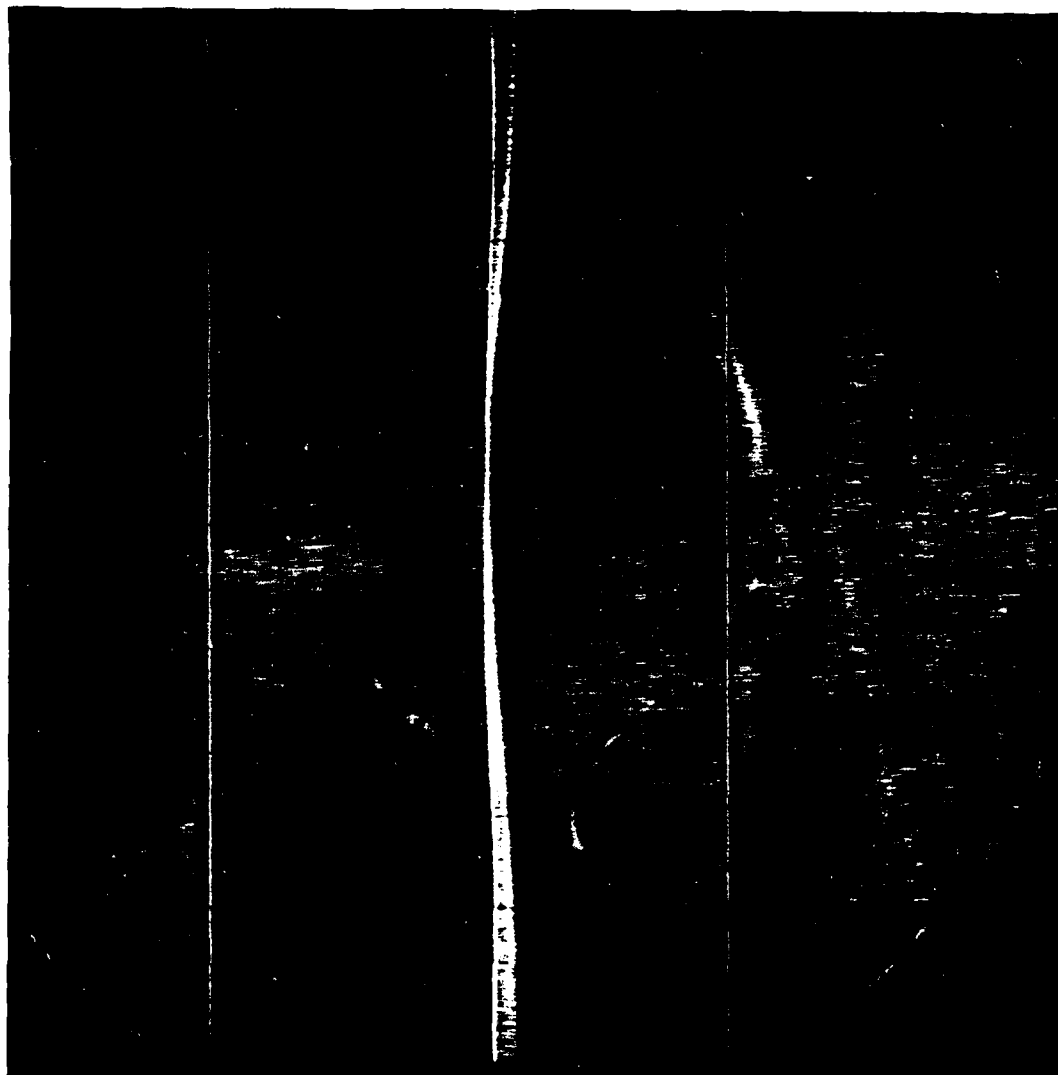
FIG. 28(a) MULTIPLE-EXPOSURE SCHLIEREN PICTURE OF AN IONIZING SHOCK WAVE MOVING LEFT IN ARGON. $M_S = 12.7$, $p_1 = 11.50$, $T_1 = 298.1°K$. $t_p = 11$ ms (RUN NO. 10).
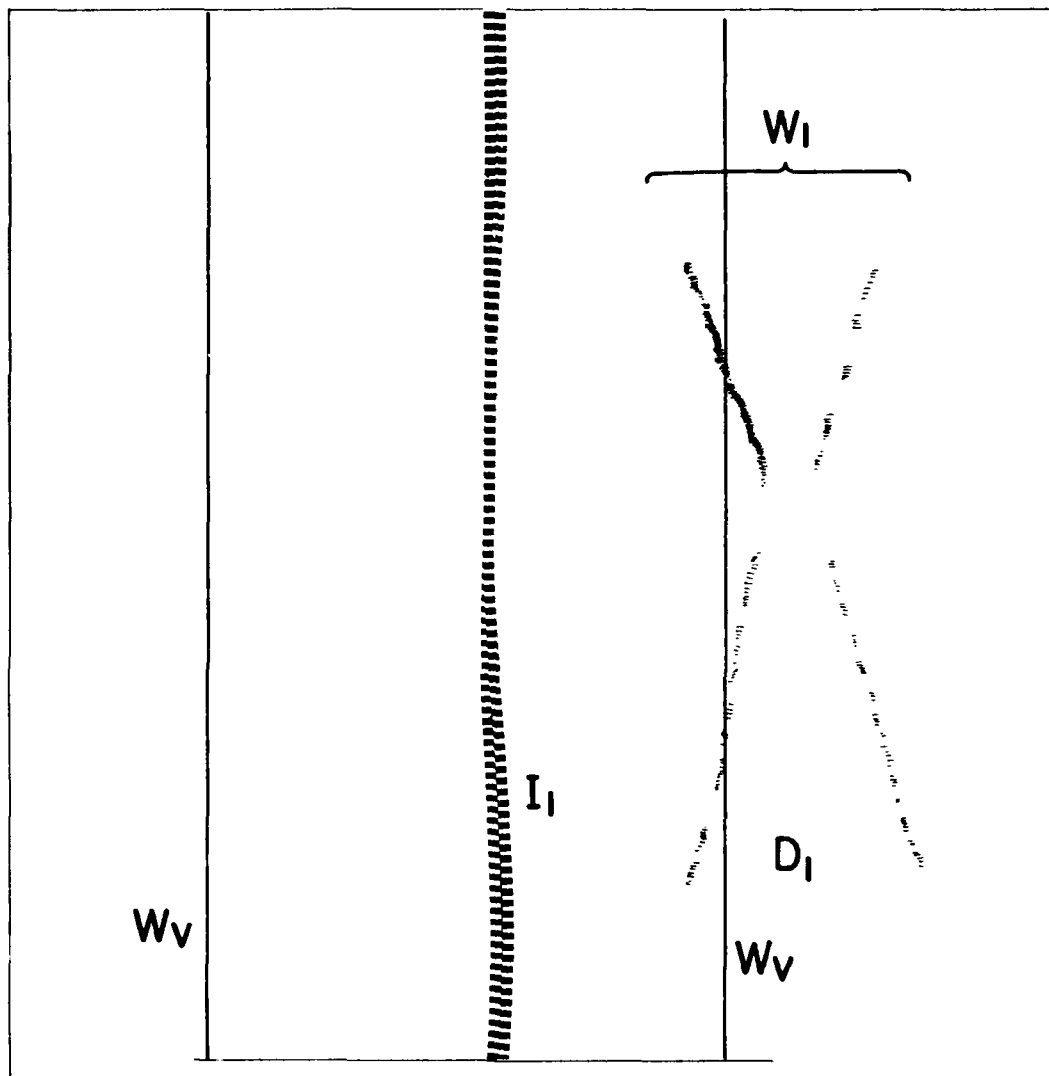
FIG. 25(b) SCHEMATIC DRAWING OF THE IMPORTANT FEATURES OF 25(a).
I_1 - SCHLIEREN IMAGE OF THE TRANSLATIONAL SHOCK FRONT.
W_1 - SYSTEM OF TRANSVERSE WAVES BEHIND I_1. D_1 - ELECTRON
CASCADE FRONT.
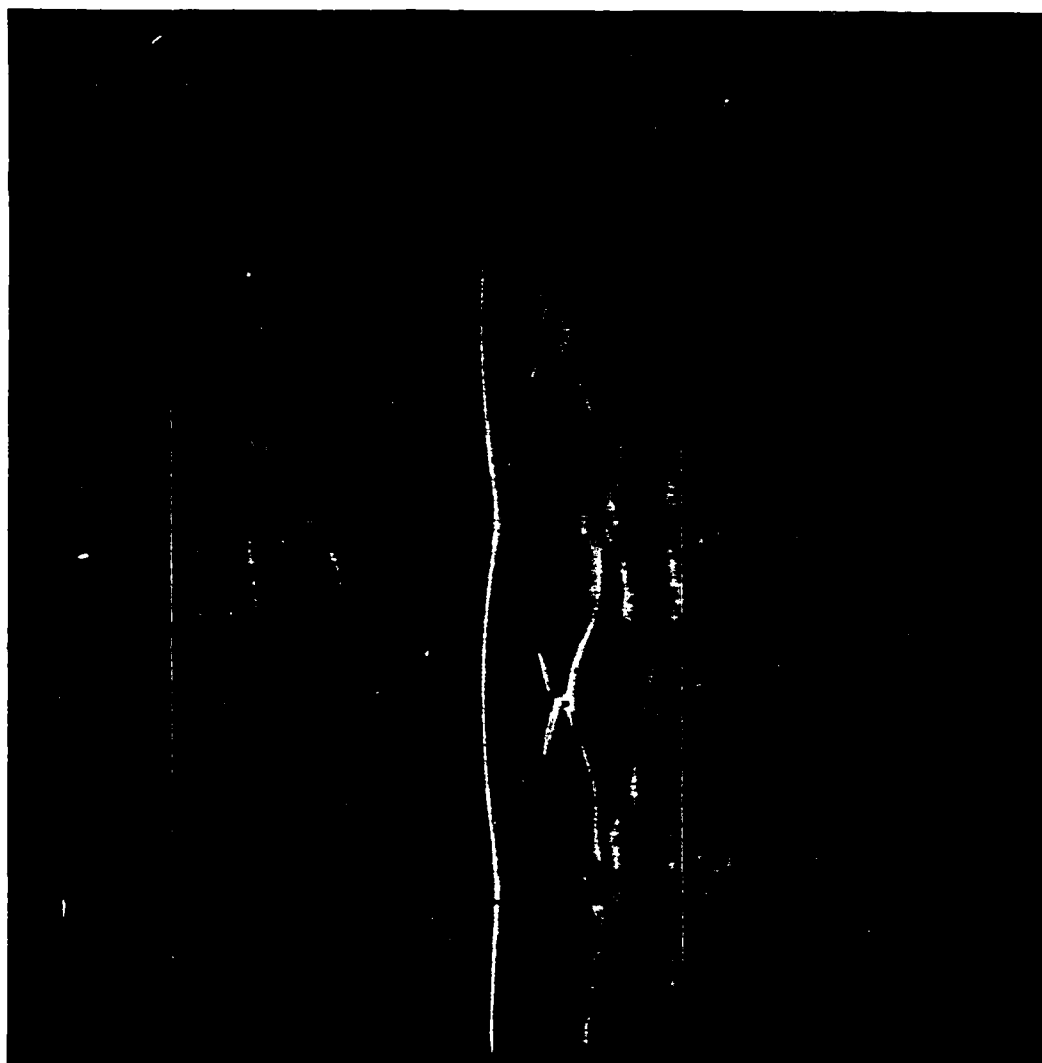
FIG. 39(a) MULTIPLE-EXPOSURE SCHLIEREN PICTURE OF AN IONIZING SHOCK WAVE MOVING LEFT IN ARGON. $M_s = 16.1$, $P_1 = 5.70$ TORR, $T_1 = 2091.5$ K, $t_p = $ (REF. 39, XX).
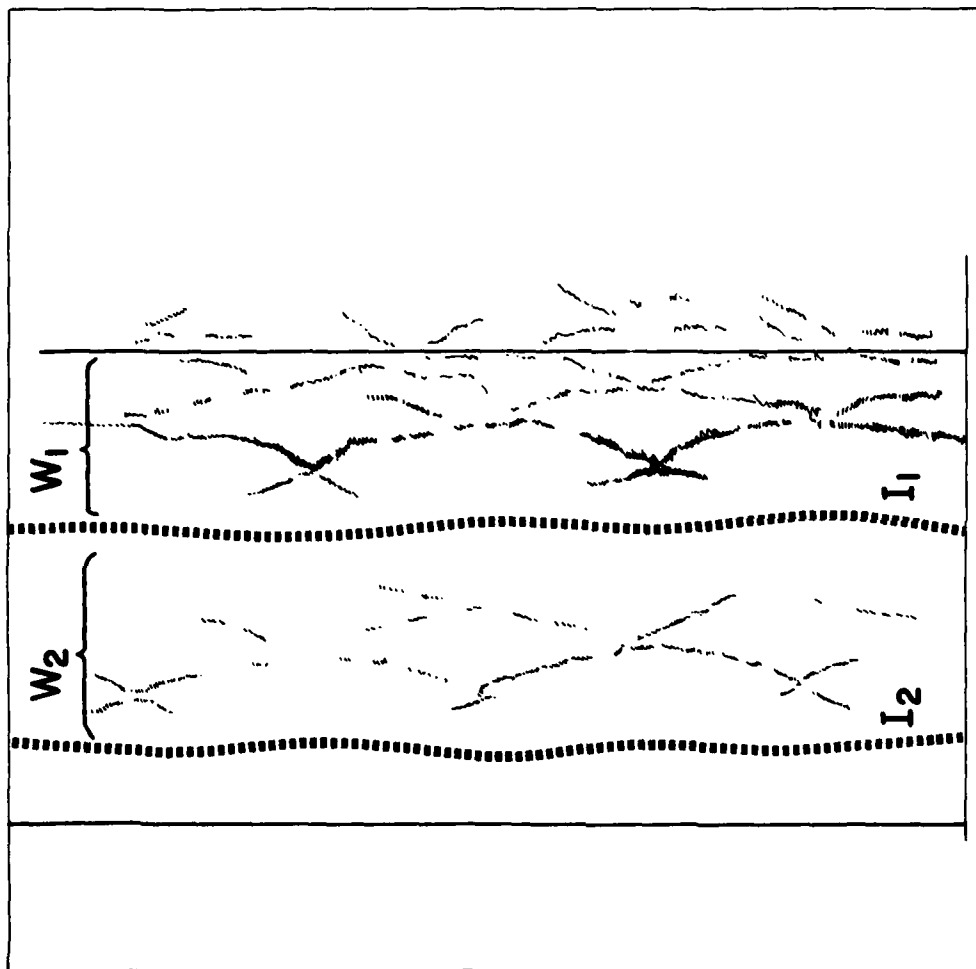
FIG. 26(b) SCHEMATIC DRAWING OF THE IMPORTANT FEATURES OF 26(a).
I_1, I_2 - SCHLIEREN IMAGES OF THE TRANSLATIONAL SHOCK
FRONT, $W_{1,2}$ - SYSTEM OF TRANSVERSE WAVES BEHIND $I_{1,2}$.
$D_{1,2}$ - ELECTRON CASCADE FRONTS. A DEFINITE CHANGE IN
THE SHOCK FRONT GEOMETRY AS WELL AS THE SUBSEQUENT WAVE
SYSTEM HAS OCCURRED BETWEEN THE TWO EXPOSURES I_1 AND I_2.
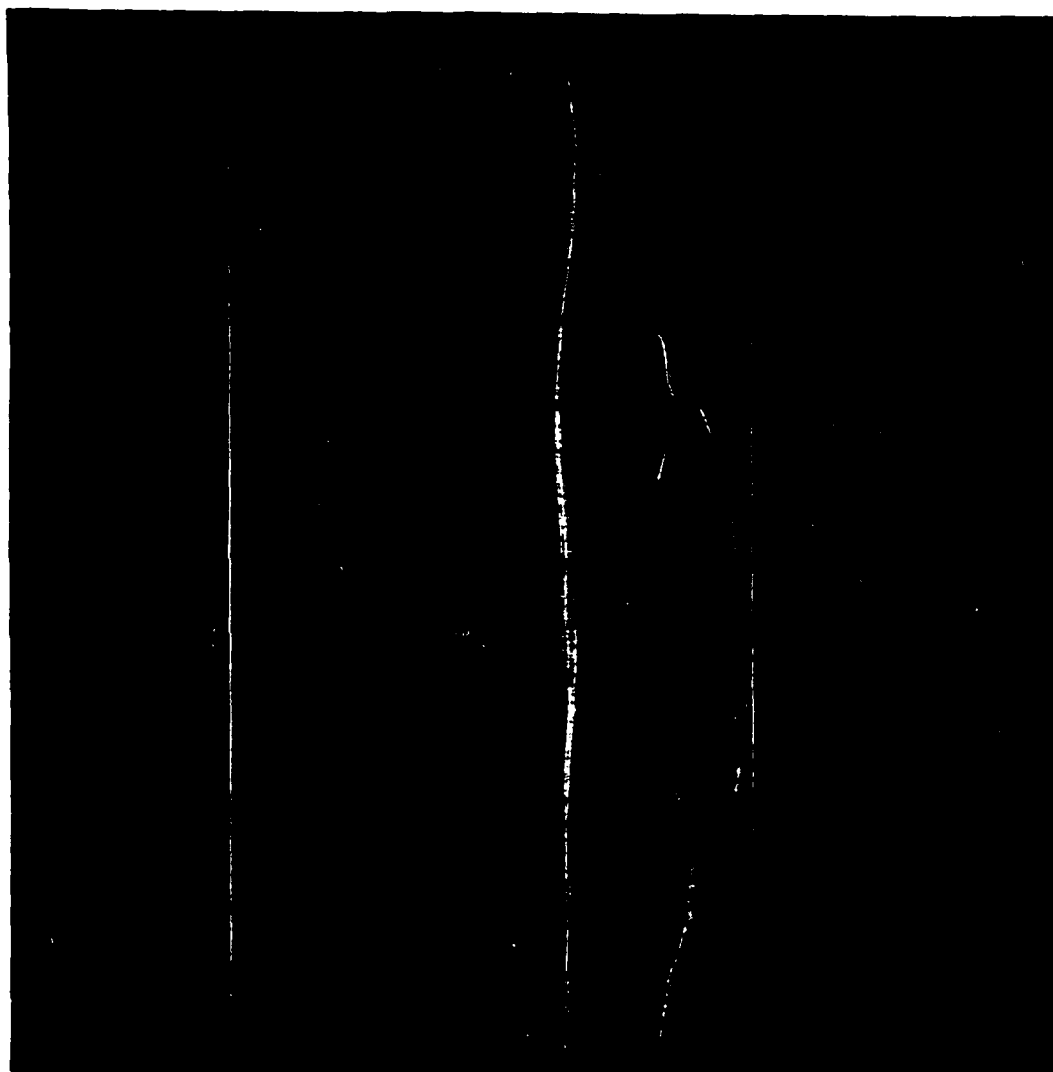
FIG. 27(a) MULTIPLE-EXPOSURE SCHLIEREN PICTURE OF AN IONIZING SHOCK WAVE WITH BODY IN SHOCK. $M_s = 14.5$, $p_1 = 11.35$ TORR, $T_1 = 300.1°K$, $t_1 = 0.7$ μs (SEE REF. 21).
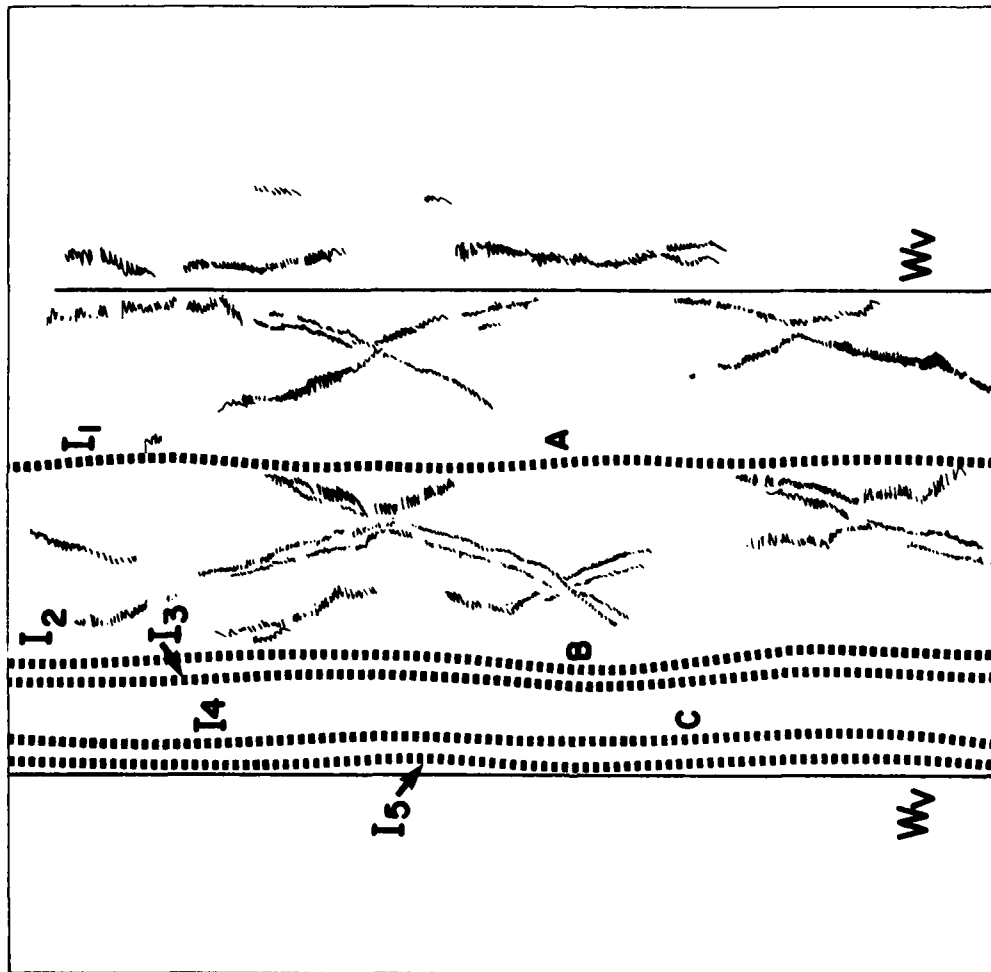
FIG. 27(b) SCHEMATIC DRAWING OF THE IMPORTANT FEATURES OF 27(a).
I_1 TO I_5 - SCHLIEREN IMAGES OF THE TRANSLATIONAL SHOCK
FRONT, W_n - SYSTEM OF TRANSVERSE WAVES CORRESPONDING TO
I_n. D_1 - ELECTRON CASCADE FRONT. w_V - VERTICAL REFERENCE
WIRE. THIS PICTURE INDICATES THAT THE SHOCK NON-PLANARITY
BEHAVES LIKE A TRAVELLING WAVE.

(a)

HUGONIOT CURVE

RAYLEIGH LINE

(v_2, p_2)

(v_1, p_1)

SLOPE $\left(\dfrac{dp}{dv}\right)_H$

p

(b) LAB FRAME

$u=0$ a_1 v_1 U_s u_2 a_2 v_2

(c) SHOCK FRAME

w_1 a_1 v_1 v_2 a_2 w_2
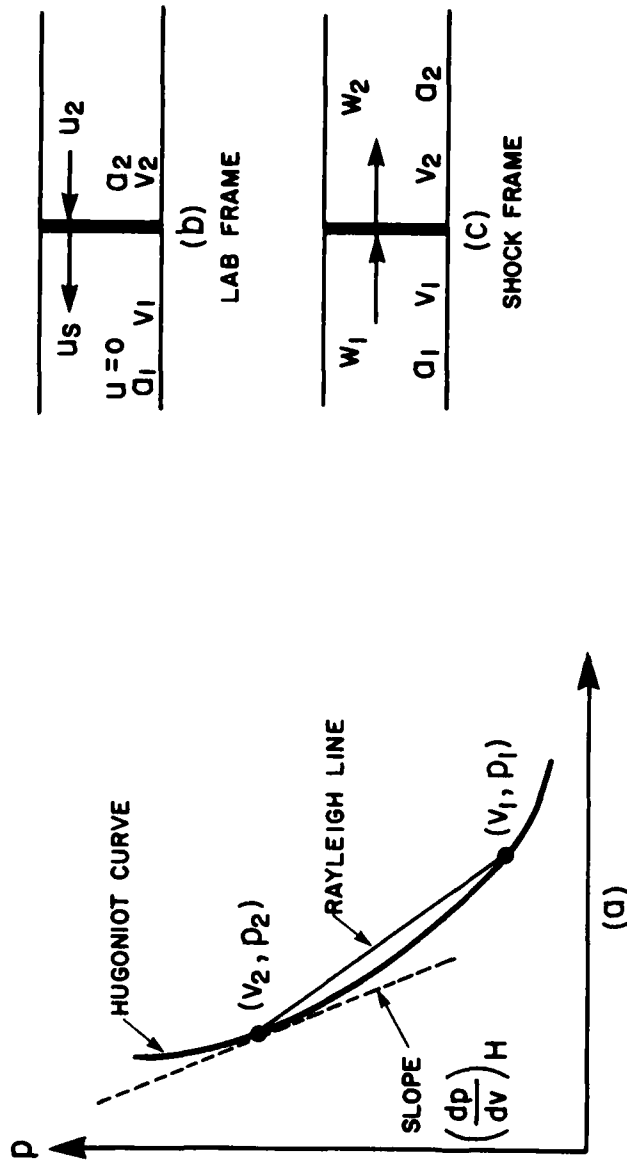
FIG. 28(a)   PRESSURE-VOLUME PLOT SHOWING INITIAL STATE (v_1, p_1), SHOCK WAVE STATE (v_2, p_2), SLOPE $(dp/dv)_H$ OF HUGONIOT CURVE AT SHOCK STATE, AND RAYLEIGH LINE JOINING THE TWO STATES. ANY TWO POINTS ON HUGONIOT CURVE REPRESENT TWO STATES SEPARATED BY SHOCK WAVE.

(b)   SHOCK WAVE WITH VELOCITY U_s IN LABORATORY REFERENCE FRAME.

(c)   SAME SHOCK WAVE IN SHOCK-FIXED REFERENCE FRAME.   THE TWO FRAMES ARE RELATED BY $w = U_s - u_2$.   THE SHOCK MACH NUMBER IS $M_s = |U_s|/a_1$. THE TEST GAS MACH NUMBER $M = w_2/a_2 = (U_s - u_2)/a_2$ IN THE SHOCK-FIXED FRAME SHOULD NOT BE CONFUSED WITH THE TEST-GAS MACH NUMBER $M_2 = |u_2|/a_2$ IN THE LABORATORY FRAME.   THE MASS FLUX IS $w_1/v_1 = w_2/v_2 = j$. FROM THE MASS AND MOMENTUM CONSERVATION EQUATIONS, WE GET $(p_2 - p_1)/(v_2 - v_1) = -j^2$.
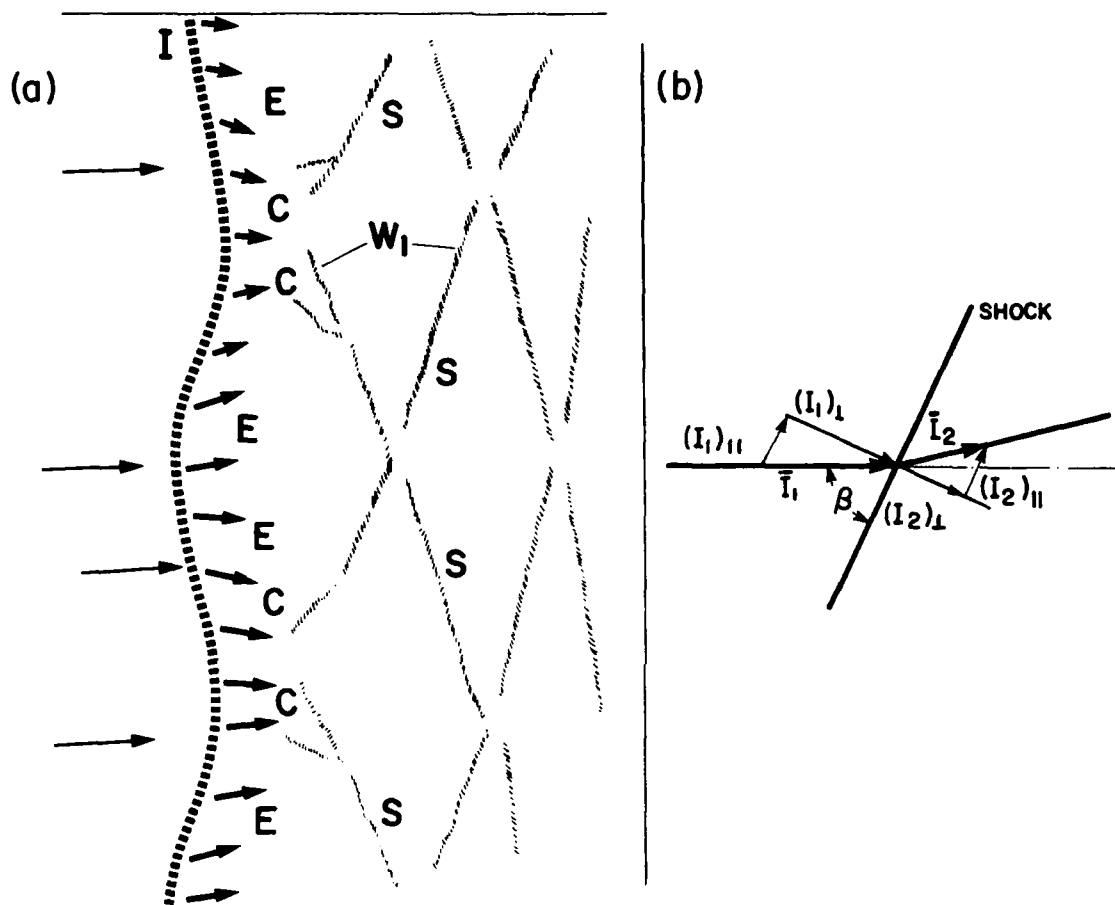
FIG. 29(a)   FLOW DEFLECTIONS BEHIND SINUSOIDALLY CURVED TRANSLATIONAL IONIZING
             SHOCK FRONT AND SUBSEQUENT TRANSVERSE WAVE SYSTEM. GAS ENTERS SHOCK
             FRONT FROM LEFT MASS FLOW REPRESENTED BY ARROWS IS DEFLECTED
             ACCORDING TO ANGLE OF INCIDENCE β; DIVERGING ARROWS RESULT IN
             EXPANSION REGIONS E; CONVERGING ARROWS GIVE RISE TO COMPRESSION
             REGIONS C, WHICH CONVERGE TO FORM TRANSVERSE SHOCKS S; SHOCKS NEAR
             THE WALL REFLECT, MAINTAINING PATTERN. IF SHOCKS ARE OF EQUAL
             STRENGTH NO CONTACT SURFACE RESULTS; OTHERWISE CONTRACT SURFACES
             WILL FORM.

       (b)   FLOW ENTERING AN OBLIQUE SHOCK IS DEFLECTED TOWARD THE SHOCK:
             NORMAL VELOCITY ACROSS SHOCK WAVE IS REDUCED; PARALLEL COMPONENT
             REMAINS UNCHANGED.
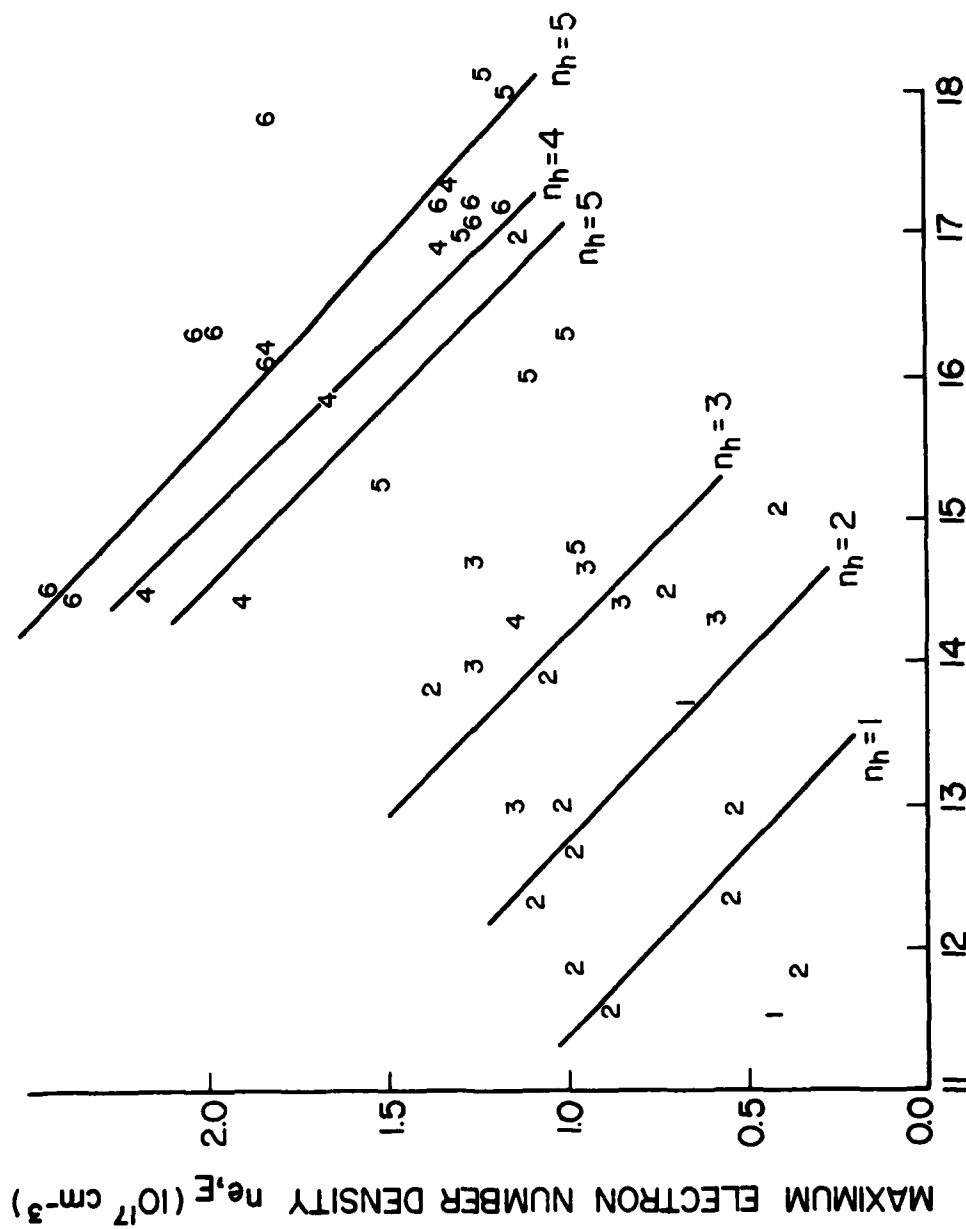
FIG. 30. VARIATION OF OBSERVED NUMBER OF HALF WAVES n_h, BEHIND NONPLANAR TRANSLATIONAL FRONT OF AN IONIZING SHOCK WAVE IN ARGON, WITH MAXIMUM ELECTRON NUMBER DENSITY $n_{e,E}$, AND MACH NUMBER M_s. EACH SYMBOL REPRESENTS ONE EXPERIMENTAL RUN. THE LOCATION OF A SYMBOL ON THIS PLANE WAS CHOSEN, BUT THE VALUE OF n_h WAS OBSERVED. THE UPPER-LEFT AND LOWER-RIGHT CORNERS ARE EMPTY DUE TO THE LIMITATIONS IMPOSED BY THE CRITICAL CONDITIONS ON THE SHOCK-TUBE FACILITY.

UTIAS Technical Note No. 222

Institute for Aerospace Studies, University of Toronto (UTIAS)
4925 Dufferin Street, Downsview, Ontario, Canada, M3H 5T6

AN EXPERIMENTAL STUDY OF NONSTATIONARY INSTABILITIES OF PLANAR SHOCK WAVES
IN IONIZING ARGON

Buchanan, W. L.   Approx. 50 pages   30 figures

1. Shock-wave stability   2. Ionizing shock-wave structure   3. Shock-tube flows

I. Buchanan, W. L.   II. UTIAS Technical Note No. 222

A multipulse laser-schlieren technique was used to study the time behaviour of instabilities
in the translational front of planar shock waves in ionizing argon in the 10 x 18 cm hyper-
velocity shock tube at UTIAS. Using a ruby laser in a combined normal-lasing/giant-pulse
mode, at least two monochromatic light pulses were obtained about 7 µs apart. As well, a
schlieren system compatible with the 23 cm dia Mach-Zehnder interferometer was created with
maximum sensitivity for some low-density conditions. The almost-sinusoidal perturbations
were found to change with time; some like a standing wave, and others like a travelling
wave. It was not, however, possible to associate the observed perturbations with either
form of wave motion in nearly half of the cases. A simple graph provides a way to predict
the shape of the perturbations from the shock-wave parameters.